University of Alberta

THE UNIVERSITY OF ALBERTA

NUCLEAR REACTION STUDIES

OF

BORON-12 AND OXYGEN-17

by

THOMAS KENNEDY ALEXANDER

A THESIS

SUBMITTED TO THE FACULTY OF GRADUATE STUDIES

IN PARTIAL FULFILMENT OF THE REQUIREMENTS FOR THE DEGREE

OF DOCTOR OF PHILOSOPHY

DEPARTMENT OF PHYSICS

EDMONTON, ALBERTA

JANUARY, 1964

UNIVERSITY OF ALBERTA

FACULTY OF GRADUATE STUDIES

The undersigned certify that they have read,
and recommend to the Faculty of Graduate Studies for
acceptance, a thesis entitled NUCLEAR REACTION STUDIES
OF BORON-12 AND OXYGEN-17, submitted by Thomas Kennedy
Alexander in partial fulfilment of the requirements for
the degree of Doctor of Philosophy.

ABSTRACT

The first two excited states of B^{12} have been studied
using the $B^{11}(d,p)B^{12}$ reaction and particle-gamma-ray coincidence
techniques. The gamma-ray branching ratio of the 1.67-MeV state
to the 0.95-MeV state was found to be $(6 \pm 3)\%$ of the ground-state
transition. An upper limit on the lifetime of the 0.95-MeV state
was obtained by direct timing, $\tau < 3 \times 10^{-10}$ sec. The angular
correlation of the 0.95-MeV gamma ray measured in time coincidence
with protons observed at 90° is isotropic at a bombarding energy
of 1.5 MeV. The combined data are not sufficient to determine the
spin of the 0.95-MeV state. The proton-gamma-ray angular correla-
tion of the 1.67-MeV state is isotropic for the same experimental
conditions.

The 3.06- and 3.85-MeV levels of O^{17} have been investigated
using the $C^{14}(\alpha,n)O^{17}$ reaction and neutron-gamma-ray coincidence
techniques. Doppler-shift measurements of the 3.85- and 2.19-MeV
gamma rays yielded $\tau \leq 0.25 \times 10^{-13}$ sec. and $\tau = 1.2^{+0.9}_{-0.6} \times 10^{-13}$
sec. for the lifetimes of the 3.85- and 3.06-MeV states respectively.
The measurements of the neutron-gamma-ray angular correlations,
combined with the lifetime estimates, give the spin assignment
$5/2^-$ for the 3.85-MeV state and confirm the $1/2^-$ spin assignment
for the 3.06-MeV state.

A fast timing system has been developed for use with
solid-state particle detectors. The observation of the time relation
between the protons and gamma rays detected in a plastic scintillator

was used to demonstrate the performance for p-γ delayed coincidence measurements. For the $O^{16}(d,p)O^{17}$ reaction to the first excited state, the timing resolution obtained was approximately 1.3 nanoseconds. This indicates that lifetimes greater than ~0.5 nanoseconds can be measured directly from the slope of the delayed edge of the resolution curve.

ACKNOWLEDGEMENTS

In looking back over the period of this thesis, I find I am indebted to many people.

The supervision of Dr. G. C. Neilson was particularly instructive and for this, special thanks are due. The discussions with, suggestions and assistance from Dr. J. T. Sample and Dr. W. K. Dawson are gratefully acknowledged. Special thanks are due to Dr. D. W. Braben for his participation in the boron-12 experiment.

The oxygen-17 experiment was done at the Chalk River Laboratories in collaboration with Doctors A. E. Litherland and C. Broude. Dr. Litherland suggested the experiment.

I wish to express my appreciation to W. C. Olsen who prepared the boron targets and to W. G. Davies who performed some computer calculations on some of the data.

The assistance of J. B. Elliott and his technical staff, E. B. Cairns, L. Holm and C. Green, is gratefully acknowledged.

Financial assistance was provided by the National Research Council and the University of Alberta in the form of scholarship awards.

The assistance of my wife, Loretta, in the preparation of the manuscript is only a minor part of her real contribution.

CONTENTS

Page

Contents   Page

LIST OF TABLES

LIST OF FIGURES

List of Figures

---

*NOTE: Figures 4.1 to 4.8 are denoted by Figures 1 to 8
       in Section 4.3.

CHAPTER 1

INTRODUCTION

The experiments described in this thesis are investiga-
tions of the low-lying states of B^{12} and O^{17}. The emphasis is
placed on the experimental techniques used to study these nuclei.
The importance of nuclear spectroscopy is concisely described
in the following quotation:

"The study of nuclear reactions of the light nuclei
is not at present one of the basic investigations of
nuclear physics. At present, emphasis is place increas-
ingly on attempts to interpret the inter-nucleon force
in terms of quantized field theory in which the π-mesons
are the quanta. The behaviour of the meson-nucleon
system and the role played by new unstable particles in
field theory have therefore become the central questions
of nuclear physics. At first sight it might appear that
the interactions of relatively complex systems of
nucleons, moving with non-relativistic velocities, could
contribute little to an answer to these questions. This
is however not so, at least in so far as the force be-
tween nucleons is concerned. Although important proper-
ties of this force can be inferred from the two-body
system and from the knowledge that nuclear forces show
saturation, some properties, such as charge indepen-
dence, do seem to be best exhibited in the existence of
nuclear charge multiplets. The existence of non-central
couplings is perhaps basically a matter for high energy
experiments, but such properties are also revealed in
nuclear level splittings and in the sequence of single

particle states of the nuclear shell model, and the
possibility of many-body forces can only be investigated
through a detailed knowledge of many-body systems.
These reasons, apart from the general interest of the
subject as a field for experimental endeavour, justify
the effort still being expended in investigating the
behaviour of light nuclei, and in tabulating their
excited states."

This quotation is from W. E. Burcham's article on the
spectra of light nuclei (Bu57). As he points out, the study of the
properties of nuclear energy levels seems at first to be far removed
from the study of nuclear forces. Rarely can any far reaching con-
clusions be drawn from a single experiment, which may be difficult
in itself. Thus the experimenter is concerned with nuclear spectro-
scopy, since it is very difficult to design an experiment that results
in a direct measurement of some aspect of nuclear forces as they
exist in nuclear matter.

The study of nuclei has produced a bewildering number of
models of varying complexity, which have as their basis some assump-
tions regarding the nuclear force. Each model emphasizes some aspect
of nuclear structure, and together, the models give quite a comprehen-
sive interpretation of the experimental data. To illustrate this and
to briefly review the present knowledge of O^{17}, consider the following
well-known problem in nuclear structure.

The O^{17} nucleus consists of eight protons and nine neutrons,
or sixteen nucleons and one neutron if we interpret by means of the
shell model, since the 1p shell is doubly filled at O^{16}. The neutron,
then, is in the (1d,2s) shell and gives the O^{17} nucleus properties of

a single-particle nature. Experimental studies of the excited states of O^{17} are required to identify the single-particle states of the shell model as they occur in the (1d,2s) shell. The 2s1/2 state experimentally appears as the first excited state at 0.871 MeV. Experiment has shown that the ground-state spin is 5/2$^+$ and the spin of the first excited state is 1/2$^+$. Thus the odd neutron must have a relatively independent motion described by it being in the field of the others comprising the core. But an interesting thing was observed; the lifetime of the 1/2$^+$ state was measured to be 2.6 x 10^{-10} sec. The shell model forbids this transition, since it assumes a single neutron outside a closed shell and an E2 transition should be inhibited. In addition, the non-zero value of the ground-state quadrupole moment (-0.005 bns) does not agree with the single-particle description even though the ground-state magnetic dipole moment does (-1.894 nm). In other words the independent, single-particle motion assumption is too simple and has to be modified by introducing collective motion, i.e. the O^{16} core must be distorted. Several theoretical calculations have been done and successfully account for the observed radiative lifetime of the 0.871-MeV state, e.g. see reference (Ra60). As will be described later in connection with the work done in this thesis, the experimental evidence indicates that the next two excited states of O^{17} are not simple states.

The impression so far is that only by careful consideration of all the data can anything resembling a correct interpretation be obtained. On the other hand, as indicated in the quotation from Burcham's article, some aspects of nuclear structure reveal themselves

clearly. One of the basic assumptions of nuclear structure, the charge independence of nuclear forces, has been observed clearly in mirror nuclei. (See Fig. 3.8 for the mass 17 mirror nuclei).

This aspect of nuclear structure is also exhibited in the existence of higher isobaric multiplets, but the experimental data are less extensive. Another chapter of this thesis describes some experimental work done to gain more information on B^{12}, which should have excited states corresponding to the $T = 1$ states in C^{12}, since these nuclei are members of a charge triplet.

To obtain B^{12} from C^{12}, which closes the p 3/2 subshell, a proton must be replaced by a neutron and the result is drastic (see Fig. 1.1) because the neutron cannot be put into the same sub-shell from which the proton was removed, due to the Pauli Principle. Nevertheless, the ground state of B^{12} and the 15.11-MeV level of C^{12} both have $J^{\pi} = 1^{+}$ and are members of an isobaric triplet. The anologue of the B^{12} ground state can be predicted to be at 15.21 MeV in C^{12} with reference to the ground state of C^{12}, using the ground-state mass differences together with a Coulomb correction (Wi56). The large energy shift has been reproduced by the theoretical calculations of Kurath (Ku56). The spins of the first two excited states of B^{12} had not been assigned experimentally so that the experimental investigation of these states seemed worthwhile.

If the excited states of B^{12} are populated using the $B^{11}(d,p)B^{12}$ reaction, then the radiative properties of these states
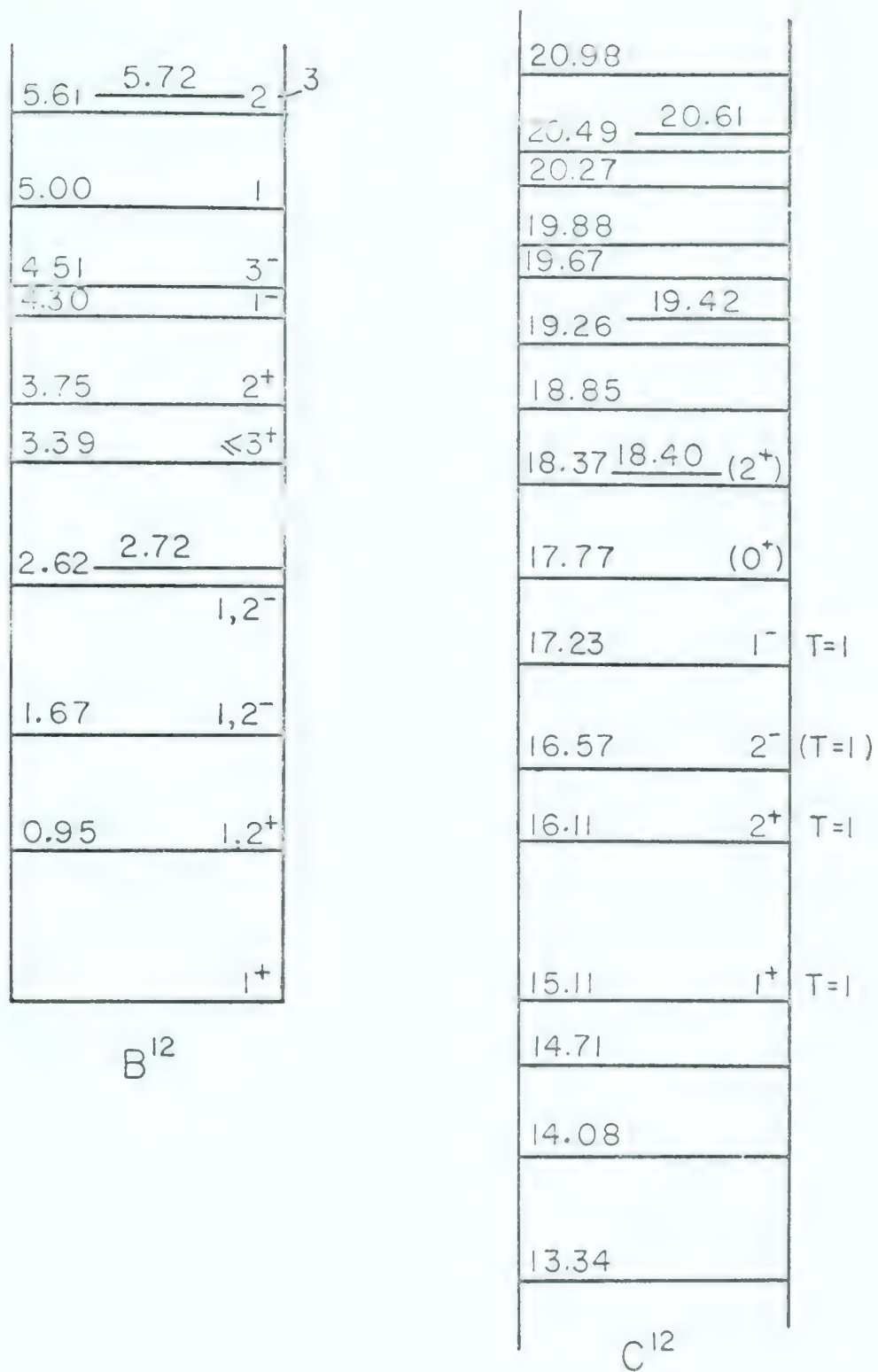
FIGURE 1.1

The Energy Level Diagrams of B^{12} and C^{12}

The ground state of B^{12} is located at the 15.11 MeV
level of C^{12} to indicate the isobaric correspondence of
these nuclei.

can be investigated using proton-gamma-ray coincidence measurements. Chapter 2 describes the measurements carried out using the $B^{11}(d,p)B^{12}$ reaction to study the first two excited states. These measurements yielded the gamma-ray branching ratio of the 1.67-MeV state, some proton-gamma-ray angular correlations and a rather crude limit, as it turned out, on the lifetime of the 0.95-MeV state. Definite spin assignments for the states of B^{12} cannot be made on the basis of these measurements alone. Also, the lifetime of the 0.871-MeV state of O^{17} was remeasured by delayed coincidence measurements.

To do the above measurements, a fast timing system for use with a solid-state particle detector was developed. This work is described in detail in Chapter 4. Some other interesting aspects of this system, e.g. the detection of a pulsed accelerator beam, were demonstrated and are described in Chapter 4.

Some experimental work done with the $C^{14}(\alpha,n\gamma)O^{17}$ reaction and n-γ coincidence techniques is described in Chapter 3. These measurements were carried out to determine the spins of the 3.06- and 3.85-MeV levels of O^{17}. Neutron-gamma-ray angular correlation measurements, combined with measurements of the life-times of the states, resulted in unambiguous spin assignments. Some of the electronic apparatus used for the O^{17} work was developed by the author previous to the period of this thesis. The apparatus included a multiparameter pulse-amplitude analyser developed by Robinson, McNaught and the author (A162, A162a). A pulse-shape analyser to distinguish neutrons from gamma rays detected in an organic scintillator was also used for the O^{17} work (A161).

Neither of these instruments is described in this thesis.

The direct-timing and Doppler-shift methods of measuring nuclear lifetimes have been used in the work described in Chapters 2 and 3. Since the measurement of nuclear lifetimes is a powerful tool of experimental nuclear physics, these methods are presented in Chapter 5. The methods are described with reference to the experiments done on B^{12} and O^{17} to complement the rather brief descriptions of the techniques given in Chapters 2 and 3. In some other experimental methods used during the investigations are described in Chapter 5. There is not much of an original nature in Chapter 5 except perhaps the demonstration of a fast particle-gamma-ray coincidence technique suitable for delayed-coincidence measurements in the nanosecond region.

The Nuclear Research Center is well equipped for fast timing experiments with scintillation detectors through the work of Neilson et al (Ne59). Advantage was taken of the existing apparatus for the scintillation detector and its associated electronics.

THE 0.95- AND 1.67-MeV STATES OF BORON-12

2.1 Introductory Remarks

The close similarity of the excited states of mirror nuclei has been established for some time. Also, for states with $T = 1$, the correspondence of the ground state of the $T_Z = 1$ nucleus to the $T_Z = 0$ nucleus is well known. The isobaric correspondence for the excited states of the $T_Z = 1$ member with the $T_Z = 0$ nucleus has been verified experimentally, notably for the triplets C^{14}-N^{14}-O^{14} and N^{16}-O^{16}-F^{16} (Ta60). (It is not surprising that there are no cases where the correspondence, i.e. J and π as well as excitation energy, between the $T_Z = \pm 1$ members of a triplet has been seen experimentally, since the states are not easily excited.) The members B^{12} and C^{12} of the mass-12 triplet also present a suitable case to study since the excited states of C^{12} have been studied extensively. The states of interest in the comparison are at approximately 15 MeV in C^{12}, but they are well separated.

The states in the $T_Z = \pm 1$ members of an isotopic spin triplet are not easily accessible to experimental investigation because of the scarcity of simple reactions to populate the states. In the present investigation, the $B^{11}(d,p)B^{12}$ reaction is used to excite B^{12}, and measurements are made with two high efficiency spectrometers, the solid-state detector and the NaI(Tl) scintillation counter. The measurement of the gamma-ray transitions in

coincidence with the protons from the $L^{11}(d,p)B^{12}$ reaction is used for the study of the excited states of B^{12}.

The maximum energy of the University of Alberta 2 MV Van de Graaff accelerator allowed the first two excited states to be populated and studied. Figure 2.1 shows the low lying levels of B^{12} and the reaction transitions studied.

The spin-parity assignments for the 0.95-MeV and 1.67-MeV states are $\leq 3^{+}$ and 1^{-} or 2^{-} respectively. The limits on the assignments have come from a stripping theory analysis of the $B^{11}(d,p)B^{12}$ angular distribution measurements of Holt and Marsham (Ho53). For the 0.95-MeV state, previous measurements of the proton-gamma-ray angular correlation tend to favour $J^{\pi} = 1^{-}$ or 2^{+} with a mixture of M1 and E2 radiations or 3^{+} with pure E2 radiation (Co61). The angular distribution of 0.95-MeV gamma-rays is anisotropic (Ko60, Co62, Wa63) ruling out $J^{\pi} = 0^{+}$ for the 0.95-MeV level.

The ground-state spin and parity ($J^{\pi} = 1^{+}$) have been established from the beta decay to C^{12} (Ka58), and the ground state of B^{12} is in isobaric correspondence with the 15.11-MeV state of C^{12}.

To gain more information on the first two excited states, the proton-gamma-ray angular correlations of the 0.95- and 1.67-MeV states have been observed at a bombarding energy of 1.5 MeV. The results of these measurements are consistent with the known properties of the states, but cannot give a unique spin assignment to either state.
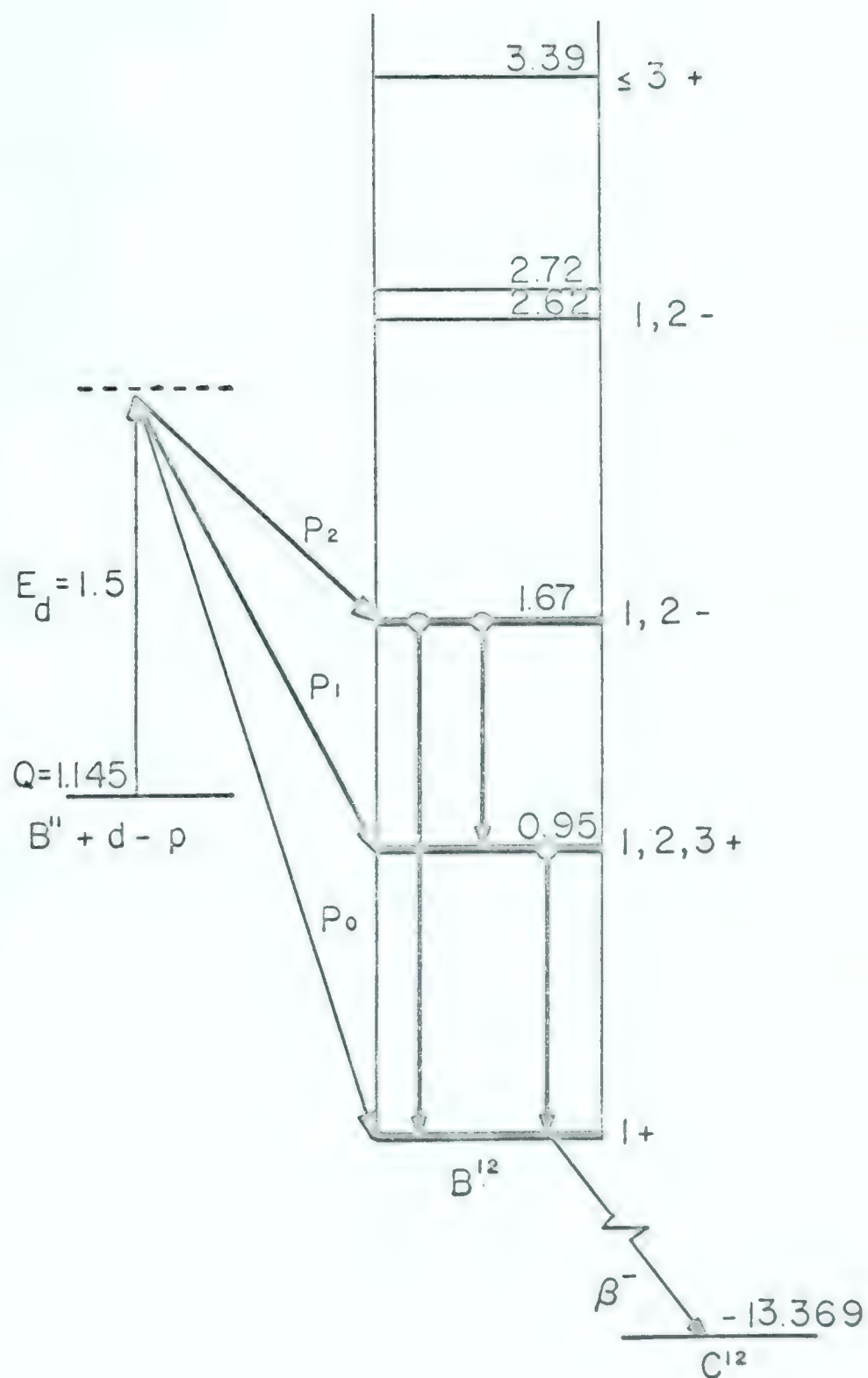
FIGURE 2.1

The Energy-Level Diagram of B^{12}

The levels studied in this investigation are indicated by heavy lines. The $B^{11}(d,p)B^{12}$ reaction and p-γ coincidence measurements are used.

The gamma-ray branching ratio of the 1.67-MeV state has been measured. A weak stop-over transition was observed to compete with the direct ground-state transition.

Finally, an upper limit on the radiative lifetime of the 0.95-MeV state was obtained by direct observation of the time relation of the protons and gamma-rays from the $B^{11}(d,p\gamma)B^{12}$ reaction.

2.2 Experimental Apparatus and Procedure

The targets consisted of thin self-supporting films of approximately 20 μgm/cm^2 natural boron, which is about 80% B^{11}, so reactions due to B^{10} were also observed. These targets were prepared by W.C. Olsen (O164) of this laboratory by electron bombardment techniques.

The $O^{16}(d,p)O^{17}$ reaction was used as a comparison for lifetime estimates. Thin self-supporting targets of quartz (SiO$_2$) were prepared by blowing a bubble of quartz until it exploded. These targets were approximately 200 μgm/cm$^-$ thick and could also be used for beam alignment due to their fluorescence under bombardment.

The gamma rays were detected in a 2 in. diam. by 2 in. long NaI(Tl) crystal which was unshielded except for a 1/4 in. slab of lead placed in front of the crystal to stop the high energy electrons from the beta decay of B^{12}. The NaI crystal was replaced by a 2 in. by 2 in. plastic scintillator for the fast coincidence measurements. For most of the measurements, the front face of the detector was 10 cm from the target.

The charged particles from the reactions were detected in a Nuclear Diodes 300-ohm-cm surface barrier silicon detector collimated so that no particles entered the active area near the edges. A 10 μin. nickel foil in front of the detector prevented heavy ions from entering it, since a large coincidence rate was observed from $B^{11}(d,n)C^{12}$ without the foil in place. The electronics for the solid-state detector uses the technique of double-differentiation shaping and zero-cross-over detection to produce the timing signal from the same preamplifier used for linear amplification. This system is described in Chapter 4. The resolving time for the p-γ coincidences using the NaI detector was set to approximately 5 ns, although a resolution of 2 ns could be obtained for single transitions. With the plastic scintillator, the resolution was about 1.2 ns as will be discussed later.

Figure 2.2 shows an ungated charged-particle spectrum from the natural boron target at a deuteron bombarding energy of 1.5 MeV. The dotted line is the charged-particle spectrum from the B^{10} + d reaction taken under identical conditions, using a self-supporting target of B^{10}. This spectrum has been normalized so that the intensities of the B^{10} groups for the two targets are roughly equal. The 1.67-MeV group is clearly resolved, whereas the 0.95-MeV group is not entirely separated from the weaker 8.92-MeV group from the $B^{10}(d,p)B^{11}$ reaction. The separation is, however, better at a bombarding energy of 1.7 MeV. It is seen that the group at approximately 1 MeV is mainly due to deuteron elastic scattering from O^{16} contamination on the target; C^{12} contamination
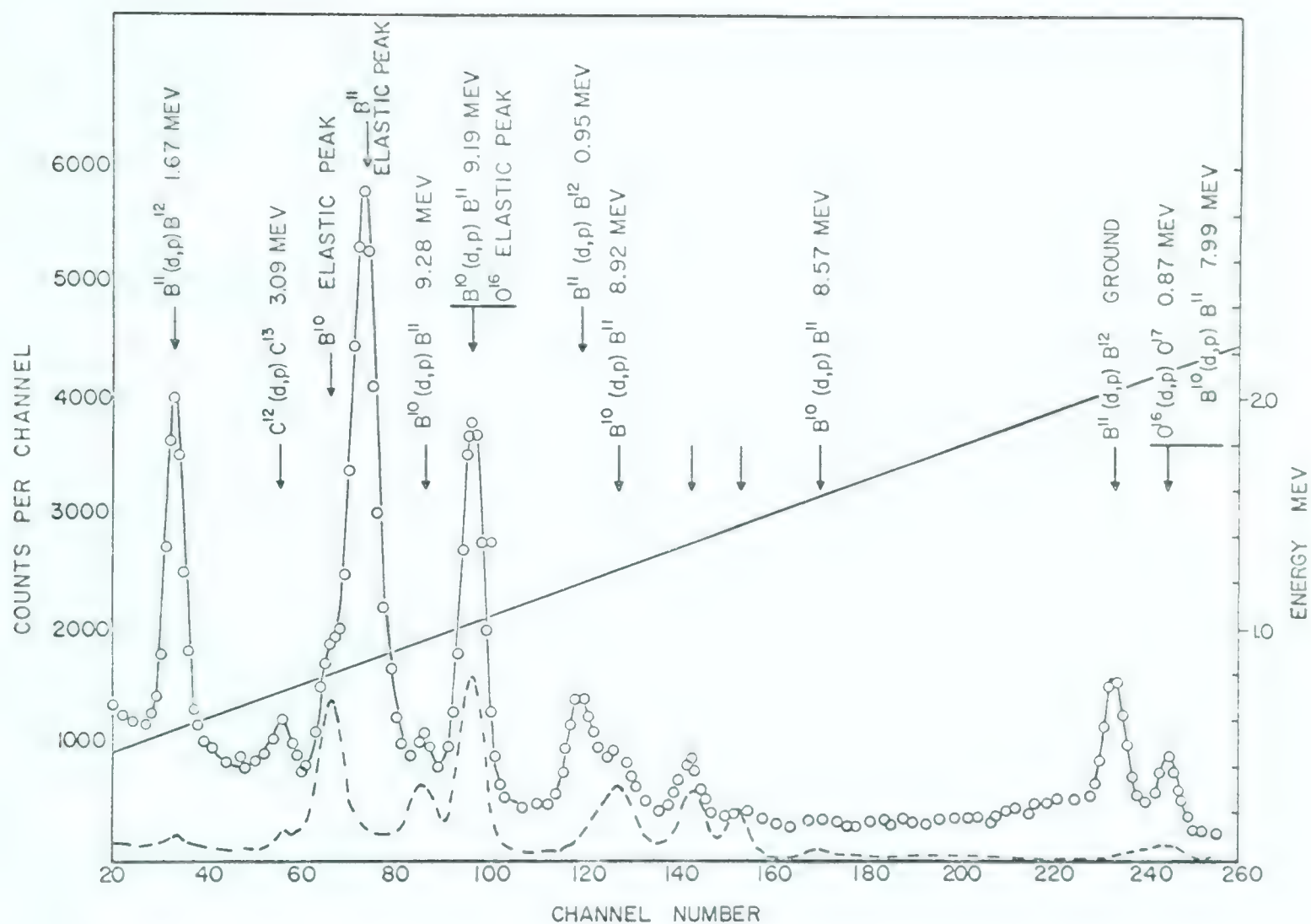
FIGURE 2.2

The Ungated Charged-Particle Spectrum from the Deuteron
Bombardment of Natural Boron at a Bombarding Energy
of 1.5 MeV

The particle detector subtends a half angle of 7.5° and
is located at 120°. The dotted curve is the spectrum from
B^{10} + d under identical conditions. The unidentified peak at
1.45 MeV may be elastic scattering from tantalum, which was
the material used for the evaporation boat during target
preparation.

was also present.

The gamma-ray background due to reactions arising in the Faraday cup was minimized by lining it with clean platinum, while the radiation from the beam defining slits was reduced by placing approximately 3 in. of lead in the form of a right cylinder with a co-axial hole inside the beam vacuum tube, just after the slits. However, annihilation radiation was still observed after a period of bombardment due to carbon build-up presumably on the Faraday cup and on the target. The build-up was observed on the target, since the proton groups to the ground state and the 3.09-MeV state from the $C^{12}(d,p)C^{13}$ reaction were observed to change during the course of the experiment. For this reason the ungated particle spectrum was constantly monitored by a 256-channel pulse amplitude analyser (see Fig. 2.3).

The general electronic block diagram for the measurements is shown in Fig. 2.3. The system was arranged so that any one of the particle spectrum, the gamma-ray spectrum, or the output of the time-to-amplitude converter could be analysed by a 1024-channel kicksorter operated in a four groups by 256-channel mode. The group selection was triggered by the outputs of two double-channel analysers designed by Goulding and McNaught (Go60) and built in this laboratory. In this way we approximated a two-parameter analyser that proved to be particularly useful in the branching-ratio measurements.

Each experimental run usually consisted of taking the following measurements:
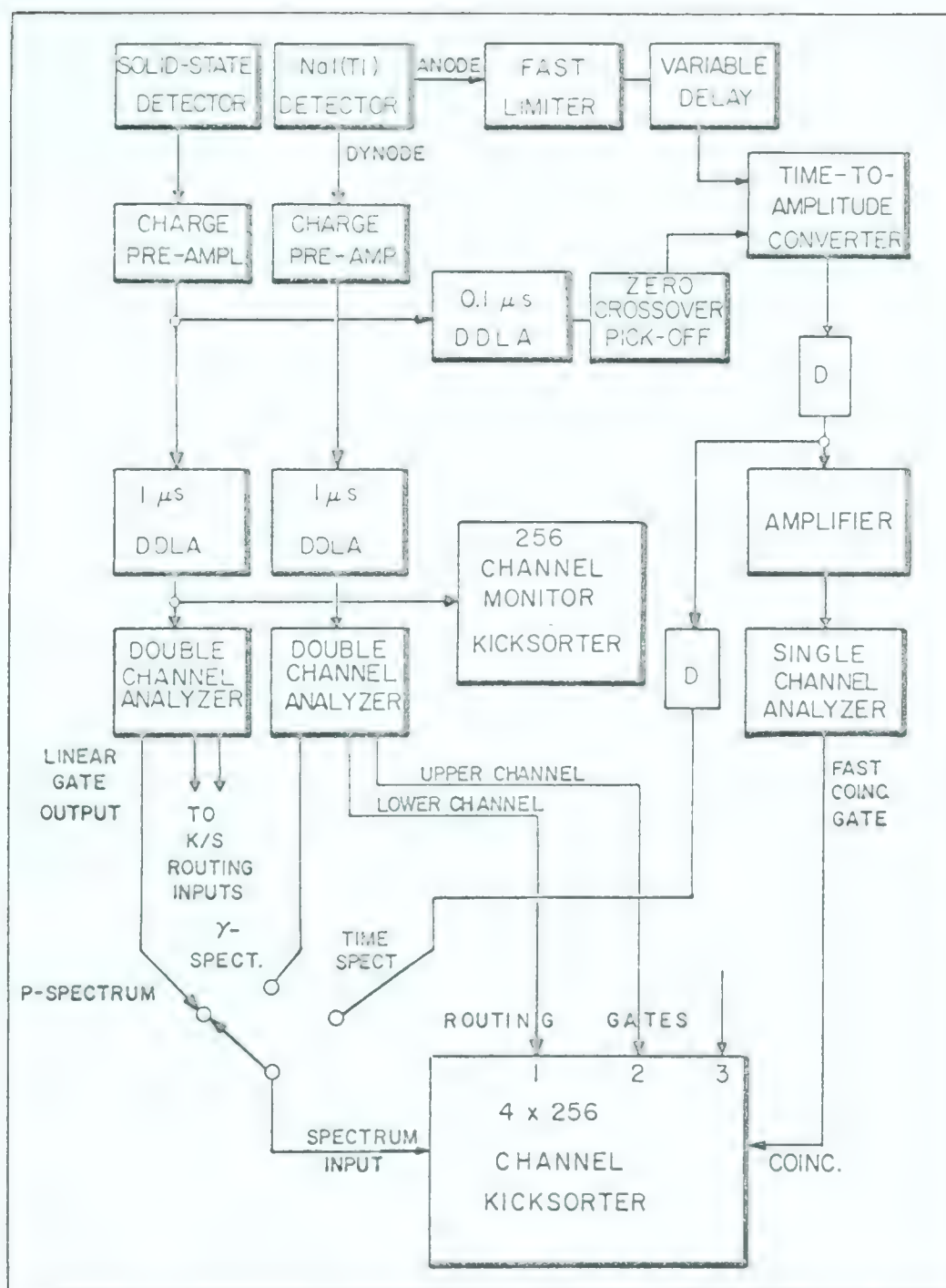
FIGURE 2.3

The Electronic Apparatus

1. The direct spectrum of both detectors was recorded previous to observing the coincidences.

2. The single-channel analysers were then set up, and the portion of the spectrum in the "window" recorded.

3. The coincidence spectrum was recorded for a given amount of charge collected on the Faraday cup and the target. A typical run would take about one hour at a beam current of 0.08 µA.

4. Simultaneously with recording the coincidence spectrum, the direct spectrum of the solid-state particle detector was recorded as mentioned before. This procedure also checked that the resolution of the particle detector was not deteriorating with irradiation or because of light leaks into the target chamber.

5. Procedures 1 and 2 were repeated at the end of the coincidence run, and the stability of the system checked. In general the electronic stability was satisfactory, but as mentioned before we did observe a small build-up of foreign material on the target.

2.3 Experimental Results

A. Coincidence Spectra and the Branching Ratio of the 1.67-MeV State

Figure 2.4 shows the gamma-ray spectrum in coincidence with the proton group to the 0.95-MeV state, taken at a bombarding energy of 1.5 MeV. The particle gate was shifted to the ground-state group from the $C^{12}(d,p)C^{13}$ reaction to obtain a measure of the random background, which is also plotted in Fig. 2.4.

FIGURE 2.4

The Gamma-Ray Spectrum in Coincidence with the Proton
Group Leading to the 0.95-MeV State

The random background is estimated by measuring coinci-
dences with the particle gate selecting the ground-state
group from $C^{12}(d,p)C^{13}$.

Previous to this measurement, the transition from the 1.67-MeV state to the 0.95-MeV state had not been observed. The primary evidence for the stop-over transition is shown in Fig. 2.5. This gamma-ray spectrum was obtained by recording coincidences with the proton group leaving B^{12} in its 1.67-MeV state. As can be seen from the figure, the 0.95- and 0.72-MeV full-energy peaks are present, and allow us to estimate the branching ratio. Analysis of the spectrum indicates that <10% of the transitions stop-over at the 0.95-MeV level.

To obtain a better determination of the relative intensities of the competing transitions, another experiment was carried out. A graphic description and the results of this measurement are shown in Fig. 2.6. On the right-hand side of the diagram is the direct gamma-ray spectrum, in which the prominent features are the 1.67- and the 0.95-MeV peaks. Two channels of a double-channel analyser were set to select two adjacent regions of the spectrum. The lower gate (0.66 ± 0.03 to 1.14 ± 0.01 MeV) included the full-energy peaks of both the 0.72- and the 0.95-MeV gamma rays. The upper gate (1.14 ± 0.01 to 1.48 ± 0.01 MeV) was set to include only the Compton region of the 1.67-MeV gamma ray, the width of the channels being adjusted so that the areas of the two regions would be approximately equal for a pure 1.67-MeV line shape as determined for our detector.

The pulse-amplitude distributions shown on the left-hand side of Fig. 2.6 are the spectra of coincident charged particles obtained. The spectra were recorded in a 1024-channel
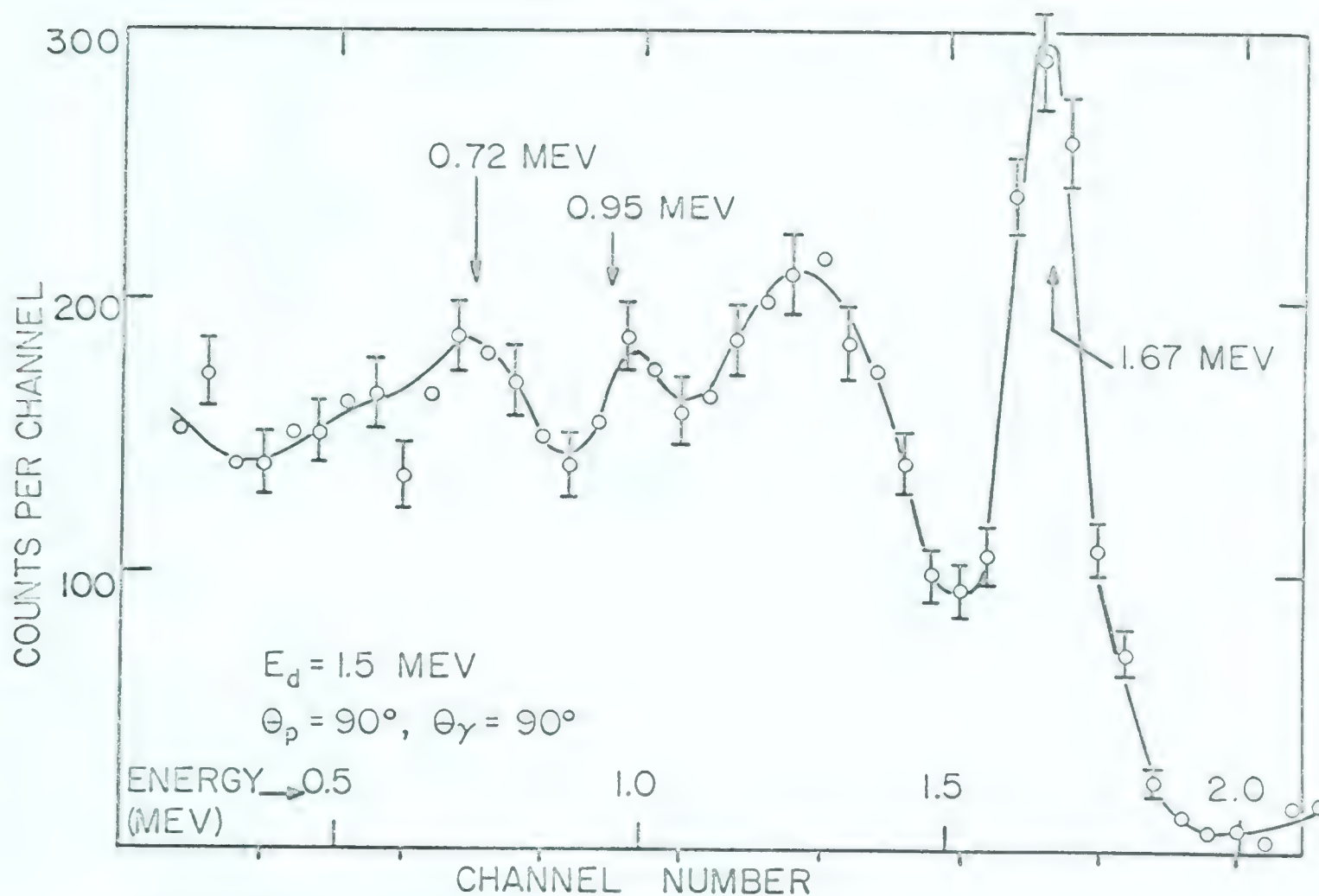
FIGURE 2.5

The Gamma-Ray Spectrum in Coincidence with the Proton
Group leaving B^{12} in the 1.67-MeV State

The intensity of the stop-over transition is less than
approximately 10% of the ground state transition. The
spectrum in the region of 1.3 MeV is too peaked to be accounted
for by the Compton edge of the 1.67-MeV gamma ray. The
origin of the bulge just above the 1.67-MeV full-energy peak
is also unknown.
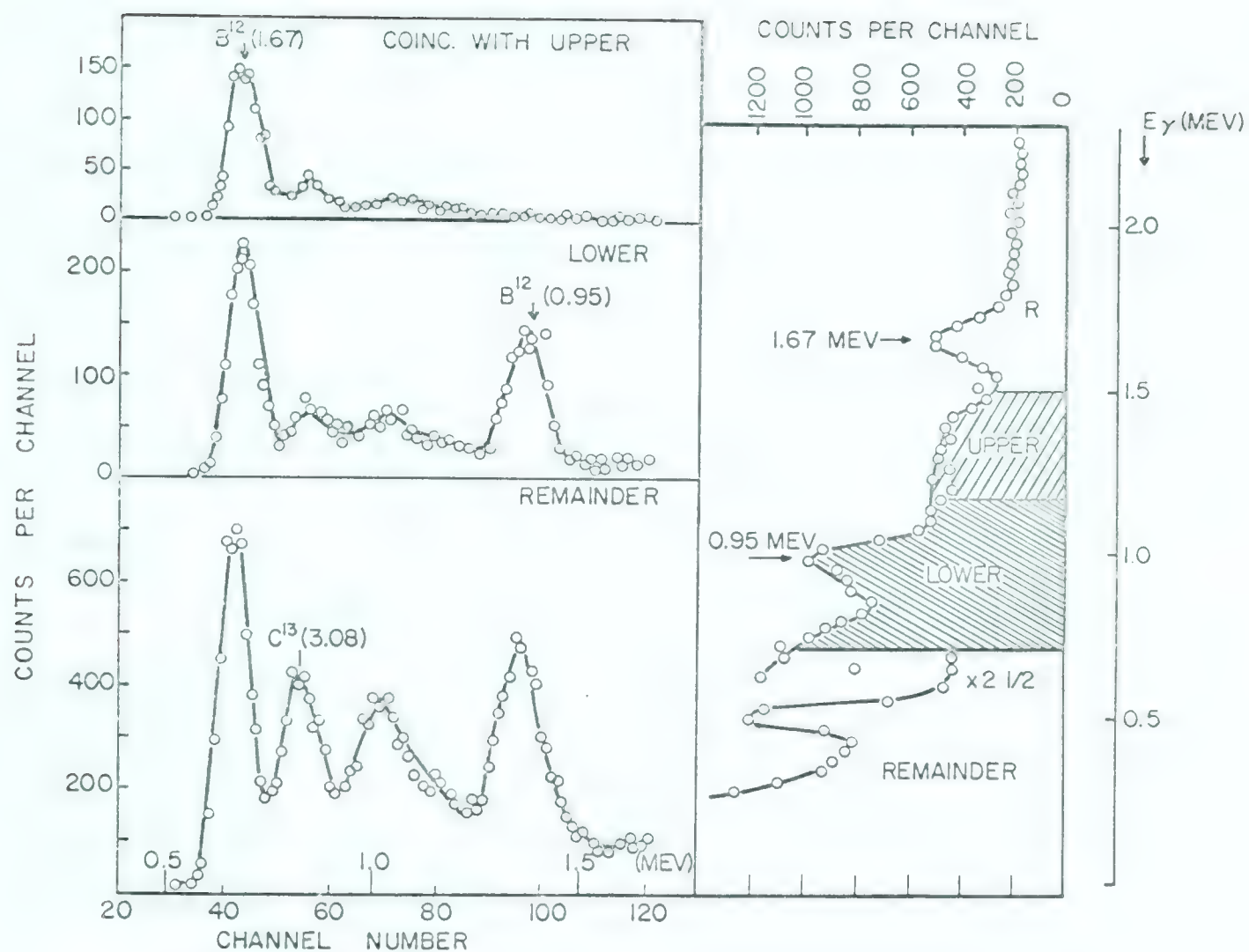
FIGURE 2.6

A Measurement of the Branching Ratio of the 1.67-MeV
State by Observing the Intensity of the Proton Groups
in Coincidence with Appropriate Regions of the Gamma-
Ray Spectrum

The spectrum on the right is the direct gamma-ray
spectrum. The coincident particle spectra on the left are
described in the text.

pulse-amplitude analyser operated in a four by 256 channel mode,
the pulses from the double-channel analyser selecting the
appropriate group of 256 channels as shown in Fig. 2.3.

The spectrum at the bottom represents all coincidences
not conditioned by either the upper or lower selections on the
gamma-ray energy. This additional information has been used as
a consistency check on the more useful data contained in the
two other groups of channels. The number of events recorded in
this "remainder" spectrum must be in the correct proportion as
known from the line shapes for the scintillation counter.

The peaks labelled "B^{12}(1.67)" contain the measurement
of the branching ratio. If the stop-over transition was zero
intensity, then the two peaks would be equal in intensity since
the rate in each gamma-ray gate was ideally equal for a pure
1.67-MeV line. Thus the ratio of the intensities of the two
proton groups gives a measure of the branching ratio.

The value obtained from these data is that the branch
to the 0.95-MeV state is (6 ± 3)% of the ground-state transition.
This result represents the sum of five runs, each taken at a
different angle of the gamma-ray detector, so that the branching-
ratio determination is an average over any possible angular
distribution. The value is in agreement with the shape of the
gamma-ray spectrum of Fig. 2.5.

B. Lifetime Estimate of the 0.95-MeV State

The spin of the first-excited state had not been determined,

but was known to be either 1^+, 2^+, or 3^+. If the gamma-ray trans-
ition had a lifetime long enough to be measured by direct timing,
then the radiation would be E2 and the spin assignment 3^+ would
be favoured. During the course of this measurement, Chase and
Warburton (Wa63) showed that, in fact, the lifetime was character-
istic of a M1 transition ($\tau_m = 3.4 \pm 1 \times 10^{-13}$ sec). Our
result, which gives an upper limit of 3×10^{-10} sec, corroborates
their determination by the Doppler-shift method.

The performance in time resolution using a solid-state
detector and a plastic scintillator was measured by observing
coincidences from the $O^{16}(d,p)O^{17}$ reaction to the first excited
state at 0.871 MeV. A recent precision measurement (Lo63) of the
lifetime of the O^{17} level is $\tau_m = (0.263 \pm 0.008)$ ns, making it a
suitable comparison for the transition in B^{12}. It was found
necessary to mount a 10 μin. Ni foil in front of the solid-state
detector to prevent the observation of delayed neutron coincidences
which presumably arise from high Q-value reactions. The effect
was observed even for the clean conditions of the $O^{16}(d,p)O^{17}$
reaction and was more pronounced when the gamma-ray detector was
at forward angles. This may explain the apparent, long lifetime
(0.43 ± 0.02 ns) measured by Gale et al. (Ga63) for the O^{17} level.
We did not attempt a precision measurement of the O^{17} lifetime
since the apparent discrepancy had been resolved. However, our
results agree with the value 0.26 ns.

Fig. 2.7A is the time spectrum obtained from the
$B^{11}(d,p\gamma)B^{12}$ reaction, with the proton gate selecting the 0.95-MeV

FIGURE 2.7

A. The Time Spectrum of the Gamma Rays from the $B^{11}(d,p)B^{12}$
    Reaction using the Proton Group to the 0.95-MeV State
                        for t = 0

    Neutrons from $B^{11}(d,n)C^{12}$, followed by alpha-particle
emission from C^{12} are also observed.

B. An Expanded Plot of the Gamma-Ray Peak

    The curve is a normal distribution derived from data
from the $O^{16}(d,p)O^{17}$ reaction to the 0.871-MeV State.

state. In addition to the gamma-ray peak, the spectrum shows two neutron groups arising from $B^{11}(d,n)C^{12}$, the C^{12} disintegrating by alpha-particle emission to produce a coincident charged particle. It is difficult to eliminate the neutron coincidences in this case, since the alpha-particle spectrum is a continuum under the proton group to the first excited state (see Fig. 2.2). Therefore, the front face of the plastic scintillator was moved to a distance sufficiently far from the target to resolve the neutrons.

Fig. 2.7B shows an expanded plot of the gamma-ray peak. The curve through the points is a normal distribution derived from the parameters obtained from the O^{17} results. To obtain the change in the time resolution due to the different proton energies (2.1 MeV in the case of O^{17} to 1.35 MeV for B^{12}), the variance of time due to the particle detector is assumed to vary as E_p^{-2}, a result verified by other tests on the system and discussed in Chapter 4. Thus the gamma-ray peak is "prompt" for our instrument, an upper limit on the lifetime being 0.3 ns.

C. Proton-Gamma-Ray Angular Correlations

The p-γ angular correlation of the 0.95-MeV state was measured at a bombarding energy of 1.5 MeV. To obtain a measurement with good selectivity, the gamma-ray spectrum was gated by energy selection on the proton group with the particle detector at $90°$. A measurement at more forward angles was considered unreliable because of interference due to proton groups from the

$B^{10}(d,p)B^{11}$ reaction together with the increased intensity of Coulomb scattering. The correlation angle, θ_γ, was in the plane defined by the beam and the particle detector.

The pulse-amplitude distribution shown previously in Fig. 2.4 is a typical coincidence spectrum of the 0.95-MeV gamma-ray observed during the correlation measurement. The background for these runs was obtained by setting the particle gate on the ground-state group of protons from the $C^{12}(d,p)C^{13}$ reaction, leaving all other conditions the same. As can be seen from the diagram, the "background" due to random coincidences is small compared to the signal from the $B^{11}(d,p)B^{12}$ reaction. The actual background was obtained from these "background" runs by using them to determine a shape factor for use with the actual counts occurring above the 0.95-MeV peak in energy (channels 55 to 70). Only the integrated counts in the full-energy peak of the 0.95-MeV gamma-ray were used as a measure of the relative intensity. The results of the correlation measurement are shown in Fig. 2.8. The data points have been corrected for the background as described above, but corrections for the finite solid angles of the detectors and for the anisotropy of the measuring apparatus have not been included. The anisotropy data were obtained by measuring the relative intensity of the 1.33-MeV gamma ray from a point source of Co^{60} placed at the target position, and is a trivial correction for $\theta_\gamma \geqslant 15°$. At $0°$, absorption in the Faraday cup reduced the intensity by 30%.
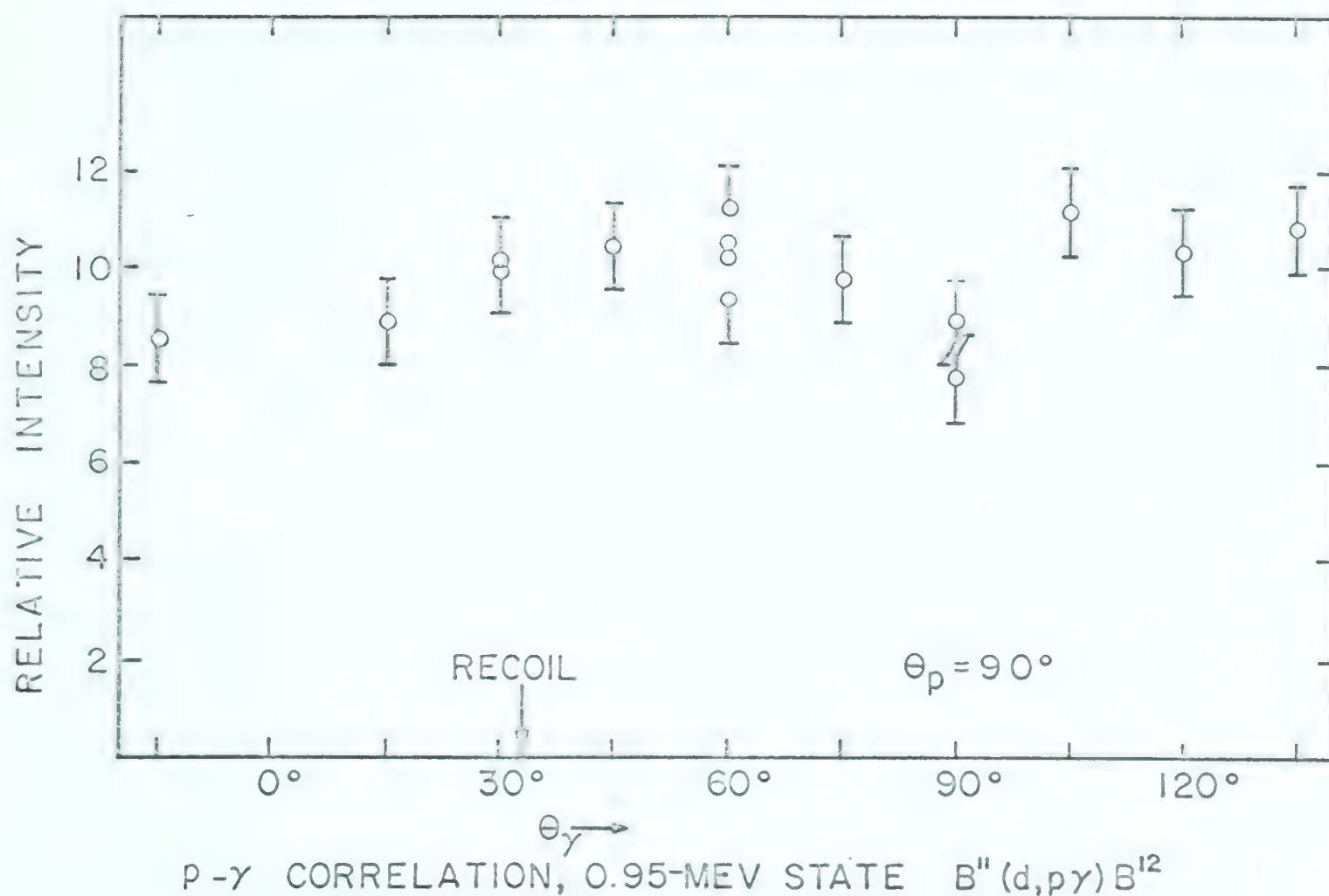
FIGURE 2.8

The p- γ Angular Correlation of the 0.95-MeV State

The errors include only statistical errors due to the finite number of counts in the full-energy peak and the background under it (e.g. see Fig. 2.4). Conditions of measurement are:

E_d= 1.5 MeV, θ_p= 90°, $\frac{1}{2}\triangle\theta_p$= 12.5°, distance from the target to the front face of NaI crystal = 10 cm, target thickness = 20 μgm/cm^2, and beam spot size = 2 mm x 2 mm. The relative intensity = (rate of coincident γ-rays) ÷ (the rate of ungated protons from $B^{11}(d,p_o)B^{12}$). The nuclear recoil axis is θ = 33.6°.

As can be seen, the correlation does not yield any measurable parameters since it is isotropic within the experimental errors. A discussion of the implications of an isotropic correlation is left to the last section. The result at $\theta_p = 90^o$ suggested that the interpretation of p-γ correlations would be uncertain, making this method of investigation unsuitable for our purposes.

Since the stripped-in neutron to the 1.67-MeV state has $\ell_n = 0$, a p-γ angular correlations measurement of this state would not be fruitful since it should be isotropic. However, p-γ correlation data were obtained as a by-product from the measurements of the branching ratio of the 1.67-MeV state. The intensity of the coincident protons was observed as the angle of the gamma-ray detector was rotated in the reaction plane (see Fig. 2.6) Since the energy selection on the gamma-ray spectrum was not restricted to the full-energy peak of the 1.67-MeV gamma-ray, scattering effects with an unknown angular dependence may be present. However, the results of this measurement, shown in Fig. 2.9, indicate that the correlation is isotropic as anticipated.

2.4 Summary of Results

The gamma-ray branching ratio of $(6 \pm 3)\%$ is consistent with the single-particle estimates ($\sim 8\%$) for competing El transitions. A recent experiment by Carlson and Norbeck (Ca63) using the $Li^7(Li^7, d)B^{12}$ reaction and multiparameter analysis techniques gave a smaller branching ratio limit of $< 2\%$.

FIGURE 2.9

The p-γ Angular Correlation of the 1.67-MeV State

See the caption of Fig. 2.8 for other details. The relative intensity was measured by observing coincident protons to the 1.67-MeV state.

The limit on the lifetime estimate of the 0.95-MeV state yields $|M(E2)|^2 > 2.3$ or $|M(M1)|^2 > 10^{-4}$ Weisskopf units, and does not allow a conclusion as to the type of radiation, since E2 transitions are typically enhanced by a factor of five in light nuclei (W157). However, the measurement of Warburton and Chase yields $|M(M1)|^2 = 1 \times 10^{-1}$ W.U., a typical value for M1 transitions in 1p-shell nuclei (W160).

The p-γ angular correlations for the 0.95- and 1.67-MeV states are isotropic within the accuracy of the experiments. The correlations are measured at 1.5 MeV bombarding energy and the protons were detected at 90°.

2.5 Discussion

In this discussion an attempt will be made to review the experimental data concerning the excited states of B^{12}.

The evidence available on the angular correlation and the angular distribution of the 0.95-MeV gamma-ray is no less than confusing. The immediate concern is to decide whether the angular correlation reported here is consistent with the published data. Table 2.1 summarizes the angular correlation results from measurements using the $B^{11}(d,p)B^{12}$ reaction.

β-γ Correlation	Ang. Distribution	E_β (Mev)	θ_2	Reference
$1+(0.35 \pm 0.07)P_2$		5.5	20°	Go61
	Anisotropic [1]	0.8	–	Ko60
	Anisotropic [2]	2.0	–	Go62
	$1-(0.035 \pm 0.01)P_2$ [3]	0.8	–	Wa63
Isotropic		1.5	90°	Present Work

Notes: (1) The distribution is not symmetric about 90°, and the anisotropy is large but numerical results are not given.

(2) No numerical results given.

(3) This result is in marked disagreement with (Ko60) although measured under identical conditions.

TABLE 2.1

All the investigations concerned with the angular distribution of the 0.95-MeV gamma ray agree that it is anisotropic, but the only numerical data show that the anisotropy is small. An angular

distribution measurement was attempted in the present investigation, but analysis of the data was considered unreliable because of oxygen contamination on the target. The $O^{16}(d,p\gamma)O^{17}$ reaction is prolific in producing 0.87-MeV gamma radiation which was unresolved from the 0.95-MeV peak in the direct spectrum from our target. As remarked in the introduction to this chapter, the angular distribution data has been used to rule out $J = 0$ as a possible spin assignment.

The p-γ angular correlation reported here is different from that reported in reference (Go61). However, the interpretation is highly controversial since the details of the reaction process may be responsible for the observed correlations. The theory of Huby et al (Hu58) predicts that distortion effects tend to reduce the anisotropy measured in the reaction plane from that derived assuming a plane wave theory. From this point of view, the present correlation work was not done under the best conditions of bombarding energy and proton-detector angle.

The interpretation of the angular correlation would require a knowledge of the reaction mechanism. However, if the plane-wave theory of stripping holds in this reaction, then the correlation is interpretable by assuming an (n,γ) process in which the angular momentum of the captured neutron is known. This simplified interpretation will give a basis for discussion.

The angular distributions of the protons from the reaction $B^{11}(d,p)B^{12}$ are consistent with $l_n = 1, 1$ and 0 for the ground, first and second excited states respectively (Go61). Consider the

p-γ angular correlation of the 0.95-MeV state and assume the
(d,pγ) reaction can be represented as an (n,γ) process. With
this assumption the correlation angle, θ, is measured from the
nuclear recoil axis and the theoretical angular correlation is

$$W(\theta) = 1 + 0.343P_2(\cos\theta) \tag{2.1}$$

for $J_o = 3/2$, $\ell_n = 1$, $J_i = 3$, $L_\gamma = 2$ and $J_f = 1$. If $J_i = 2$ is
assumed, then $L_\gamma = 1$ and 2 are allowed as well as two possibilities
for the channel spin. The angular correlation then becomes

$$W(\theta) = 1-0.35P_2 - \delta\, 1.56P_2 + \delta^2 \left(1+0.25P_2\right)$$
$$+t\left\{1+0.35P_2 + \delta\, 1.56P_2 + \delta^2\left(1-0.25P_2\right)\right\} \tag{2.2}$$

where: δ = the quadrupole to dipole amplitude ratio. The
sign of δ differs from that used by Sharp, Kennedy,
Sears and Hoyle (Sh54).

  t = the channel spin mixing ratio, i.e. the intensity
for S = 2 divided by the intensity for S = 1.

The third possibility for J_i is 1, which gives the theoretical
angular correlation

$$W(\theta) = 1-0.25P_2 + 1.5\,\delta\, P_2 + \delta^2(1-0.25)P_2$$
$$+t\left\{1+0.05P_2 - 0.30\,\delta\, P_2 + \delta^2(1+0.05P_2)\right\} \tag{2.3}$$

Wilkinson (Wi61) has suggested that (d,p) and (d,n)
reactions should show nearly Butler stripping patterns at low

deuteron energies if the Q-value is low. Since the Q-value for
the 0.95-MeV state is 0.195 MeV and the bombarding energy was
1.5 MeV the above conditions are satisfied, and the (n, γ) assump-
tion may be a reasonable one. However, other theoretical calcula-
tions by Gibbs and Tobocman (Gi60) do not support this.

A recent paper by Robson and Weigold (Ro63) shows that
the observed angular distribution of the ground-state protons from
the $B^{11}(d,p)B^{12}$ reaction can be explained only by distorted-wave
analysis, provided a strong spin-orbit force is included in the
potential. The work was done at low bombarding energies $(E_d \sim 1 \text{ MeV})$.
The proton group to the first excited state could not be studied
thoroughly (as in the present investigation) because of inter-
ference from other reactions. The limited experimental results for
the 0.95-MeV state cannot distinguish between a plane-wave fit
and a distorted-wave analysis.

If a strong spin-orbit interaction is present, as implied
above, then the p-γ correlation is affected since the channel spin
mixing ratio, t, in equations (2.2) and (2.3) depends on the coup-
ling scheme. If we again resort to the simple (n, γ) model and
assume j-j coupling (as implied by the spin-orbit force), the
theoretical correlation is isotropic for $J^{\pi} = 2^{+}$ and pure M1 gamma
radiation. In other words, in formula (2.2), t is equal to
unity if j-j coupling is assumed. Thus, the observed angular
correlation is not inconsistent with the observed lifetime and
the strong $\vec{\ell}.\vec{s}$ force assumed in the stripping analysis. However,
it is doubtful that any significance can be attached to this.

From their measurement of the lifetime of the 0.95-MeV state, Warburton and Chase (Wa63) have been able to deduce an upper limit on the gamma-ray quadrupole-to-dipole amplitude ratio. They estimate $\delta^2 \leq 0.02$. They were then able to use the p-γ correlation observed at E_d = 5.5 MeV (see Table 2.1) to show that J = 1 is an unlikely assignment. This approach to interpretation is given with additional details, below.

If $J^{\pi} = 1^+$ is assumed for the spin of the first excited state, then equation (2.3) holds if plane wave theory is used to interpret the correlation. Knowing $\delta^2 < 0.02$, but not knowing the sign of δ, two limits for W(θ) are obtained:

If $\delta = +0.14$

$$W(\theta) = 1 - 0.043P_2 + t(1 + 0.008P_2)$$

If $\delta = -0.14$

$$W(\theta) = 1 - 0.463P_2 + t(1 + 0.092P_2)$$

Therefore the coefficient of $P_2(\cos\theta)$, A_2, can be calculated as a function of t for the two limits of δ. A graph of this relation is shown in Fig. 2.10. The line for $\delta = 0$ is also shown. It is seen that the value of A_2 obtained by Gorodetzky et al does not overlap with the prediction for any value of t, since only the region bounded by the two limiting loci is acceptable for $\delta^2 \leq 0.02$.

Similarly, if $J^{\pi} = 2^+$ is assumed, the angular correlation (2.2) has the limiting values

$$W(\theta) = 1 - 0.55P_2 + t(1 + 0.55P_2)$$
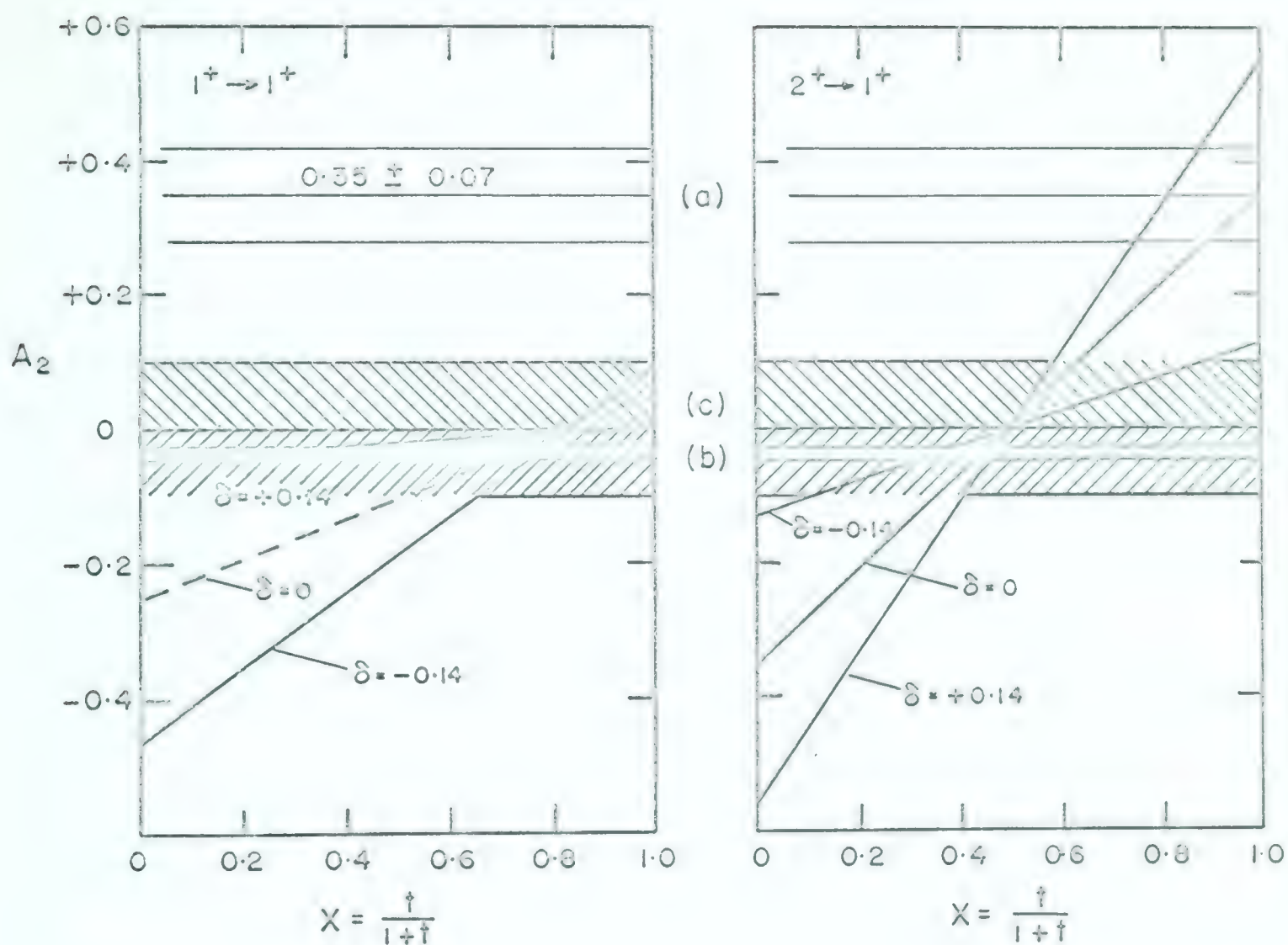
FIGURE 2.10

Summary of the Angular Correlation Results on
the 0.95-MeV State

The value of A_2 is plotted as a function of the
channel spin mixing ratio, t. The limits imposed by
$\delta^2 \leq 0.02$ are shown. Experimental results are also
plotted:

a) $A_2 = +0.35 \pm 0.07$ (Go61)

b) $A_2 = -0.035 \pm 0.01$ (Wa63); Ang. Distr.

c)   Isotropic   (Present work)

and

$$W(\theta) = 1-0.125P_2 + t(1+0.125P_2)$$

for $\delta = +0.14$ and -0.14 respectively.

It is seen from the second graph in Fig. 2.10 that the allowed positive values of A_2 are sufficiently large to overlap with the measured value, $+0.35 \pm 0.07$.

The result from the present investigation of the p-γ correlation is also plotted in Fig. 2.10, along with the A_2 coefficient measured by Warburton & Chase for the angular distribution. Although these two measurements cannot distinguish between $J = 1$ and $J = 2$, they do overlap the allowed values. The question arises as to whether the fact that the angular distribution has a negative value for A_2 is consistent with the positive value from the p-γ correlation, within the framework of this simplified interpretation.

In the $B^{11}(d,p)B^{12}$ reaction, the recoil axis is always in the forward direction. Thus the symmetry axis for the p-γ correlation is always $< 90^\circ$. Therefore, if the angular distribution is assumed to be a weighted average of the p-γ correlation, the sign of the anisotropy cannot change. If the measurement at high energies is taken as being close to the plane-wave limit, then A_2 should remain positive since distortion effects can only reduce the anisotropy. Thus the two measurements are inconsistent for the interpretation given. It would seem necessary to use a more general theory to explain the experimental data.

From Fig. 2.10, the limit on δ^2 and $A_2 = 0.35 \pm 0.07$ restricts $t \geqslant 3$. As mentioned before, pure j-j coupling predicts $t = 1$. In the theoretical review by Macfarlane and French (Ma60), it is pointed out that the reduced width obtained from the $B^{11}(d,p)B^{12}$ stripping reaction is consistent with j-j coupling. They also point out that the absolute reduced width, however, is smaller than expected by a factor of about two. The nucleon width for the 16.10-MeV level in C^{12} corresponds to that for the 0.95-MeV state in B^{12}(La60). The 16.10 MeV level has $T = 1$, $J^{\pi} = 2^+$ and is believed to be the isobaric analogue corresponding to the 0.95-MeV state in B^{12}.

In conclusion, the spin assignment $J = 2$ is favoured for the 0.95-MeV state. But this assignment has been made by the elimination of other spin possibilities. Ruling out $J = 0$ by using the anisotropy argument of the angular distribution of the gamma rays does not have to be invoked. The probability of $\ell = 1$ neutron capture to a state with $J = 0$ is very small (Aj59), and both the 0.95-MeV state and the ground state show $\ell_n = 1$ capture for the (d,p) reaction. The assignment $J = 3$ is ruled out by the lifetime measurement. Finally, the choice between $J = 1$ or $J = 2$ is made by assuming (1) the $(d,p\gamma)$ reaction can be described as an (n,γ) reaction when the bombarding energy is high (5.5 MeV) and the protons are observed on the stripping peak, and (2) $\delta^2 \leqslant 0.02$, as estimated from the lifetime and E2 sum rules (Wa63).

The branching ratio of the 1.67-MeV state does not provide the possibility of deciding between $J^{\pi} = 1^-$ or 2^- for

the 1.67-MeV state, since the assignment $J^{\pi} = 2^{+}$ is favoured for
the 0.95-MeV state.

CHAPTER 3

THE 3.06- AND 3.   eV STATES OF OXYGEN-17

3.1 Introductory Remarks

In Chapter 1 the importance of the single-particle nature of the low lying positive parity levels of O^{17} was briefly mentioned. Studies of deuteron induced stripping and pick-up reactions (Ke61, Ar61) leading to excited states of O^{17} have been successful in identifying the single-particle states by their spins, parities and large reduced widths. However, the negative parity states at 3.06- and 3.85-MeV presented difficulties in interpretation.

Since the 3.85-MeV level is a negative parity state, the interpretation in terms of a single-particle picture is that this state is a 1f7/2 neutron coupled to the doubly magic O^{16} core. Similarly the 3.06-MeV level could be interpreted as a 2p1/2 or p 3/2 neutron state. While these levels do exhibit stripping patterns that allow assignments to the parity and ℓ_n, the reduced widths relative to the reduced widths of the positive parity ground state are small.

Theoretical considerations (Ma60) indicated that the (1/2⁻) state at 3.06-MeV is due to excitation of core particles and the 3.85-MeV state is probably an f7/2 state if the spin 7/2 is assumed.

The experimental spin assignments from the stripping data limited the values to (1/2⁻, 3/2⁻) and (5/2⁻, 7/2⁻) for the 3.06- and 3.85-MeV levels respectively, since angular distribution

patterns were characteristic of $\ell = 1$ and 3 respectively, (Ke61, Ar61). The 3.86-MeV level in the mirror nucleus, F^{17}, was believed to have $J^{\pi} = 7/2^-$ from elastic scattering measurements using the $O^{16}(p,p)O^{16}$ reaction (La51), supporting the $7/2^-$ assignment for O^{17}. However, the assignment in F^{17} can be considered inconclusive due to the narrow width of the state (Ha62). The $J = 1/2$ spin assignment for the 3.06- MeV level is supported, since the analogue state at 3.10 MeV in F^{17} has spin $1/2^-$ from the elastic scattering data.

To obtain more information on the 3.06- and 3.85-MeV states of O^{17}, a study has been made by exciting O^{17} with the $C^{14}(\alpha,n)O^{17}$ reaction and measuring the n-γ angular correlations. Using the same reaction, the Doppler shift attenuation factors for the 3.85- and 2.19-MeV gamma-rays from the 3.85- and 3.06-MeV levels respectively were measured to obtain estimates of the nuclear lifetimes.

Litherland, Ferguson and McCallum (Li60, Li61) have shown theoretically and experimentally demonstrated that the interpretation of particle-γ-ray angular correlations can be greatly simplified if suitable restrictions can be imposed on the geometry and the reaction populating the states. This type of triple angular correlation measurement has been used in the present investigation to obtain unique assignments for the spins of the two levels under study. It would be beyond the scope of this thesis to discuss in a general way the theory of triple angular correlations. However, for the interpretation of the experimental results, the following plausibility

argument will suffice.

By using an axially symmetric detector to observe the particles emerging at $0°$ (or $180°$), a selection of aligned nuclear states is obtained. The population of the magnetic substates is restricted by the spins of the bombarding and emerging particles and the target nucleus. In the $C^{14}(\alpha,n)O^{17}$ reaction, only the $m = \pm 1/2$ magnetic substates of the levels of the residual nucleus are selected by observing the neutrons with an infinitely small detector at $0°$. In other words, the compound states of O^{18} are formed with zero component of angular momentum along the beam axis since the entrance channel-spin is zero. Therefore, the projection of the total angular momentum of the neutrons emerging along the same axis is $\pm 1/2$, since $\vec{\ell}_n$ is perpendicular to the momentum vector. Thus the residual states in O^{17}, formed by the emission of these particular neutrons, have an angular momentum projection of $\pm 1/2$ on the beam axis. If s-wave neutrons are emitted, then the states are aligned independently of the direction in which the neutrons emerge, and observation of the neutrons becomes unnecessary.

The angular dependence of the intensity of the coincident γ-rays, measured in a plane containing the beam axis, can now be described by two unquantized quantities, viz. the population, $P(1/2) = P(-1/2)$, of the $m = \pm 1/2$ substates and the multipole mixing ratio, δ, of the emitted γ-rays, and the quantized observables of interest, viz. J_i, J_F, etc.

The angular correlation in a plane at right angles to the beam axis is isotropic since the probability of emission of a γ-ray in a given direction depends on the orientation of the spin of the nuclear state with respect to the direction of emission of the γ-ray. Clearly, cylindrical symmetry is present for a geometry with a point neutron detector at 0° or 180°.

The above brief description of the triple angular correlation experiment has been specialized to our particular needs for the sake of simplicity. A full description of the method can be found in the papers by Litherland et al (Li60, 61). The effect of the finite solid angle of an actual neutron detector has been discussed in (Li60) and more generally in (Li63). The effect of the finite solid angle of the detector is to add contributions to the angular correlation from higher magnetic substates.

Experimentally, the correlation is measured in a plane containing the beam axis to obtain the nuclear information. An isotropic correlation is enforced in the plane perpendicular to the beam axis by using a neutron detector with cylindrical symmetry. The effect of its finite size and other imperfections is estimated by studying the correlations as a function of the solid angle.

Although the experimental problems of using a neutron detector at 180° require special consideration, the problems of using the detector at 0° are less extreme. In this investigation, a small cylindrical stilbene detector was used close to the target and at 0°. Gamma rays observed at this angle had to pass through the neutron detector to reach the γ-ray detector. A NaI(Tl)

gamma-ray spectrometer was used to identify the desired transitions induced by the $C^{14}(\alpha, n\gamma)0^{17}$ reaction.

The Doppler-shift method of measuring nuclear lifetimes is discussed in Chapter 5 with reference to this experiment.

3.2 Experimental Apparatus and Procedures

The Chalk River tandem Van de Graaff was used to provide approximately 0.4 μA of 7.1- to 8.6-MeV He^4_{++} ions. The target consisted of a C^{14}- enriched ($\sim 25\%$) carbon layer on a tantalum backing thick enough to stop the bombarding beam.

The neutrons were detected in a 1 1/2 in. long by 1 in. diam. stilbene crystal mounted with its cylindrical axis at 0° to the beam. To obtain optical coupling to a Dumont 6292 photomultiplier in an arrangement that left a minimum amount of material at 0°, the stilbene was placed in a cylindrical aluminium container such that the crystal's axis was at right angles to the container's axis. Optical coupling was then made by filling the container with silicone fluid and inserting the photomultiplier into the container to bring the photocathode into contact with the fluid. Then, the whole assembly was mounted rigidly to the target chamber with the offending photomultiplier at right angles to the beam, but the crystal axis lined up with the beam axis. The gamma-ray counter was a 5 in. diam. by 6 in. long NaI(Tl) crystal mounted on the arm of an angular correlation facility capable of locating the crystal at (r, θ, φ) in an orientation with the crystal axis pointing at the target (origin of the coordinates r, θ, and φ). Intensity measurements at each angle were monitored by a second NaI(Tl) crystal in a fixed position.

The electronic apparatus consisted of a modified fast-slow coincidence system in which one fast channel of electronics serves both γ-ray detectors. Then, one time-to-amplitude converter is used to measure the time relations between the signal from the stilbene neutron detector and both γ-ray detectors. By inserting equalizing delays, one fast coincidence signal is obtained that involves a single resolving time ($2\tau \simeq 30$ns) for both the measuring and monitoring channels. At first sight, this arrangement may appear to increase the random coincidence rate, but it is no worse than normal operation using a multi-parameter kicksorter for analysis of the slow linear signals gated by the fast coincidence requirement.

The pulse-amplitude analysis of the signals from the detectors involved the following:

(1) The pulses from the two γ-ray detectors were analysed in two separate 100-channel kicksorters having digital pulse-amplitude stabilizers (La61). These instruments apply a correction voltage to the photo-multiplier to stabilize the gain of the system. The correction is obtained from digital comparators after pulse-amplitude conversion so that a reference peak in a spectrum can be maintained in a specified group of channels.

(2) Another 100-channel analyser monitored the output of the time-to-amplitude converter, and dis-played the time relation of the events detected by the counters.

(3) The pulse-amplitude distributions from all three detectors were analysed simultaneously in a 900-channel multi-parameter analyser to produce nine 100-channel coincidence spectra (A162). One group of 100

channels contains a spectrum of the pulses from the stilbene neutron counter in time coincidence with all γ-rays detected in both NaI counters. Four digital single-channel analysers were set on this distribution to select four portions ("windows") of the spectrum. Each window on the neutron spectrum imposes a further selection that produces four γ-ray spectra from the 5 in. by 6 in. NaI detector and four spectra from the fixed monitor. These eight spectra each have 100 channels of resolution.

The ungated gamma-ray spectrum observed when bombarding the C^{14}-enriched target with 8.05-MeV alpha particles is shown in Fig.3.1. This complex spectrum is mainly composed of 4.43-MeV radiation from the $C^{12}(\alpha,\alpha')C^{12}$ reaction and the gamma-rays of interest from the $C^{14}(\alpha,n)O^{17}$ reaction to the 3.85- and 3.06- MeV states. Subtraction of contributions from the 4.43-MeV γ-ray (shown as a broken line in Fig. 3.1) reveals the 3.85-MeV full-energy peak. The full-energy peak of the gamma ray from the $3.06 \rightarrow 0.87$ transition is also present. The n-γ correlations and the Doppler shift measurements of the 3.85-MeV level were made at a bombarding energy of 8.05 MeV. At this energy the ratio of the 3.85-MeV to the 4.43-MeV γ-ray intensity proved to be optimum for coincidence measurements.

The measurements on the 3.06-MeV level were made at a bombarding energy of 7.2 MeV, which is below the threshold for the reaction to the 3.85-MeV level. A measurement of the yield of the 3.85-MeV radiation was consistent with the threshold of 7.29 MeV for the $C^{14}(\alpha,n)O^{17}$ reaction to the 3.85-MeV state.
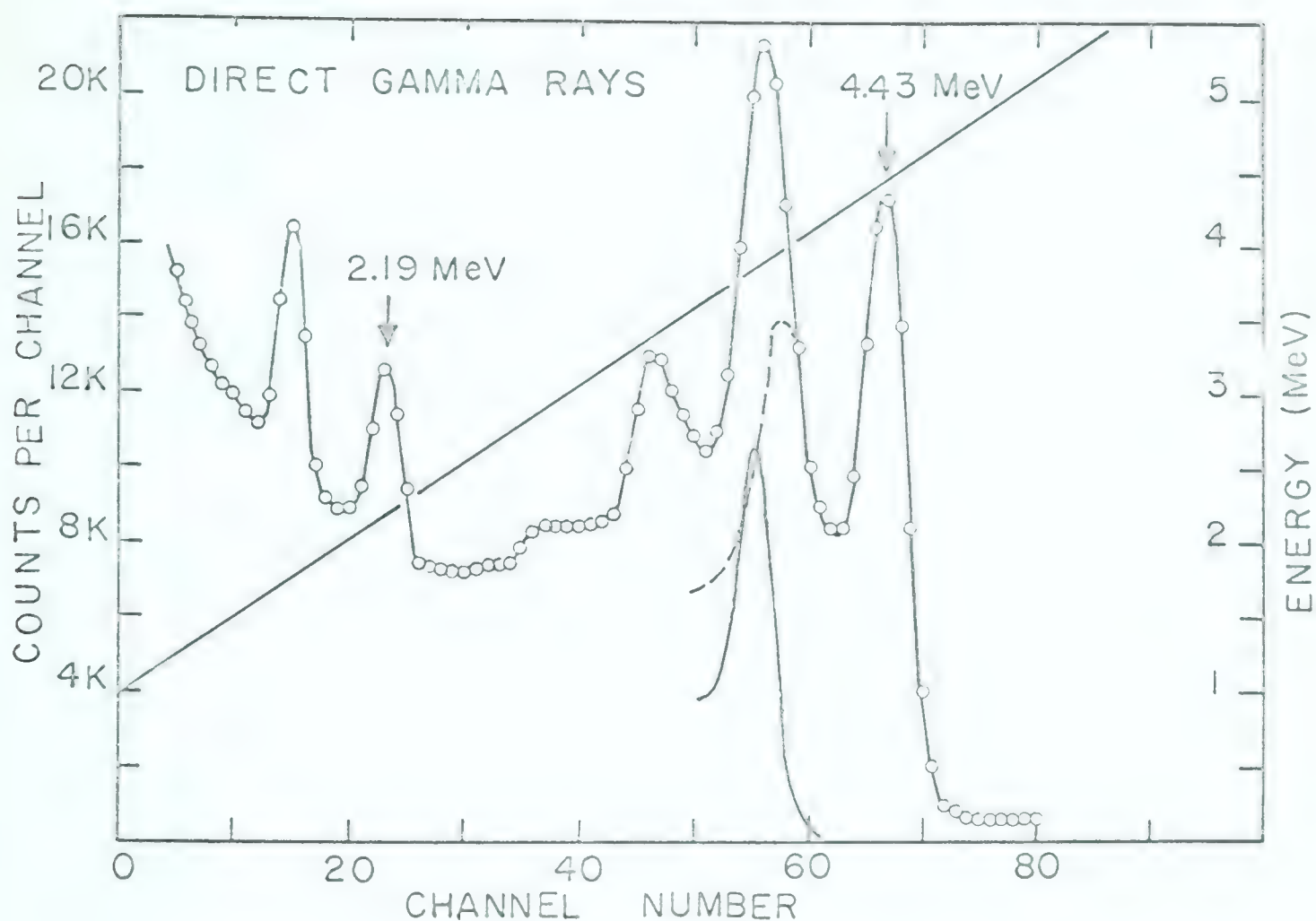
FIGURE 3.1

The direct γ-ray spectrum obtained in the 5 in.
diam. by 6 in. long NaI(Tl) detector when bombarding
the C^{14}-enriched target with 8.05-MeV alpha particles.
The spectrum shows (1) 4.43-MeV radiation from
$C^{12}(\alpha, \alpha')C^{12}$ (2) 3.85-MEV radiation from the 3.85-
MeV level of O^{17} and (3) 2.19-MeV radiation from the
3.06-MeV level of O^{17}. The broken curve shows the
line shape of the 4.43-MeV γ-ray in the region of the
first escape peak. The presence of the 3.85-MeV full-
energy peak is apparent when the counts from the 4.43-
MeV γ-ray are subtracted.

The lack of pronounced structure in the direct gamma-ray spectrum in the region between 2.3 to 3.2 MeV (see Fig. 3.1) proved fortunate for the Doppler shift runs. For these measurements, a RdTh source was attached to the container of the gamma-ray detector to insert a prominent reference peak in the flat region of the spectrum. The gain of the system was then stabilized on the 2.62-MeV peak from the source.

The presence of the 4.43-MeV radiation, however, proved troublesome in the n-γ correlation work. It contributed the major part of the background under the 3.85-MeV full-energy peak. This background arose from true coincidences due to the γ-rays scattering between the stilbene and NaI crystals. The elimination of these coincidences by pulse-shape discrimination in the stilbene detector was impractical because of the low energy of the neutrons, i.e. the statistical uncertainty in the shape of the pulses makes discrimination with good efficiency a difficult task. By measuring the coincidence spectra at all angles from the $C^{12}(\alpha, \alpha')C^{12}$ reaction using an elemental carbon target under identical conditions as the $C^{14}(\alpha,n)O^{17}$ correlation measurement, the spectral shape and intensity of the scattered radiation relative to the direct intensity of the 4.43-MeV radiation was determined. These data were normalized to the ungated yield of 4.43-MeV radiation from the C^{14} target giving the intensity correction to be subtracted from the n-γ coincidence spectra. The largest correction, of course, is at 0° where the γ-ray detector is "shadowed" by the stilbene crystal.

A correction factor for the anisotropic absorption of γ-rays was obtained by measuring the angular distribution of 2.31-MeV γ-rays from the $C^{14}(p,n\gamma)N^{14}$ reaction with the stilbene detector in place.

3.3 Experimental Results

Figure 3.2 shows a coincidence gamma-ray spectrum taken at a bombarding energy of 8.05 MeV. The 3.85-MeV gamma-ray is clearly observed as well as the weaker 2.19-MeV full-energy peak. The background from degraded 4.43-MeV gamma-rays is apparent just above the 3.85-MeV full-energy peak.

Figure 3.3 is a coincidence spectrum observed at 7.2 MeV bombarding energy where the 2.19- and 0.87-MeV gamma rays are observed without exciting the 3.85-MeV level. Pulse-shape discrimination in the stilbene detector was used to reduce unwanted γ-γ coincidences.

A schematic drawing of the detector geometry used for measurements of the angular correlations and distributions is shown at the top of Fig. 3.4. The graph shows the angular distribution of direct 3.85-MeV gamma-rays observed at 7.7 MeV bombarding energy.

The n-γ correlations for the 3.85-MeV level were obtained for two distances of the neutron detector (see Fig. 3.4). The intensity of the full-energy peak, i.e. the area under the peak, was normalized to the intensity in the corresponding peak in the monitor detector after corrections for the background and the scattering effect had been made. The anisotropy correction from $C^{14}(p,n\gamma)N^{14}$ data was then applied at each angle to give the
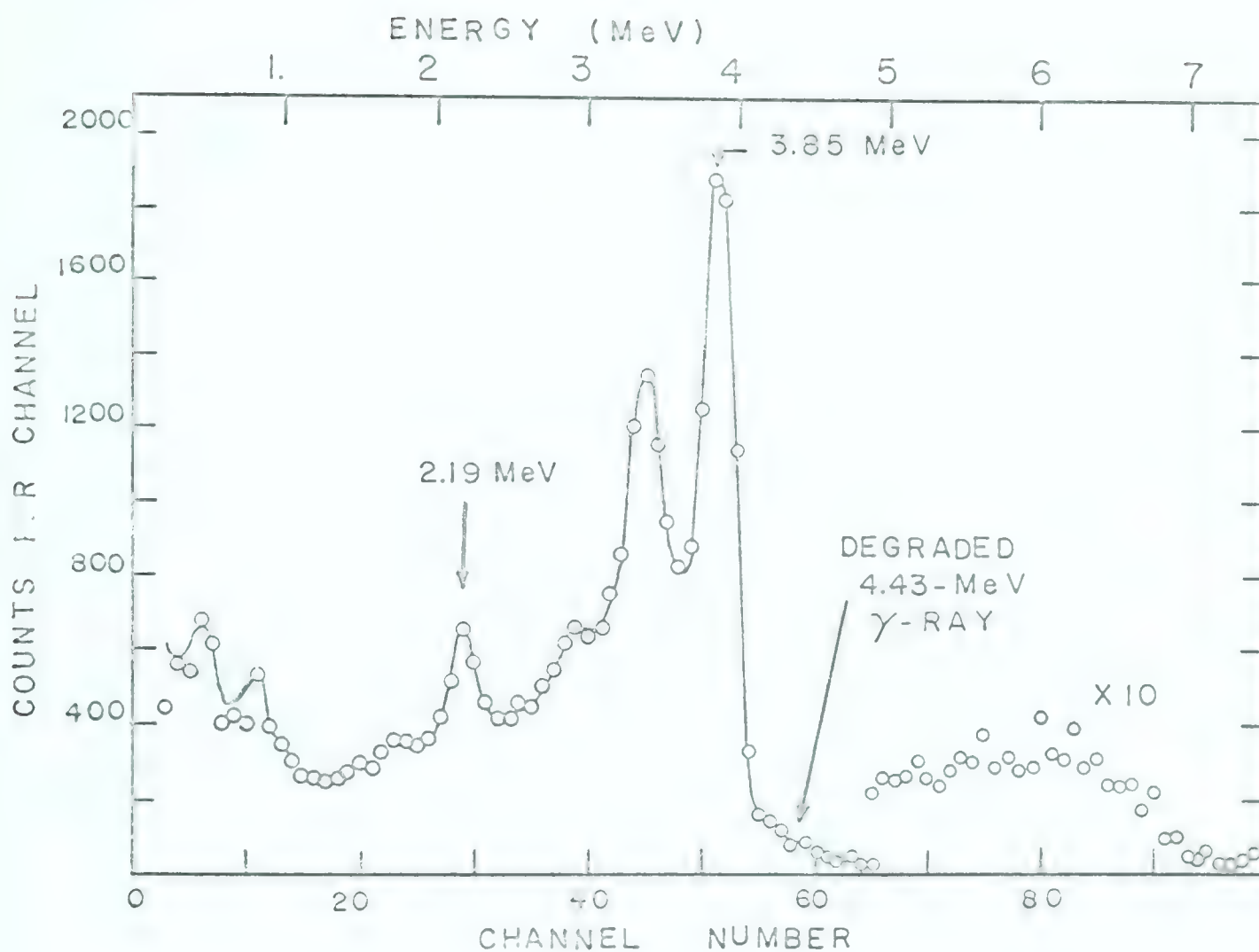
FIGURE 3.2

An n-γ coincidence spectrum taken for 8.05-MeV He^4 incident on a C^{14} enriched target. The gamma rays from the 3.846-and 3.058-MeV states of 0^{17} are evident in this spectrum taken with the neutron detector at 0° and the gamma-ray detector at 90°. The background just above the 3.85-MeV peak is due to 4.43 MeV radiation from the C^{12}(α, α')C^{12} reaction.
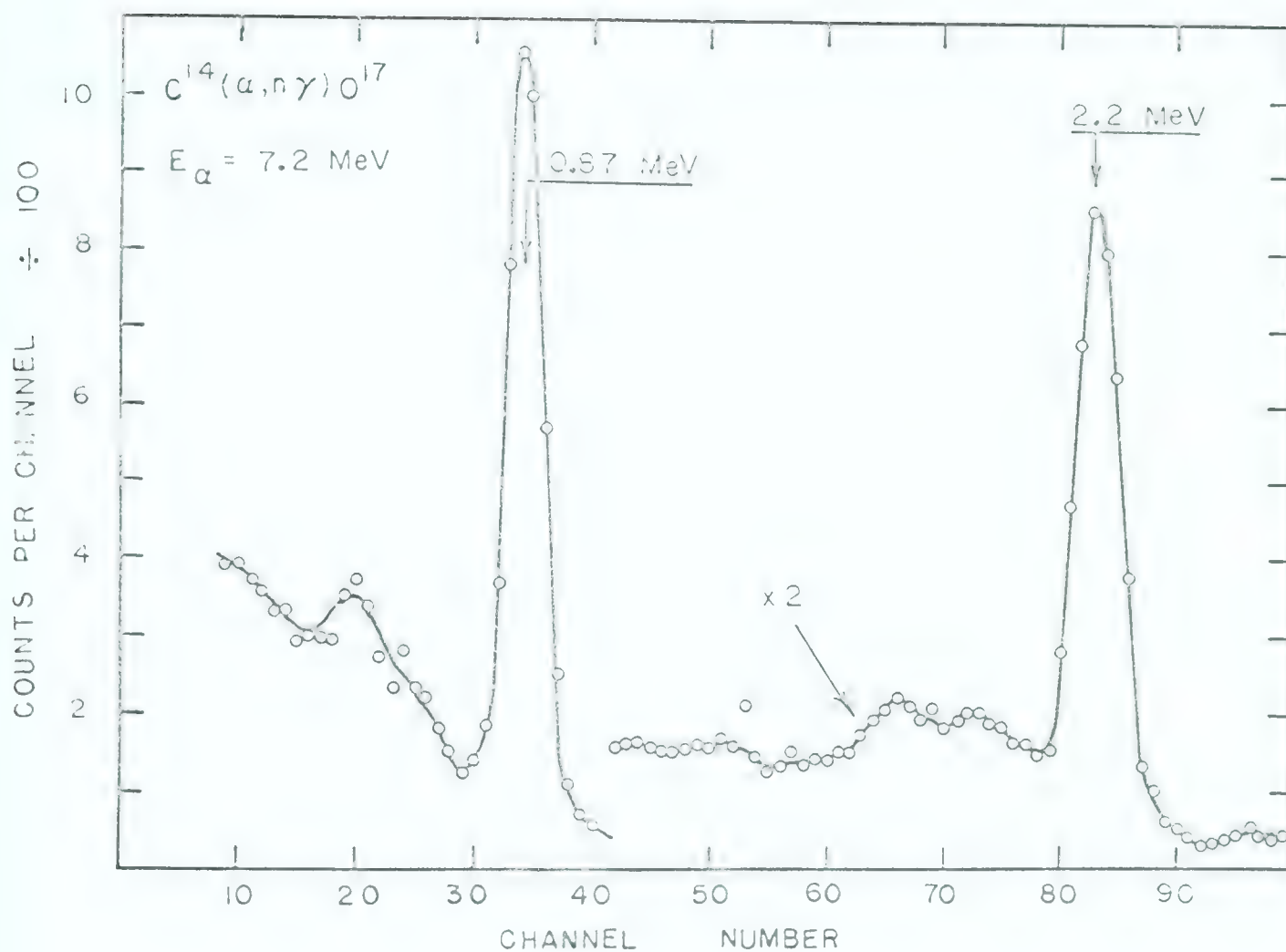
FIGURE 3.3

The spectrum shows the gamma radiation in coinci-
dence with neutrons from $C^{14}(\alpha,n\gamma)O^{17}$ at 7.2 MeV
bombarding energy. The 2.19-and 0.87-MeV gamma rays
are seen from the decay of the 3.06-MeV level through
the 0.87-MeV level of O^{17}. Unwanted $\gamma-\gamma$ coincidences
have been reduced by pulse-shape analysis of the pulses
from the stilbene crystal.

AXIALLY SYMMETRIC
NEUTRON DETECTOR
1 IN. X 1½ IN. STILBENE

L₂

α PARTICLES

θ

L₁

NaI(Tl)

5 IN. X 6 IN.
γ-RAY
DETECTOR

$1 + 0.37 P_2 (\cos \theta)$
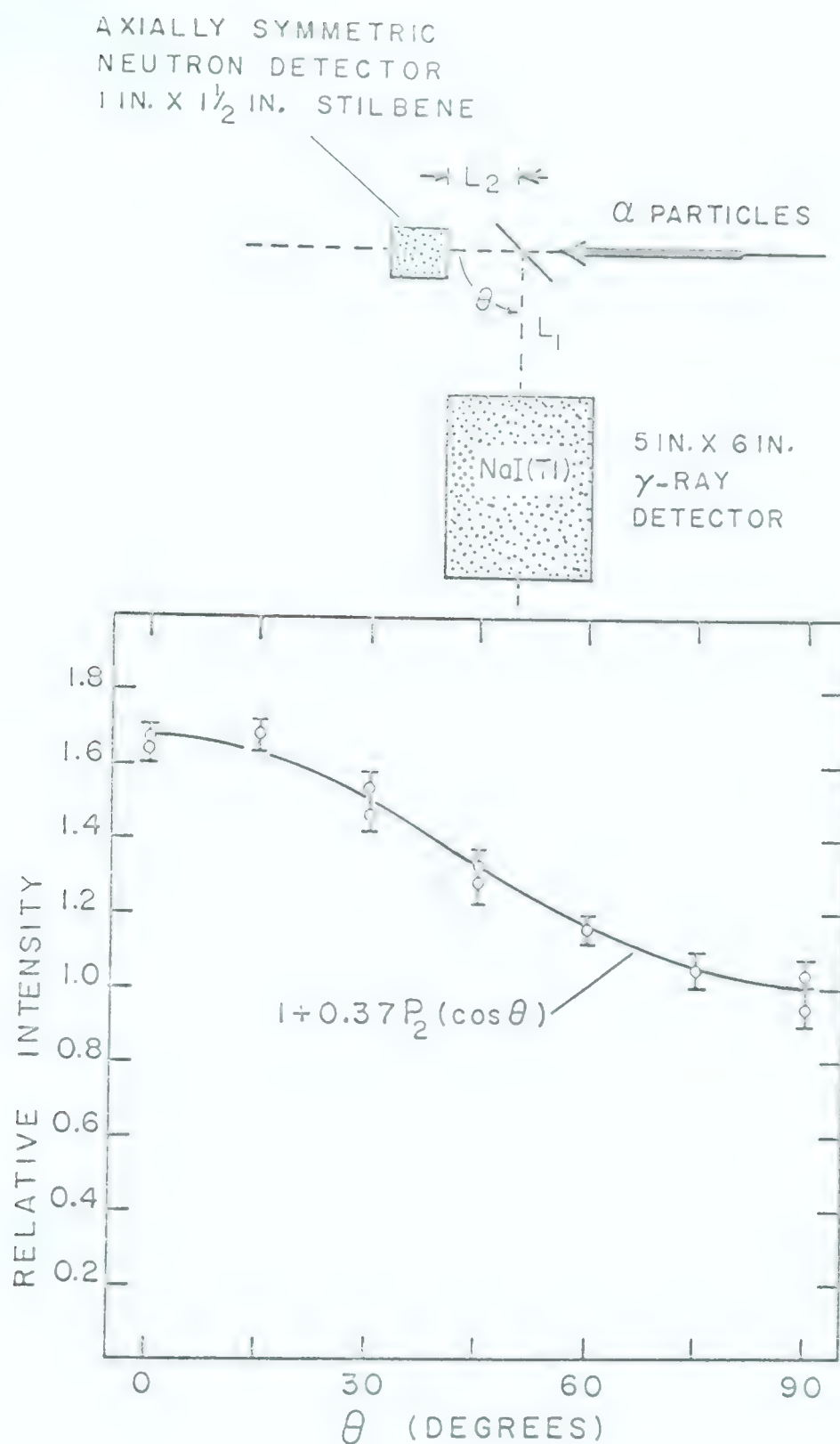
FIGURE 3.4

The geometry of the detectors used for the investi-
gation of n-γ coincidences and for the measurement of
angular correlations and distributions is shown at the
top of the figure. The graph is a measurement of the direct
angular distribution of 3.85-MeV radiation observed at
E_α = 8.05 MeV. The stilbene detector was removed for this
measurement. In the figure, L_2 = 4.5 or 7.0 cm and L_1 = 15 cm.

final values for the relative intensity. One of the correlations is shown in Fig. 3.5. The results of all n-γ correlations and the angular distribution for the 3.85-MeV state are summarized in Table 3.1.

	E (MeV)	φ	L_2(cm)	L_1(cm)	A_2	A_4
	8.05	0	4.5	15	+0.30±0.03	
	8.05	90	4.5	15	+0.34±0.03	
n-γ	8.05	0	7.0	15	+0.42±0.06	+0.13±0.07
	8.05	90	7.0	15	+0.44±0.03	+0.11±0.04
γ	8.05	0		15	+0.39±0.03	
	7.70	0		15	+0.37±0.01	

Notes 1. L_1 = the distance from the target to the
           front face of the NaI detector.

      2. L_2 = the distance from the target to the
           front face of the stilbene detector.

      3. A_2 and A_4 are the coefficients of $P_2(\cos\theta)$
           and $P_4(\cos\theta)$ after correction for
           the finite solid angle of the NaI
           detector using the correction factors
           of Twin and Wilmott (Tw62).

Least Square Analysis of the Correlation Data

TABLE 3.1
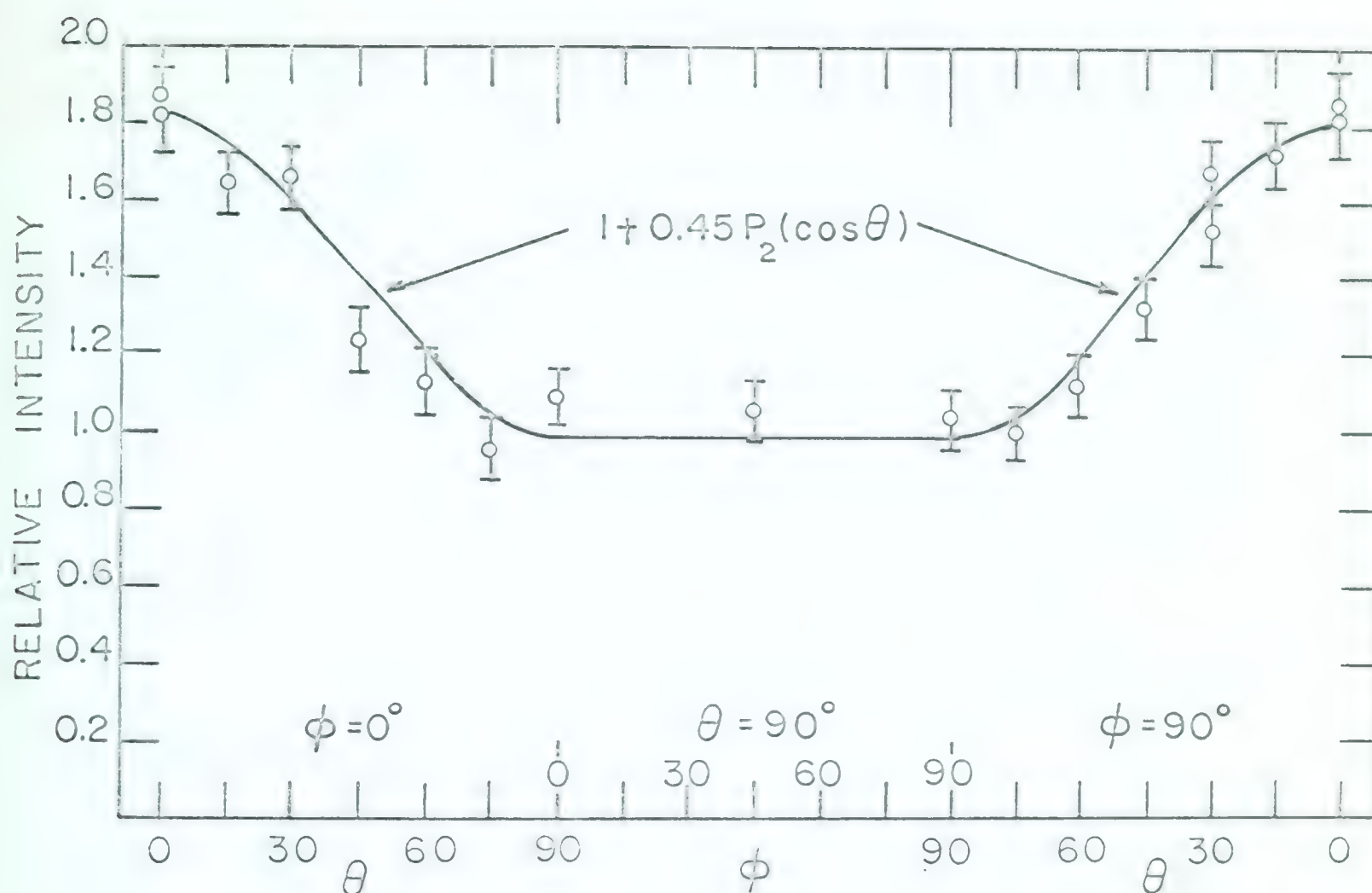
FIGURE 3.5

An n-γ Angular Correlation

The data were obtained with an axially symmetric
neutron detector at 0° to the 8.05-MeV alpha-particle
beam. The data points have been corrected for aniso-
tropic absorption and for the scattering effects as dis-
cussed in the text. The diagram illustrates the measure-
ments over the edges of an octant of a sphere centered
on the C^{14} target. $\phi = 0°$ defines a horizontal plane
containing the beam.

It is seen that the angular distribution and the n-γ correlation for the 3.85-MeV state are nearly the same. This implies that the emitted neutrons are s-wave. Therefore, the predicted n-γ correlation is independent of the direction of the neutrons and the angular correlation and distribution are the same function. Assuming all correlations are the same, the average value of A_2 from all measurements is $\div 0.40 \pm 0.03$. The individual correlations are not sufficiently accurate to give a reliable value for A_4, in view of the corrections for the scattering of 4.43 MeV radiation.*

The n-γ correlation of the 2.19-MeV gamma ray from the 3.06-MeV state was isotropic.

An example of the data obtained in the measurement of the Doppler shifts is shown in Fig. 3.6. These spectra for the 3.85-MeV radiation were taken alternately at $\theta_\gamma = 135^\circ$ and 45° as shown in Fig. 3.6A. To check the consistency of the measurement, this procedure was repeated. The shift in the energy of the gamma ray was obtained by normalizing the spectra such that the full-energy

---

*Note: C. Broude and A. E. Litherland have further checked that $\ell_n = 0$ is the correct assumption by measuring the n-γ correlation for $\theta_n = 45^\circ$, and found the same correlation. They then analysed all four correlations simultaneously to fit five parameters, a common δ and four normalization coefficients, for each assumed value of J. With this analysis all correlations can be fitted with $\delta = 0.07 \pm 0.01$ for J = 5/2 or $\delta = -0.37 \pm 0.01$ for J = 7/2. The χ^2 of the fits obtained are consistent with the statistical errors and justify the assumption of identical correlations (Br63).
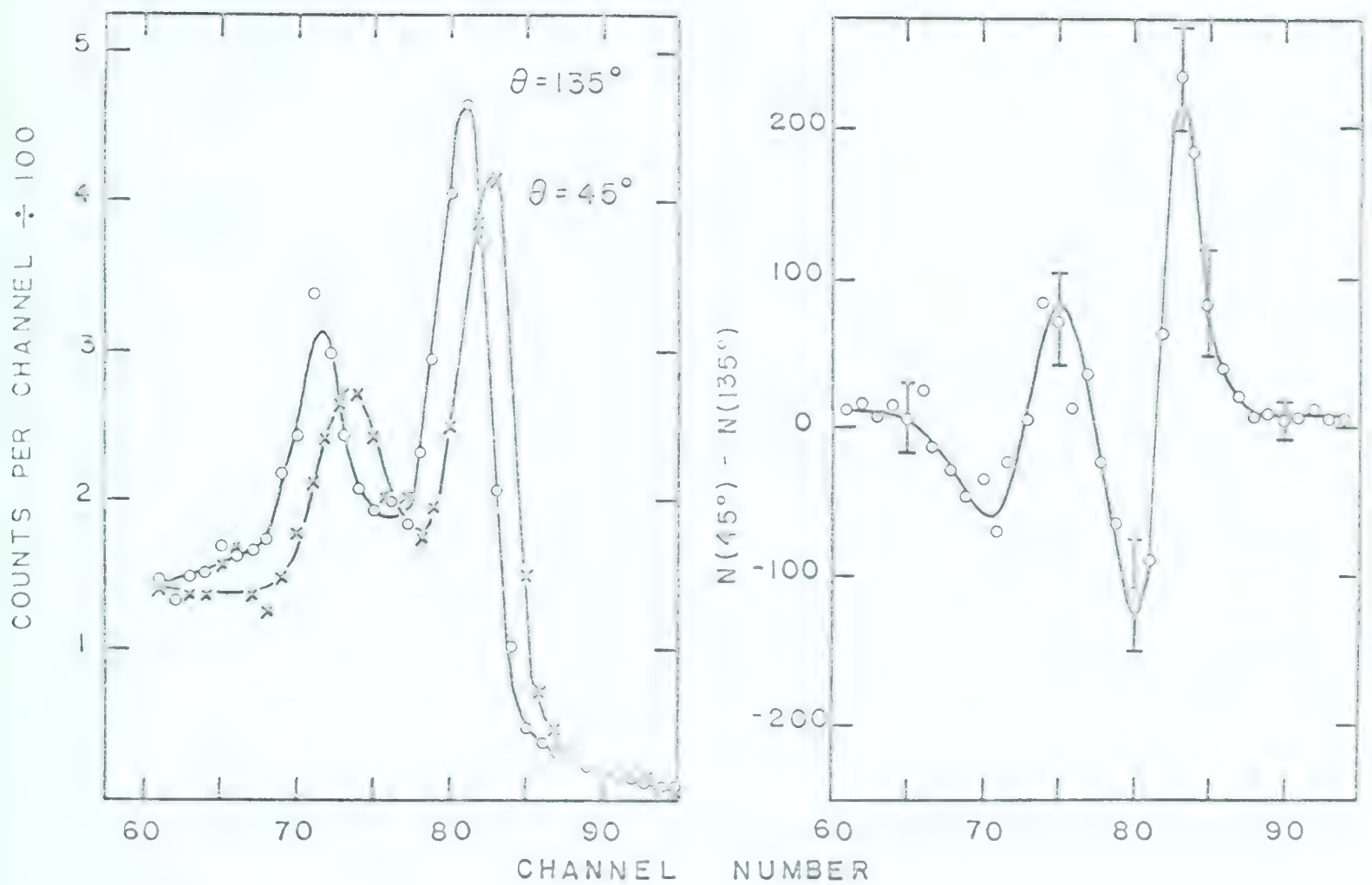
FIGURE 3.6

Doppler-Shift Spectra for the Measurement of the
Mean Lifetime of the 3.846-MeV level of 0^{17}

A. Spectra taken at $\theta_y = 45°$ and $135°$.

B. The difference of the spectra shown in A
after normalization to equal peak areas.

peaks have equal area, and subtracting them to give the difference spectrum shown in Fig. 3.6B. The shift is obtained by dividing the peak height of the spectrum by the area of the positive peak in the difference spectrum. Similar measurements were performed on the 2.19-MeV gamma ray from the 3.06-MeV state.

The percentage energy shift in the 2.19-MeV gamma ray was $(1.25\pm0.12)\%$ and the percentage shift in the 3.85-MeV gamma ray was $(1.94\pm0.12)\%$. The maximum fractional Doppler shift is $\sqrt{2}\,V_0/c$, where V_0 is the initial velocity of the recoiling O^{17} ions. From kinematic calculations, the values for V_0/c are 1.15% and 1.25% for the 3.06- and 3.85-MeV states respectively. Therefore, the experimental values of F, the Doppler shift attenuation factor, are 0.77 ± 0.07 and 1.06 ± 0.07 respectively. F is the ratio of the observed shift to the maximum shift (see Chapter 5).

The extraction of the nuclear lifetime from F requires a knowledge of the characteristic stopping time for O^{17} ions recoiling into the target and its backing material. The characteristic stopping times for O^{17} ions in carbon and tantalum have been obtained from the published data on the stopping power of carbon and gold for O^{16} ions (Po61). A complete analysis of the data to yield the nuclear mean lifetime is given in Chapter 5. The final values for the mean lifetimes are $\leq 0.25 \times 10^{-13}$ sec. for the 3.85-MeV transition and $1.2^{+0.9}_{-0.6} \times 10^{-13}$ sec. for the 3.06- to 0.87-MeV transition.

3.4 Summary of Results

The theory of triple correlations predicts a distribution of the form (Li61)

$$W_{tt'}(\theta) = \sum_{k} A_k \, P_k(\cos\theta)$$

with k = 0, 2 and 4 for pure multipole radiation. For a mixture of dipole and quadrupole radiation, the total distribution is a sum of $W_{tt'}$

$$W(\theta) = W_{11}(\theta) \div 2\delta W_{12}(\theta) + \delta^2 W_{22}(\theta)$$

where δ is the quadrupole-to-dipole amplitude ratio. The subscripts on $W_{tt'}(\theta)$ refer to the multipolarity of the gamma radiation.

For each J- value assumed for the state decaying by gamma ray emission, the correlation function is evaluated. Thus, for the 3.85-MeV state the transition is either $5/2^- \to 5/2^+$ or $7/2^- \to 5/2^+$, since the ground-state spin-parity of 0^{17} is known to be $5/2^+$.

For the $5/2^- \to 5/2^+$ case:

$$W_{11}(\theta) = 1 + 0.457 \, P_2(\cos\theta)$$

$$W_{12}(\theta) = \quad - 0.542 \, P_2(\cos\theta)$$

$$W_{22}(\theta) = 1 - 0.204 \, P_2(\cos\theta) - 0.368 \, P_4(\cos\theta)$$

For the $7/2^- \to 5/2^+$ case:

$$W_{11}(\theta) = 1 - 0.357 \, P_2(\cos\theta)$$

$$W_{12}(\theta) = \quad - 1.031 \, P_2(\cos\theta)$$

$$W_{22}(\theta) = 1 + 0.085 \, P_2(\cos\theta) + 0.653 \, P_4(\cos\theta)$$

A plot can be made of A_2 versus A_4 as a function δ, where A_2 and A_4 are the normalized coefficients of $P_2(\cos\theta)$ and $P_4(\cos\theta)$ respectively (i.e. coefficient of $P_o = 1$). This type of diagram is shown in Fig. 3.7 for the two spin values. The experimental value of A_2 is plotted on the graph and shows that the correlation measurement does not give a unique assignment for J. From the graph, for the $5/2^- \to 5/2^+$ case, $\delta = +0.05$, i.e. the radiation is almost pure E1, whereas for the $7/2^- \to 5/2^+$ case, $\delta = -0.40$, indicating a large component of M2 radiation. Note that the values of δ are the same as the values from the preferred analysis of Broude and Litherland.

The value of δ together with the lifetime estimate does allow abasis for unique assignment of J by comparing the experimental transition strength to the single-particle estimate. The intensity of M2 radiation relative to E1 is δ^2. Therefore, a measure of the matrix element for the decay is $|M|^2 \sim \Gamma_\gamma /(1+\delta^2)$ for the E1 component and $|M|^2 \sim \Gamma_\gamma \delta^2/(1+\delta^2)$ for the M2 component. Expressing $|M|^2$ in terms of the estimates of Weisskopf,

$$|M|^2 = \frac{1}{1+\delta^2} \quad \frac{\tau_{\gamma w(E1)}}{\tau_\gamma} \qquad \text{Weisskopf units}$$

$$|M|^2 = \frac{\delta^2}{1+\delta^2} \quad \frac{\tau_{\gamma w(M2)}}{\tau_\gamma} \qquad \text{Weisskopf units}$$

where τ_γ is the measured lifetime and $\tau_{\gamma w}$ is the Weisskopf prediction.
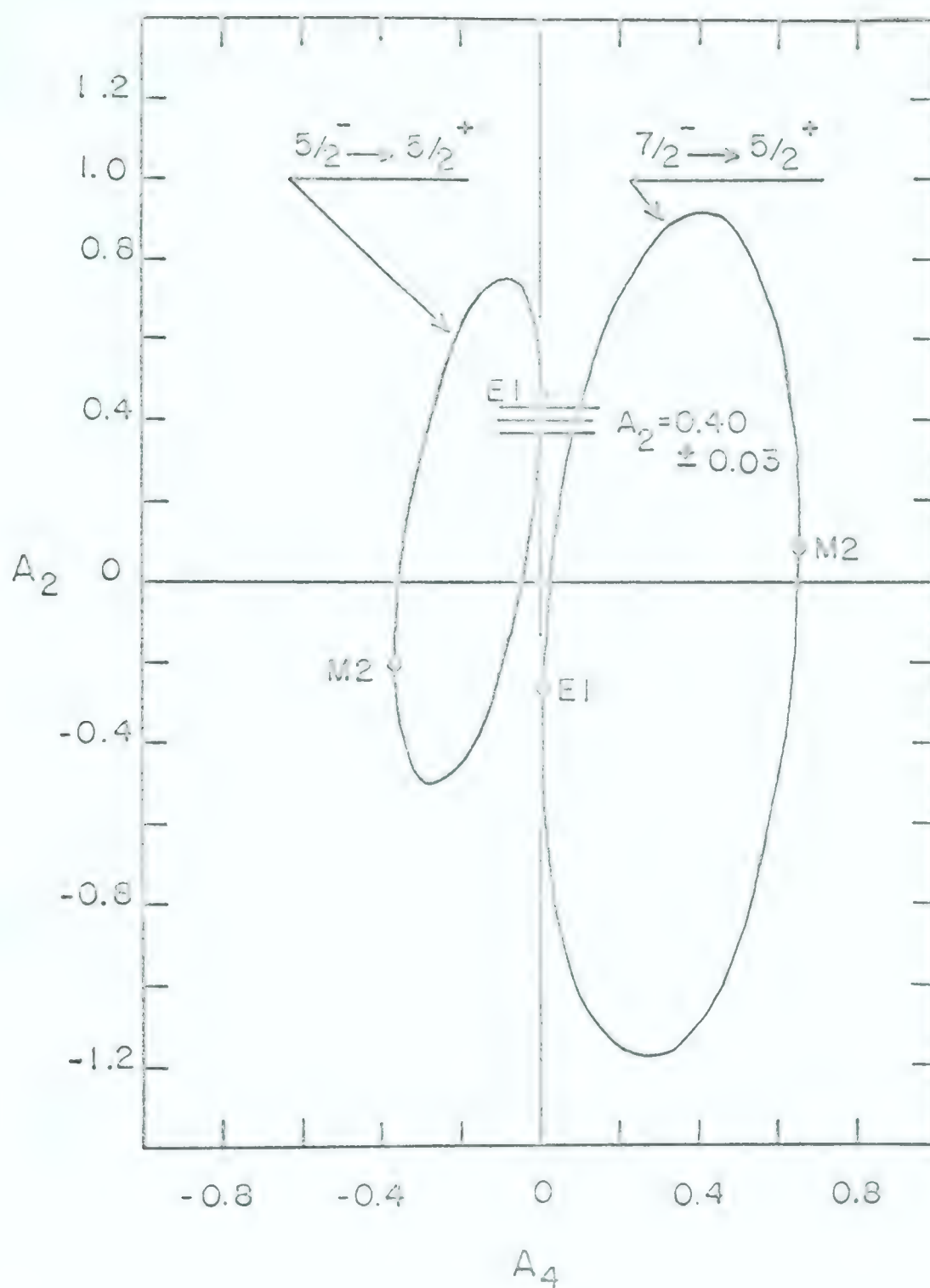
FIGURE 3.7

The Angular Correlation Results for the
3.85-MeV State

Graphs are plotted of A_2 versus A_4 as a function
of δ for the two cases $5/2^- \rightarrow 5/2^+$ and $7/2^- \rightarrow 5/2^+$. The
experimental value of A_2 gives two possible values of
δ. For the $5/2^-$ case, $\delta \simeq +0.05$ and for the $7/2^-$
case, $\delta \simeq -0.40$. The dots show the values of A_2 and
A_4 for the pure-multipole radiation indicated.

Transition	$\lvert M \rvert^2$	
	E1	M2
$5/2^- \to 5/2^+$	$\geqslant 10^{-5}$	$\geqslant 1.5$
$7/2^- \to 5/2^+$	$\geqslant 10^{-3}$	$\geqslant 40$

The E1 and M2 Transition Strengths

TABLE 3.2

The values of $\lvert M \rvert^2$ in Table 3.2 for the E1 part of the transition show typical inhibition factors (Wi60). However, the large $\lvert M \rvert^2$ for the M2 part assuming $J^\pi = 7/2^-$ makes this assignment unlikely, so that $J^\pi = 5/2^-$ is strongly favoured.

The isotropic n-γ correlation for the $3.06 \to 0.87$ transition is consistent with the spin assignment $1/2^-$ for the 3.06-MeV state. The lifetime is also consistent with E1 radiation since $\tau = 1.2 \times 10^{-13}$ yields $\lvert M \rvert^2 \simeq 10^{-3}$ Weisskopf units.

3.5 Discussion

Segel et al (Se63) have recently shown that the 3.86-MeV state in F^{17} (see Fig. 3.8) has $J^\pi = 5/2^-$. The angular distribution of 3.86-MeV radiation was measured for the $O^{16}(p, \gamma)F^{17}$ reaction as a function of energy. The angular distribution measured on the resonance at $E_p = 3.473$ MeV gave $A_2 = +0.47 \pm 0.03$. From an analysis of the yield curve, they obtained a radiative lifetime of
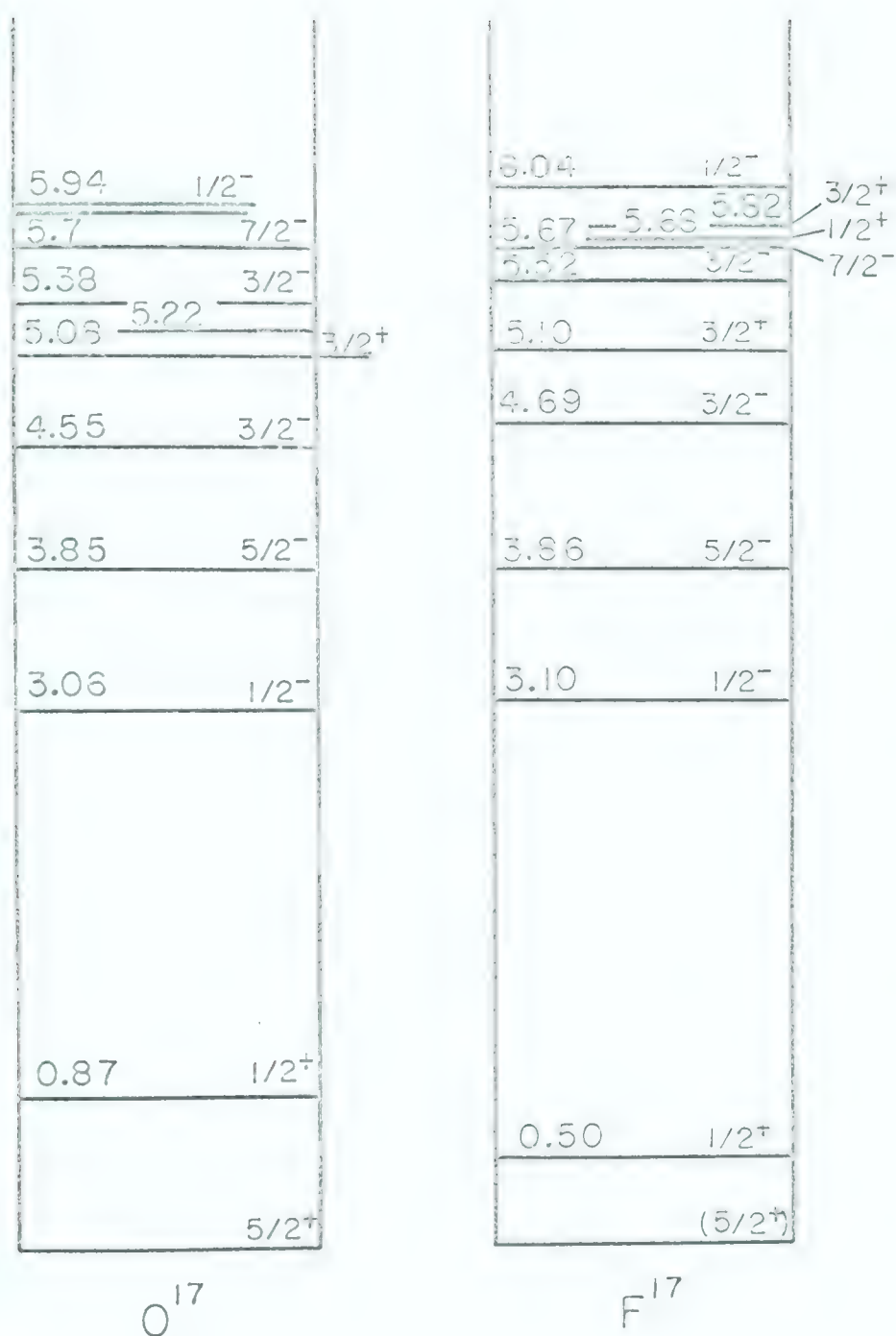
FIGURE 3.8

The Energy Level Diagrams of the Mass 17
Mirror Nuclei

$(0.6\pm0.1) \times 10^{-14}$ sec. In O^{17}, the lifetime is $\leq 2.5 \times 10^{-14}$ sec. The smaller $A_2 = 0.40\pm0.03$ coefficient for the $n-\gamma$ correlation indicates a small amount of M2 radiation, whereas the data in the F^{17} case indicate almost pure E1. However, the measurements agree within the experimental errors.

Measurements on the 3.06-MeV state confirm the assignment $J^{\pi} = 1/2^-$ for this state; the mirror level at 3.10 MeV in F^{17} also has $J^{\pi} = 1/2^-$.

In a recent paper, Yagi et al (Ya63) have studied the energy level structure of O^{17} using the $O^{16}(d,p)O^{17}$ reaction with 15 MeV deuterons. Their data on the reduced widths of the first eight levels of O^{17} indicate that the 1f7/2 level may be the $7/2^-$ level at 5.7 MeV. The ratio of the reduced widths for the 3.85-MeV level to that for the 5.7-MeV level is 0.16. Segel et al have discussed the possible location of the lowest f7/2 level in the mass 17 nuclei and suggest that the level at 5.7 MeV now appears to be the single-particle level.

The theoretical interpretation of the $1/2^-$ and $5/2^-$ states studied in this investigation is still uncertain. It seems worthwhile, at this point, to mention some recent theoretical studies of O^{17} concerned with the negative-parity states.

Calculations on the negative parity states of O^{17} by Harvey (Ha63) predict the lowest level to be in the region of 6 MeV (Fig. 3.8), and do not explain the levels at 3.06 and 3.85 MeV. The calculations are based on the shell model as formulated by Elliott and Harvey and Elliott. The lowest negative-parity

states are assumed to be single excitation states resulting from the excitation of a 1p-particle from the O^{16} core into the (1d,2s)-shell. Harvey's calculations give good account of the levels in neighbouring nuclei F^{19} and O^{18}, although more experimental data are needed to test the O^{18} results.

Harvey notes that his calculations on O^{17} do not contradict the assumptions of Christy and Fowler (Ch54) in their interpretation of the negative parity levels. Christy and Fowler suggest that these states may arise from three particles excited from the O^{16} core. In cluster model language, this would correspond to a C^{13} ground state with four particles in the (1d,2s)-shell.

Matthies et al (Ma63) consider O^{17} as four alpha particles and an extra nucleon. The spectrum of levels is calculated in a weak-coupling approximation taking into account the interaction of the extra nucleon with the non-spherical core of four α-particles, which are vibrating in a configuration possessing the symmetry of a tetrahedron. This theoretical calculation predicts both the positive and negative parity states as well as the ground-state quadrupole moment, the magnetic moment and the lifetime of the 0.87-MeV state. It is successful in most of these endeavours. A $1/2^-$ excitation is predicted in the region of 3 MeV, but the $5/2^-$ level is predicted to be at 5.5 MeV.

As mentioned previously, Macfarlane and French (Ma60), with interest in single-particle states, prefer to give only qualitative statements about the negative parity states. They note that the existence of a 1f7/2 single-particle level only 4 MeV above the

1d5/2 ground state in 0^{17} is surprising. This difficulty, of course, has now been removed only to be replaced by another.

CHAPTER 4

THE SOLID-STATE RADIATION DETECTOR AND TIMING ELECTRONICS

Since the design philosophy of electronic equipment is affected by the details of the radiation detector, a brief discussion of the solid-state detector is given in Section 1. In this section the interest will be focused on those properties affecting the choice of technique. Section 3 is a paper dealing with the details of an electronic design and some of the applications of the solid-state detector system to problems of nuclear physics. The final section is devoted to an analysis of the time resolution that has been realized.

4.1 The Solid-State Radiation Detector

The semiconductor detector is a diode with a large junction area. The two main types of detectors are the surface-barrier and the diffused-junction detector, which are different only in the techniques for forming the junction in a high resistivity semiconductor. To be specific, consider a junction formed by making a thin n-type layer on the surface of a crystal of p-type semiconductor. The n-type layer must be made as thin as possible so that charged particles may easily penetrate into the active region of the diode, i.e. the carrier depleted region in the p-type body of the detector. The depletion region of the detector is enlarged by operating the diode in the reverse-biased part of its characteristic current versus voltage curve.

Figure 4.0 shows schematically the features of a typical solid-state radiation detector. In Fig. 4.0(b) the three regions of a detector are shown. The n-type region is a "window" into the detector and is made thin and heavily doped as illustrated by the charge distribution shown in Fig. 4.0(c). The heavy doping of the n-type region causes the depletion region to penetrate deeply into the bulk of the p-type material since, in equilibrium, the net charge must be zero for the whole device. This dipole charge distribution resulting from ionized donor and acceptor levels gives rise to a potential characterized by a parabolic dependence on the distance through the p-type material as illustrated in Fig. 4.0(d). Thus, the field (Fig. 4.0(e)) is a maximum at the junction and falls off linearly as it penetrates into the body of the diode.

The third region of the detector is the undepleted region in the p-type material. For many purposes it is desirable to eliminate this region entirely by applying sufficient voltage to the junction to make the depletion region "punch through" to the back contact. However, careful design of the detector is required to obtain this condition without excessive leakage current.

Static Characteristics of the Solid-State Detector

To obtain an understanding of the detector, consider the junction region in a diode formed with an abrupt transition from the n-type to the p-type material. The features of Fig. 4.0 assume this. The potential in the detector is found by solving Poisson's
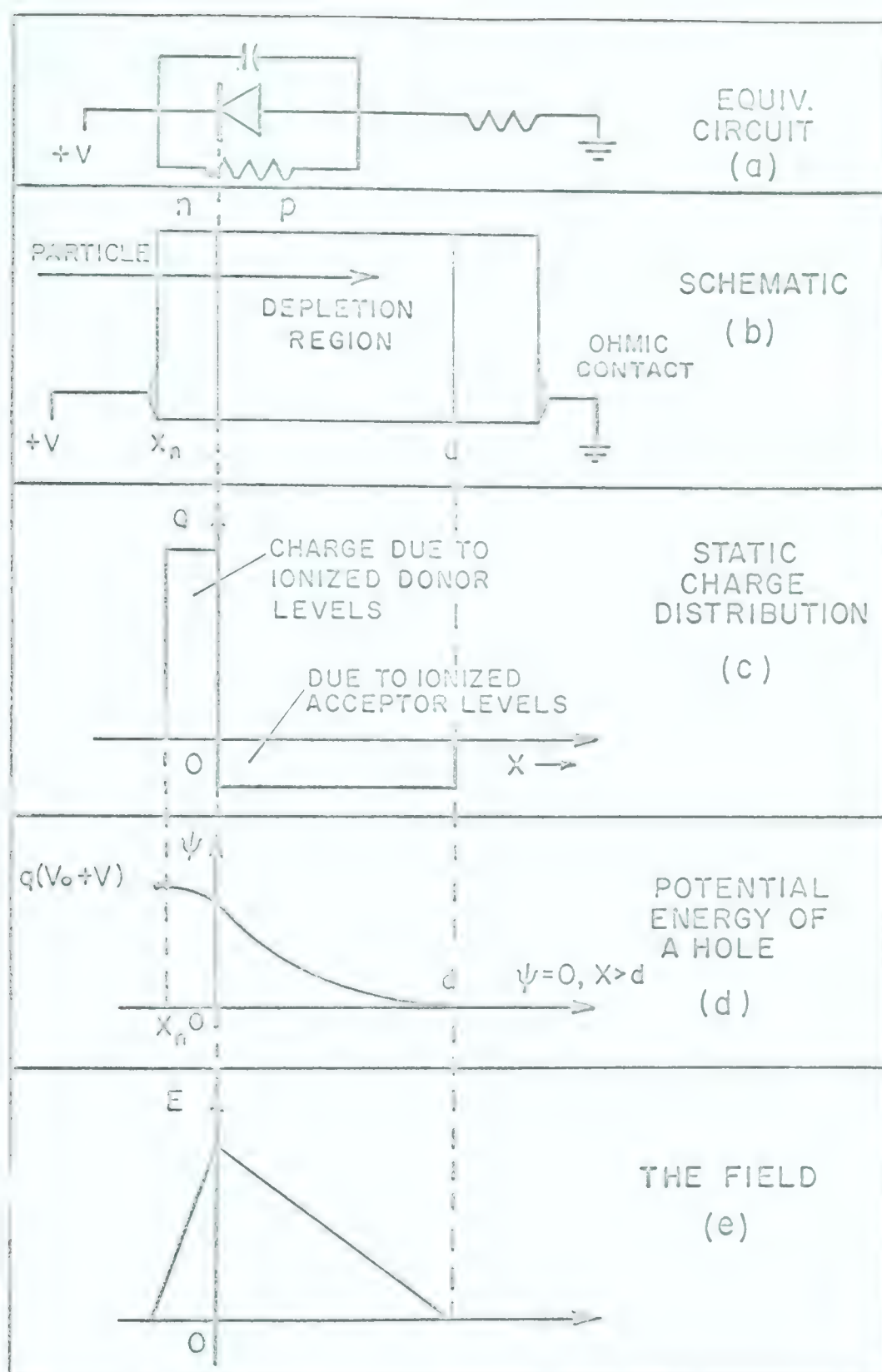
FIGURE 4.0

The Solid-State Particle Detector

(a) An equivalent circuit; the n-region is to the
     left, the p- region to the right.

(b) A schematic diagram of a detector showing its
    three regions.

(c) The equilbrium charge distribution due to
    ionized donor and acceptor levels.

(d) The potential energy of a hole.

(e) The electric field in the carrier depleted region.

equation (Va57), and assuming a one-dimensional model.

$$\frac{d^2 \chi}{d x^2} = - \frac{\rho(x)}{\epsilon \epsilon_o}$$

(4.1)

where:

χ = potential

$\rho(x)$ = charge density

ϵ = dielectric constant

ϵ_o = 8.85 x 10^{-12} F/m

In the n-region, i.e. x < 0

$$\chi_n = V_o + V - \frac{g N_d}{2 \epsilon \epsilon_o} (x_n - x)^2$$

(4.2a)

And in the p-region, x > 0

$$\chi_p = \frac{g N_a}{2 \epsilon \epsilon_o} (d - x)^2$$

(4.2b)

where:

V_o = the thermoelectric potential

V = applied voltage

g = electronic charge

N_d = density of donor atoms

N_a = density of acceptor atoms

d = width of the depletion region in p-region

x_n = width of the depletion region in n-region

The boundary condition at x = 0 requires that

$$\frac{d \chi_n}{d x} = \frac{d \chi_p}{d x} \qquad \text{and} \qquad \chi_n = \chi_p$$

(4.3)

yielding the relation

$$x_n N_d = N_a d$$

(4.4)

and explaining why the n-region should be doped heavily and the

p-region, lightly. The second condition $(X_n = X_p)$ combined with (4.4) gives

$$V_o + V = \frac{q}{2 \epsilon \epsilon_o} N_a d^2 \left(1 + \frac{N_a}{N_d^2} \right) \qquad (4.5)$$

$$\simeq \frac{q}{2 \epsilon \epsilon_o} N_a d^2 \qquad N_d \gg N_a$$

Now the resistivity is given by

$$\rho = \left(N_h q \mu_h + N_e q \mu_e \right)^{-1} \qquad (4.6)$$

where: N_h = density of holes

N_e = density of electrons

μ = the appropriate mobility

and since in the p-type material $N_e \simeq 0$, $N_h \simeq N_a$ we have

$$d^2 = (V_o + V) 2 \epsilon \epsilon_o \mu_h \rho \qquad (4.7)$$

Thus, the depletion-region width is proportional to the square root of the applied voltage, multiplied by the resitivity of the p-type material.

The small-signal capacity of the detector is defined as

$$C = \frac{dQ}{dV} \quad \text{per unit area} \qquad (4.8)$$

From Fig. 4.0 we can see that the stored charge $Q = qN_a d$, so that

$$C = \frac{\epsilon \epsilon_o}{d} \quad \text{per unit area}$$

Before considering the effects of the above considerations on the design of an electronic system, a short discussion of the

transient response of a detector will be given. It will then be useful to consider all the properties of the detector and to make comparisons with other detectors.

Transient Response of S.S. Radiation Detectors

The basic equation governing the motion of charge carriers is the equation of continuity.

$$\frac{\partial n}{\partial t} = -\frac{1}{q} \nabla \cdot \vec{J} - \frac{(n - n_o)}{T} + g \qquad (4.9)$$

where

$\frac{\partial n}{\partial t}$ = number of carriers per cm^3 per sec.

J = current density

n = number of carriers per cm^3

n_o = equilibrium value of n

T = lifetime of the charge carriers

g = externally generated carriers

The current density is given by two terms, one due to drift of charge carriers in the field $\vec{E}$ and the other due to the diffusion of the charge carriers.

$$\vec{J} = nq\mu \vec{E} - qD\nabla n \qquad (4.10)$$

Equations (4.9) and (4.10) must be solved simultaneously. However, one can usually make drastic but realistic approximations to simplify the mathematical calculation. For example, in the depletion region, the current density due to $\vec{E}$ is much larger than the diffusion current density which can thus be neglected. Similarly, the collection time is much smaller than the lifetime so that the term $(n - n_o)/T$, representing carriers disappearing because of recombina-

tion, can be neglected. With these assumptions

$$\frac{\partial n}{\partial t} = -n\mu \nabla \cdot \vec{E} + g \qquad (4.11)$$

The term g and therefore the solution of (4.11) depends on the manner in which the carriers are generated. One simple assumption we can make is that a charged particle enters the detector and instantaneously creates a uniformly ionized column the length of the depletion region. In this case the hole current (due to n_h) and the electron current due to n_e will be equal. From (4.2b)

$$E = \frac{g N_a}{\epsilon \epsilon_v} (d - x) \qquad (4.12)$$

so that

$$\frac{\partial n}{\partial t} = -n\mu \frac{g N_a}{\epsilon \epsilon_o}$$

and since

$$\rho = (N_a g \mu_h)^{-1}$$

for the holes

$$\frac{\partial n_h}{\partial t} = -\frac{n_h}{\rho \epsilon \epsilon_o}$$

and for the electrons

$$\frac{\partial n_e}{\partial t} = -\frac{\mu_e}{\mu_h} \frac{n_e}{\rho \epsilon \epsilon_o}$$

From (4.10), the current is proportional to n so that the time constants of the currents are

$$\tau_h = \rho \epsilon \epsilon_o \qquad (4.13a)$$

$$\tau_e = \frac{\mu_h}{\mu_e} \rho \epsilon \epsilon_o \qquad (4.13b)$$

If Q is the charge released to one type of carrier by the ionizing particle, the current pulse is

$$i = \frac{Q}{2} \left\{ \frac{1}{\tilde{\tau}_h} \, e^{-\frac{t}{\tau_h}} + \frac{1}{\tilde{\tau}_-} \, e^{-\frac{t}{\tau_e}} \right\} \tag{4.14}$$

To illustrate the effect of different assumptions regarding g, consider that the particle is stopped in a distance very short compared to d; then the electron current is zero since they are not required to move in the field, hence

$$i = \frac{Q}{\tau_h} \, e^{-\frac{t}{\tau_h}} \tag{4.15}$$

Expressions similar to equations (4.14) and (4.15) have been derived previously by Cavalleri et al (Ca63).

The above description is a very simplified picture of the collection of the charge released in the detector. The exact shape and therefore the risetime will depend on where the track of electron-hole pairs is located and oriented in the detector (To61). Also, for heavily ionizing particles, the collection time may be altered by self-shielding of the ionization column, i.e. at first, only the outermost carriers feel the field assumed in the above calculation.

If the depletion region does not reach the back contact of the detector, then the series resistance of the bulk material , in conjunction with the transition capacity, (equation 4.8), form a time constant that may mask the time constants considered.

4.2 A Comparison of Detectors

Before the solid-state diode was developed into a useful particle detector, the detection of charged particles was accomplished with scintillation and gas counters. (Photographic emulsions do not give the time of detection and will not be considered here) A comparison of the solid-state detector with the gas and scintillation counter may be useful in pointing out an electronic system to take advantage of those properties that distinguish it from the other detectors. Table 4.1 compares the three detectors for several quantities important to their performance as particle detectors.

	Solid-State Detector (Si)	Gas Counter	Scintillation Detector
ε	3.5 eV/pair	30 eV/ion pair	700 eV/photo-electron
Current Gain	1	~ 10	$\sim 10^6$
Mobility (cm^2/Vs)	$\mu_h = 500$ $\mu_e = 1250$	$\mu \sim 1$ $\mu_e^+ \sim 1000$	
τ(ns), risetime	~ 10	$\sim 10^3$	$\sim 20\text{-}10^3$
Relative Stopping Power	1	$\sim 10^{-3}$	1
Detector Capacity	$C \propto \dfrac{1}{V^{1/2}}$	Constant	Constant

TABLE 4.1

A Comparison of Detectors

Since the solid-state detector has the smallest value of $\mathcal{E}$, it has the best intrinsic energy resolution. In this respect, other solid-state devices using semiconductors with a small energy gap between the valence and conduction bands hold promise for the future. The absolute value of the energy required is of considerable importance since in low-energy nuclear physics, the energies of interest are in the region of one MeV.

Although the scintillation counter has the advantage that the photomultiplier which is required is an excellent high gain amplifier, the output current pulse is not well defined statistically because of the energy required to create the initial photo-electrons. The solid-state detector and, in less extreme, the gas counter produce statistically well defined signals but require amplifiers to bring their signals to a useful amplitude.

The current pulse produced by an ionizing particle entering any one of the detectors in Table 4.1 has not a simple shape. In the previous section, the shape of the current pulse from a solid-state detector was shown to change drastically as a result of the different mobilities of electrons and holes. This property of detectors, characterized by the mobility of the charge carriers in the case of the solid-state and gas counters, finds its counterpart in the scintillation detector as a result of the complicated mechanism of the scintillation process, and its dependence on the stopping power for the ionizing particles. Let it suffice to say that the effect in the scintillation counter

or more

again produces a current pulse which is the sum of two/components

with varying amplitudes and different time constants. In the case of

organic scintillators, the effect has been used to distinguish differ-

ent ionizing particles by pulse-shape analysis.

The solid-state detector has a much faster response than

either the gas counter or the scintillation detector as can be seen

from Table 4.1. The fast response, combined with the small value of $\mathcal{E}$

for the solid-state counter, makes it ideally suited for fast time

coincidence applications.

Some properties of silicon and germanium are listed in Table

4.2. These two semiconductors are both used for particle detectors

and the technology of using Ge and Si has been extensively studied

because of their importance in semiconductor amplifying devices.

Property	Si	Ge
Intrinsic resistivity (ohm-cm)	10^5-10^6	10-100
Carrier lifetime (sec)	10^{-6}-10^{-3}	
μ_h (cm^2/V-sec)	500	1700
μ_e (cm^2/V-sec)	1250	3600
Energy gap (eV)	1.21	0.785
$\mathcal{E}$ (eV/pair)	3.6	~ 2.4
Density (gm/cm^3)	2.4	5.46
Dielectric constant	11.8	16
Melting point (^{o}C)	1444	936
Z	14	32
A	28	72.6

TABLE 4.2

Some Properties of Silicon and Germanium

SECTION 4.3

ELECTRONIC TIMING WITH A
SOLID-STATE DETECTOR *

T.K.ALEXANDER and G.C.NEILSON

Physics Department
University of Alberta
Edmonton, Alberta
Canada

(Paper to be presented at the Edmonton meeting
of the A.P.S., August, 1963.)

ABSTRACT

An amplifier and shaping circuit has been
designed to take advantage of the precise timing
available from solid-state particle detectors[1]. The
system to be described has been used in the following
techniques for nuclear research: (1) Fast particle-
gamma-ray coincidence measurements using a solid-
state detector and a NaI(Tl) scintillation counter.
(2) Neutron time-of-flight analysis by detecting an
associated charged particle for the zero-time reference,
(3) Prompt identification of charged particles by
measuring their energy and velocity simultaneously,
(4) Detecting the time of arrival of a pulsed beam
of particles from the accelerator. This has been done
by collecting the nanosecond burst of charged particles
in a Faraday cup or on the target itself.

[1] T.K. Alexander and G.C. Neilson; Proceedings of
the Conference on Instrument Techniques in Nuclear
Pulse Analysis - Monterey, California, April (1963)
in press.

1. Introduction

A linear amplifier and a shaping circuit has been designed to take advantage of both the precise time and energy resolution available from solid-state detectors.

It is well known that the charge collection time in a diode particle detector is fast provided the ionizing particle is stopped within the depletion region. Also the small energy required to create an electon-hole pair (3.6 ev) together with the fast relaxation time (1,2) of the current pulse tends to produce a signal with small statistical time jitter. One can therefore use double-delay-line shaped pulses and zero-cross-over detection to advantage, for timing of the ionizing event. At the same time the advantages of charge-sensitive pre-amplifier, linearity and high counting rate capability of the delay-line-type amplifier system are realized.

In our laboratory we have another use for a fast, charge-sensitive amplifying system. The d.c. beam of particles from a Van de Graaff accelerator is chopped into nanosecond pulses by a beam-flipping apparatus (3). It is desirable to detect the arrival of the burst of ions at the target for generation of a zero-time signal for time-of-flight work. This can be done by collecting the burst of charged particles in a Faraday cup or on the target itself. For example, a 20 μA peak current pulse of singly charged particles lasting for 1 ns is approximately the same amount

of charge as that produced by a 0.5-Mev particle stopping
in a solid-state detector. Thus identical amplifying
systems are suitable for the detection of the time-of-
arrival in both cases. This laboratory will soon have
a Mobley compression system in operation and the increased
beam intensity will enhance the time resolution obtainable
from this type of detection.

2. The Double-Delay-Line Amplifier

Goulding (4) and Chase (5) have already provided
a good transistor operational amplifier stage and a
technique for delay-line shaping. Fig. 1 shows the double-
delay-line amplifier designed specifically for our purposes.

DOUBLE DELAY LINE AMPLIFIER
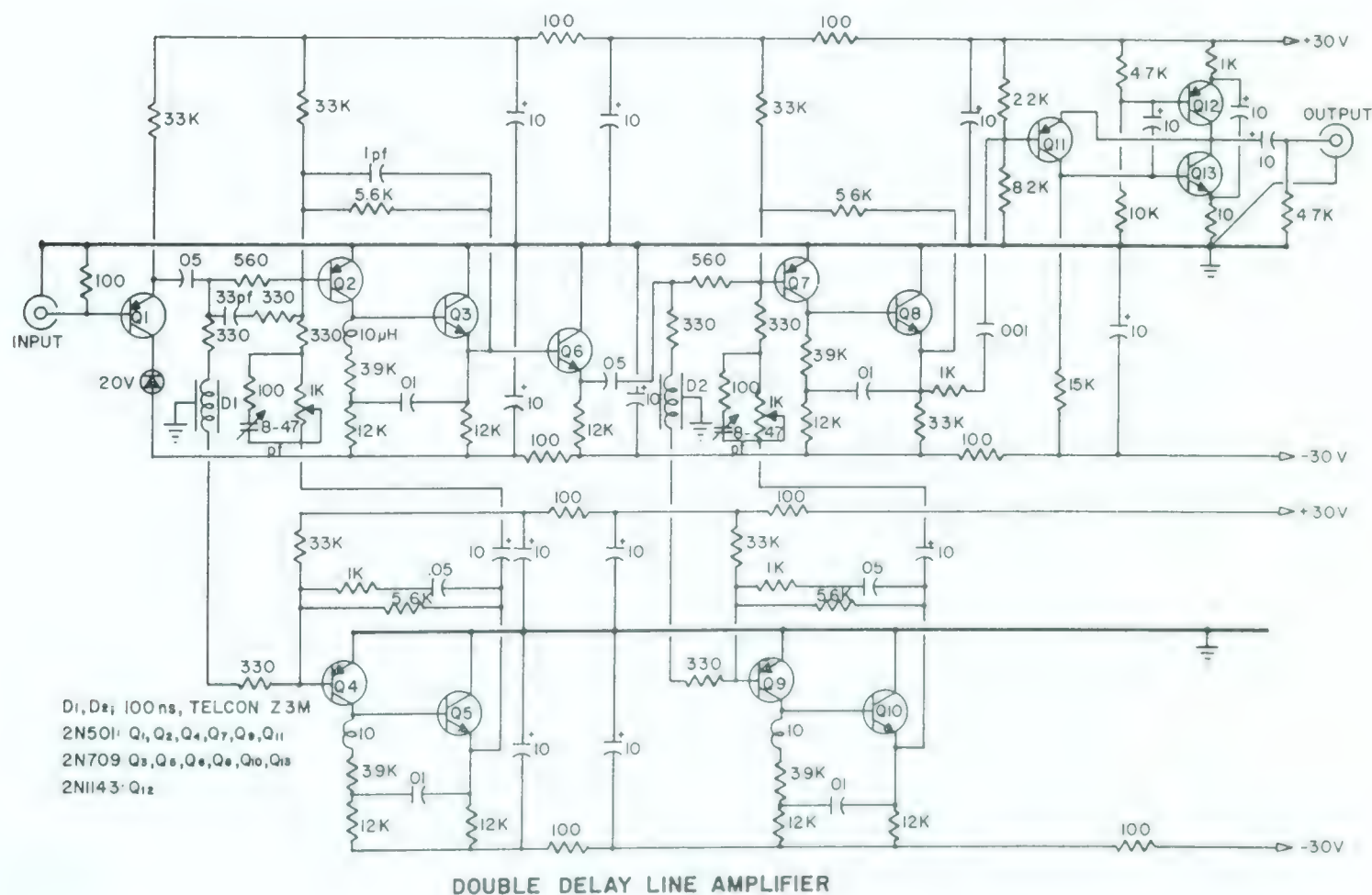
Figure 1

The pulse width is 100 ns (single-ended) enabling the amplifier to handle a steady rate of beam pulses occurring at 1.6 Mc/s. One point worth noting is that the loss in rise-time of the pulse travelling through the delay line and inv rting amplifier (Q4 and Q5) can .... RC network at the input to the amplifying stage (Q2 and Q3). A rise time 25 ns has been obtained by this technique. The delay lines (Telcon Z3M, Z_o = 300 ohms) are bulky compared to the circuit and have been isolated from one another by enclosing them in separately shielded compartments. Other mechanical precautions involve shielding the first amplifying stage from the last and providing a heavy ground lead from the ground point at the emitter of Q13 to the output connector, as indicated in the schematic diagram. Photographs of the output wave forms will be shown in Figures 2 and 4.

Horizontal = 50 ns/cm
Vertical = 2 v/cm
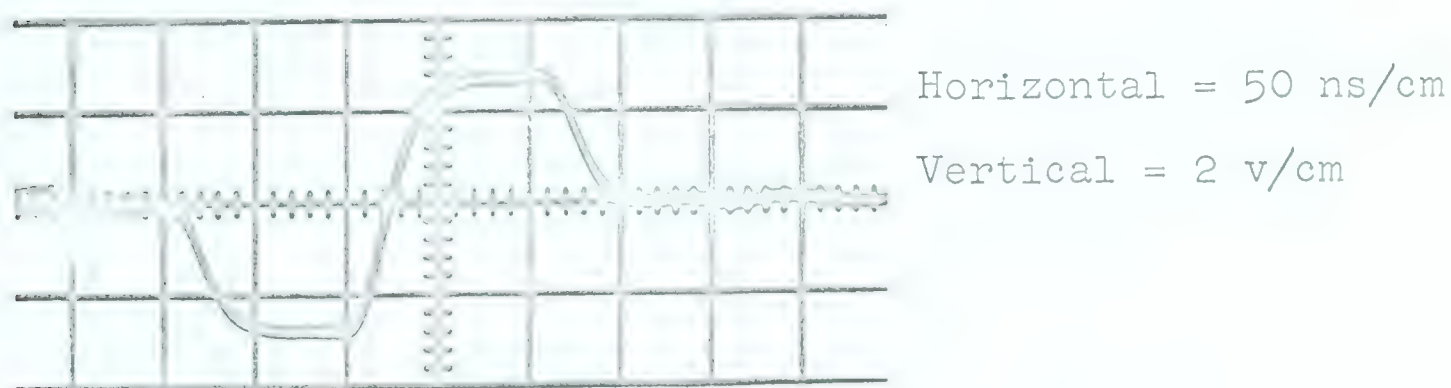
Figure 2

Fig. 2 shows the output waveform of the 100 ns double-delay-line amplifier when a voltage step is applied to the test input of the pre-amplifier. The horizontal

- 4 -

scale is 50 ns/cm and the vertical scale is 2V/cm. The
sensitivity of the system is such that a 5-Mev alpha
particle produces a 2-volt waveform as shown in Fig. 4.

3. The Pre-Amplifier

Fig. 3 shows the pre-amplifier which consists
of a current amplifying stage fed-back with a 3.3pF
integrating capacitor. A low output impedance is provided
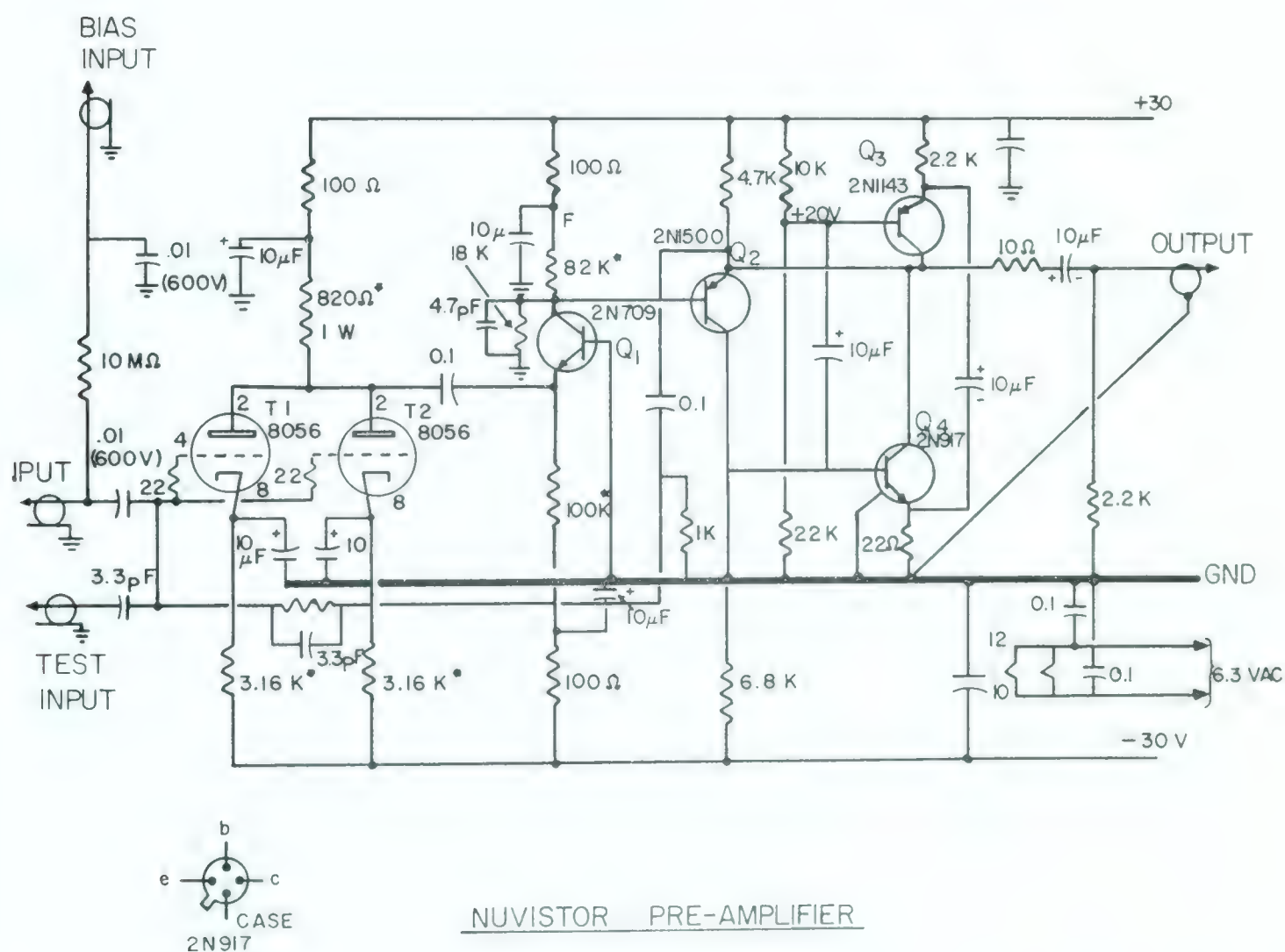by a "White emitter follower" stage. The input amplifying

NUVISTOR   PRE-AMPLIFIER

Figure 3

element is a pair of 8056 nuvistor tubes attempting to
reduce noise due to input capacity(6). With this
pre-amplifier a noise equivalent of 23 kev is obtained

- 5 -

for open circuit conditions and double-delay-line

shaping. For a 300 ohm-cm detector with an area of

1.3 cm^2, the measured resolution is 70 kev at a bias

of 200 volts.
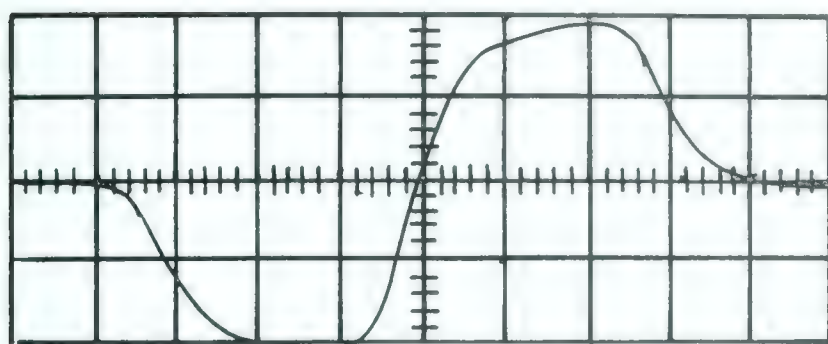
Pu^{239} ALPHA PARTICLE
HORIZONTAL = 40 ns/CM
VERTICAL   = I V/CM
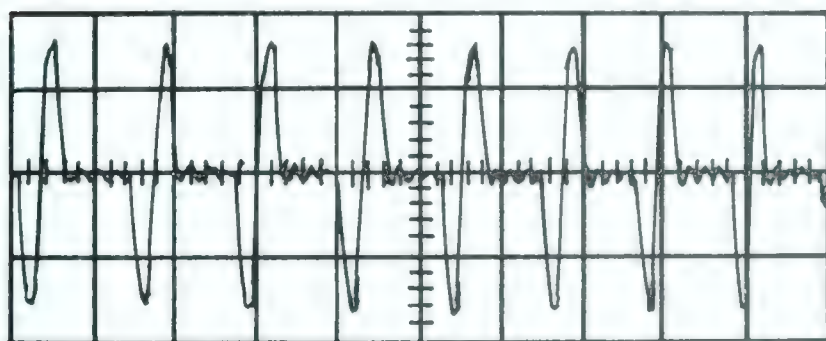
PULSED BEAM
HORIZONTAL = 500 ns/CM
VERTICAL   = 0.2 V/CM

Figure 4

The top picture in Fig. 4 is the output obtained

using the amplifier with a 300 ohm-cm, 1.3 cm^2 area, solid-

state detector. The waveform resulted from a Pu^{239} alpha-

particle being stopped in the detector. The sensitivity

is then approximately $1V/10^{-13}$ coul.

The trace at the bottom of Fig. 4 is the amplified

pulses obtained by collecting the pulsed beam of protons

from the accelerator. The zero-cross-over is detected and

used for the zero-time signal in time-of-flight analysis.

This application of the system has been extremely helpful

- 6 -

since the waveform, whose amplitude is linear with the
amount of charge in each pulse, can be used to monitor
the operation of the beam flipper and ion source.
Adjustments to eliminate alternate pulses can also be made
quickly and with certainty. The rather slow-rising top
on the pulses in the photograph is due to unsuppressed
electron emission from the Faraday cup and can be
eliminated if necessary.

CROSS OVER PICK OFF

Figure 5

The zero detector shown in Fig. 5 $(Q_1$ and $Q_2)$
is a Schmitt trigger circuit similar to the one designed
by Goulding and McNaught [7]. The other trigger circuit,

- 7 -

Q4 and Q5, provides a variable width for the output waveform. The currents switched in Q2 and Q5 are summed on a common resistor (390 ohms), producing a waveform whose front edge is timed from the zero-cross-over circuit but whose backedge is determined by the period of the trigger circuit. Together, their action produces a positive pulse at the base of Q6. This pulse is then clipped by a shorted delay line (2T = 150 ns) and amplified to produce a positive 4-V pulse suitable for operation of a 6BN6 time-to-amplitude converter (8).

Fig. 6 shows the time resolution obtained for alpha particles detected in coincidence with gamma radiation.
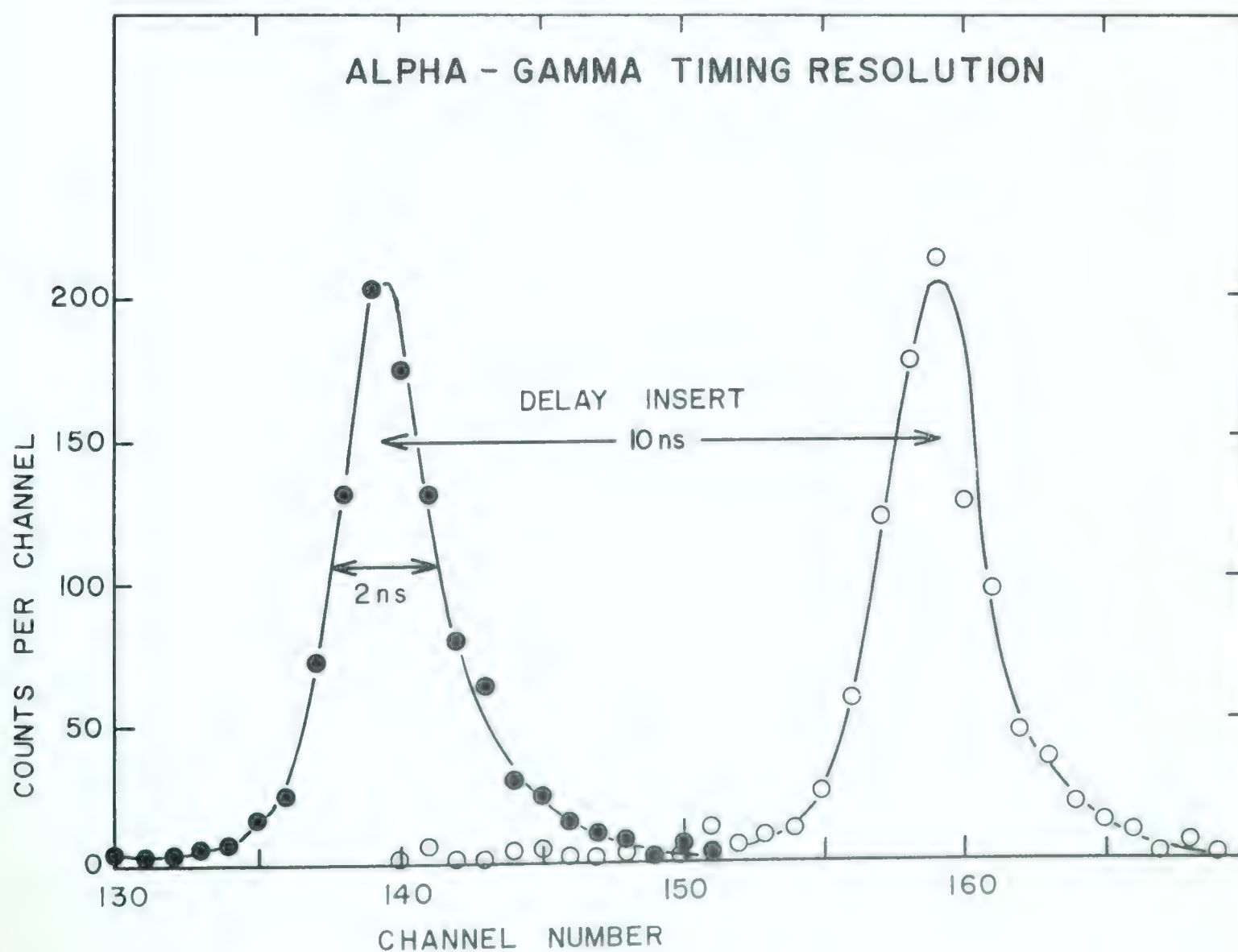
Figure 6

- 8 -

The reaction $F^{19}(p,\alpha,\gamma)O^{16}$ was used to produce 2-Mev alpha particles and 6.13-Mev gamma radiation. The gamma rays were detected in a 4 in. by 4 in. NaI(Tl) crystal mounted on a 58AVP photomultiplier. The solid-state detector was a 300 ohm-cm., 1.3 cm^2 area, surface barrier detector. A side-channel on the gamma-ray detector was biased at an energy of 2.5 Mev and gated the kicksorter analyzing the output of the time-to-amplitude converter. The full width at half maximum is approximately two nanoseconds. The resolution performance will be discussed in a latter section.

Fig. 7 is a schematic diagram of an experimental apparatus to investigate the possibilities of precise timing of charged particles with respect to a pulse of particles from the accelerator. The arrival of a pulse of beam is detected by collecting the charge on the target (T) or on a set of slits just before the target. Charged particles leaving the target at an angle of 135° are stopped in a solid-state detector whose distance from the target can be varied. The output of the time-to-amplitude converter is then a measure of the time-of-flight of a particle from the target to the detector.

The particle's energy (E) and time-of-flight (t) can be obtained simultaneously from the detector and fed to a two-parameter pulse-amplitude analyser. Each type of particle gives a different locus of points depending on the particles' mass, as illustrated in the next figure.
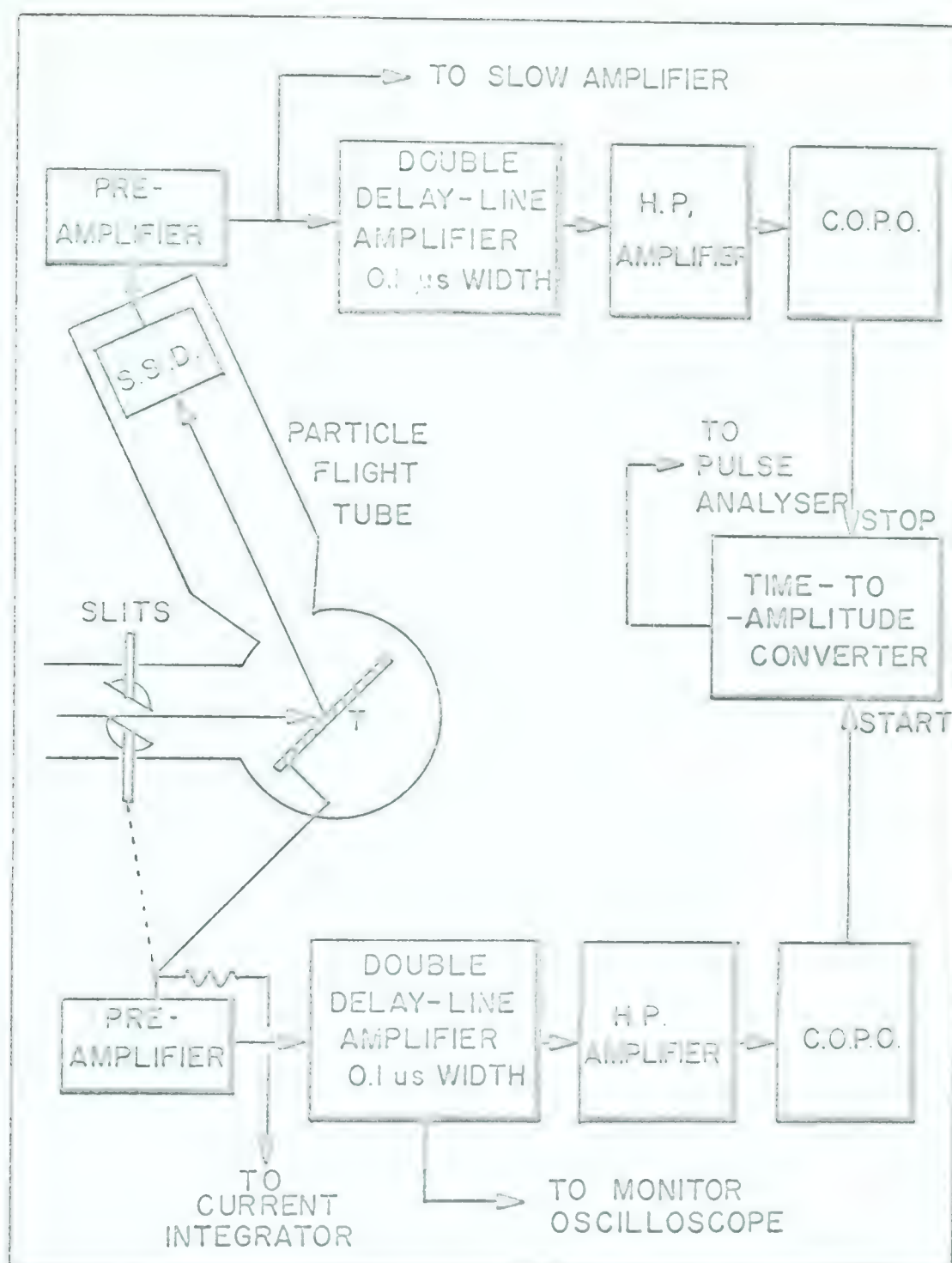
Figure 7

This equipment also allows one to obtain a profile of the beam pulse. If a thin scattering target is used, then the width of the pulsed beam of particles is contained in the measured resolution curve, and can be extracted if the resolution curve of the detecting scheme is known.
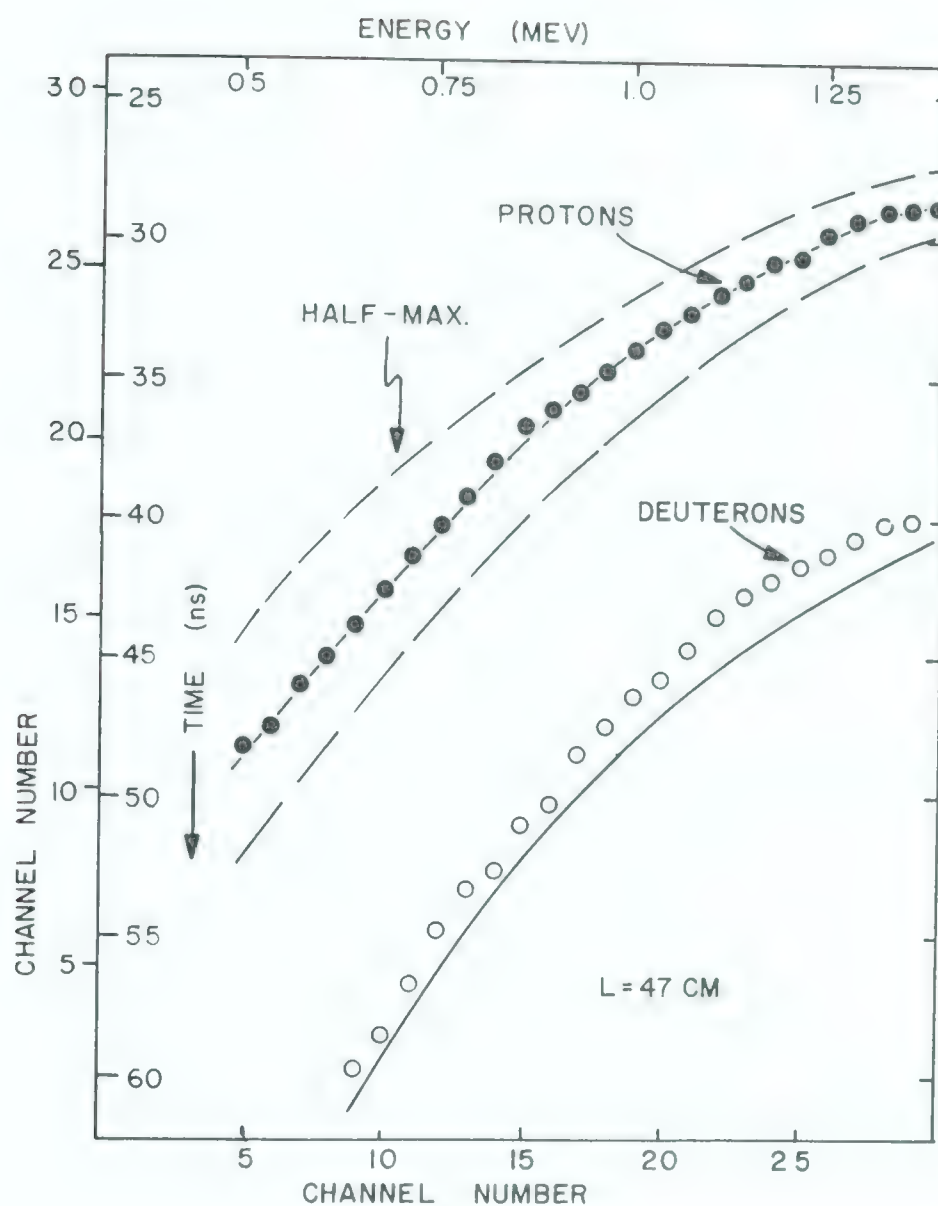
- 10 -

Figure 8

Fig. 8 is a plot of particle energy against particle time-of-flight obtained with the apparatus shown in the previous figure. The data was accumulated in a 32 by 32 channel coincidence analyser. The dots are experimental points while the solid curves are the calculated loci for protons and deuterons. The dashed curves represent the half-maximum points for the

experimental data. These data do not show the best resolution obtained, but illustrate the variation of timing resolution with particle energy, which will be discussed later. The data show clearly that an Ext^2- method of mass identification is feasible even down to low energies.

5. Discussion of Performance

The data on resolution have been presented from a utilitarian point of view, illustrating situations which would be encountered in using the equipment for nuclear investigation. One, however, can look at the performance in more ideal cases.

One can easily show that the resolutions for energy and time are related by (9)

$$\sigma_T = \left(\frac{t}{V}\right)\sigma_n \tag{1}$$

in this system. σ_T^2 is the variance of time, σ_n^2 is the variance of voltage, t is the rising-time constant of the pulse and V is the amplitude of the pulse. With a suitable change of units

$$R_T = \frac{\sqrt{2}}{2.2}\left(\frac{t}{V}\right)R_E \tag{2}$$

where E = energy of particle

R_E = measured energy resolution

T = 10% to 90% rise time

Thus one sees that the criterion for good time resolution is to minimize the product TR_E. We also see that R_T is

- 12 -

proportional to $1/E$ as illustrated in Fig. 8.

If one measures the electronic resolution (i.e. Cin = 0) a value of 0.2 ns is obtained, which can be predicted from measurements of T and R_E which are 25 ns and 23 kev respectively. Similarly, in the case where a 1.3 cm^2 area detector is used the rise-time increases to approximately 40 ns and the noise to 70 kev resulting in a time resolution of approximately 1 ns for 2-Mev particles.

Acknowledgements

- 13 -

References

1) Tove, P.A. and Falk, K. N.I. & M. 12 (1961) 278

2) Frabri, G., Gatti, E., and Svelto, V., Proc. of the
   Conf. on Instrument Techniques in Nuclear Pulse
   Analysis, Monterey, Calif. April (1963) in Press.

3) Neilson, G.C., Dawson, W.K., Johnson, F.A. and
   Sample, J.T., Suffield Tech. Report 176 D.R.B., 1960

4) Goulding, F.S., Nicholson, R.W. and Waugh, J.B.,
   N.I. & M. 8 (1960) 272.

5) Chase, R.L. and Svelto, V., BNL 5350 (1962)

6) Goulding, F.S. and Landis, D.A., Proc. of the Conf.
   on Instrument Techniques in Nuclear Pulse
   Analysis, Monterey, Calif. April (1963) in Press.

7) Goulding, F.S. and McNaught, R.A., N.I. & M. 9 (1960) 282.

8) Neilson, G.C., Dawson, W.K. and Johnson, F.A.,
   R.S.I. 30 (1959) 963.

9) Cottini, C., Gatti, E., and Svelto, V., Proc. of the
   Conf. on Insturment Techniques in Nuclear Pulse
   Analysis, Monterey, Calif. April (1963) in Press.

4.4 The Time Resolution of the Solid-State Detector System

In this section the time resolution of the solid-state detector system described in Section 3 is discussed. The time resolution achievable in practice often depends on the details and compromises of the particular experiment. Therefore the discussion will be restricted to the components of time jitter introduced by the solid-state detector system alone. No consideration will be given to the jitter introduced in the measurement of a time interval by the reference (t = o) signal, or to effects such as the time spread which may be present in the particles entering the detector.

The time resolution for the solid-state detector system can be estimated from the following tests:

(1) Particle-gamma-ray coincidence studies

(2) Resolution measurements with a light pulser.

(3) Resolution tests with an electronic pulse generator.

The first method is the most difficult way to perform the evaluation, since the time resolution of the gamma-ray detector must be known. The energy dependence of the time resolution of the particle detector would also be difficult to measure over a large range of energy.

The light-pulser method can be used successfully since most diode detectors are light sensitive. It is probably the best way to perform the tests provided a stable light-pulse generator is available.

The third method can give nearly all the information

required, if the electronic pulse generator is used to produce

current pulses that simulate the current released from the detector.

In this test, the charge released by the solid-state detector is

simulated by applying a voltage V to a small capacitor C (=3.3 pF)

connected to the input of the system. The applied voltage-step

waveform injects a charge Q = CV into the input circuit in a time

short compared with the response of the amplifier. Therefore, the

actual shape of the current pulse as given by equation (4.14) is

not simulated but idealized to a delta function. The time resolu-

tion, $R(\tau)$, is then measured as a function of Q, which can be

expressed in equivalent particle energy by

$$E = \frac{\mathcal{E} Q}{1.6} \cdot 10^{13} \qquad\qquad (4.16)$$

where:

E = energy in units of MeV

Q = the charge in units of Coulombs

$\mathcal{E}$ = 3.6 eV/electron-hole pair

The third method is the test adopted to evaluate the time

resolution of the system. Figure 4.9 shows the equipment for the

test and the components that are expected to influence the time

resolution of the system, e.g. the detector and the stray capacity

of the input.

From the discussion in Sections 1 and 2, it can be seen

that the current pulse from the detector is well defined because

of the large number of charge carriers produced initially. Since

the time constants of the detector are short ($\sim$ 10 ns), the pulse

is well defined in time as well. However, the noise of the
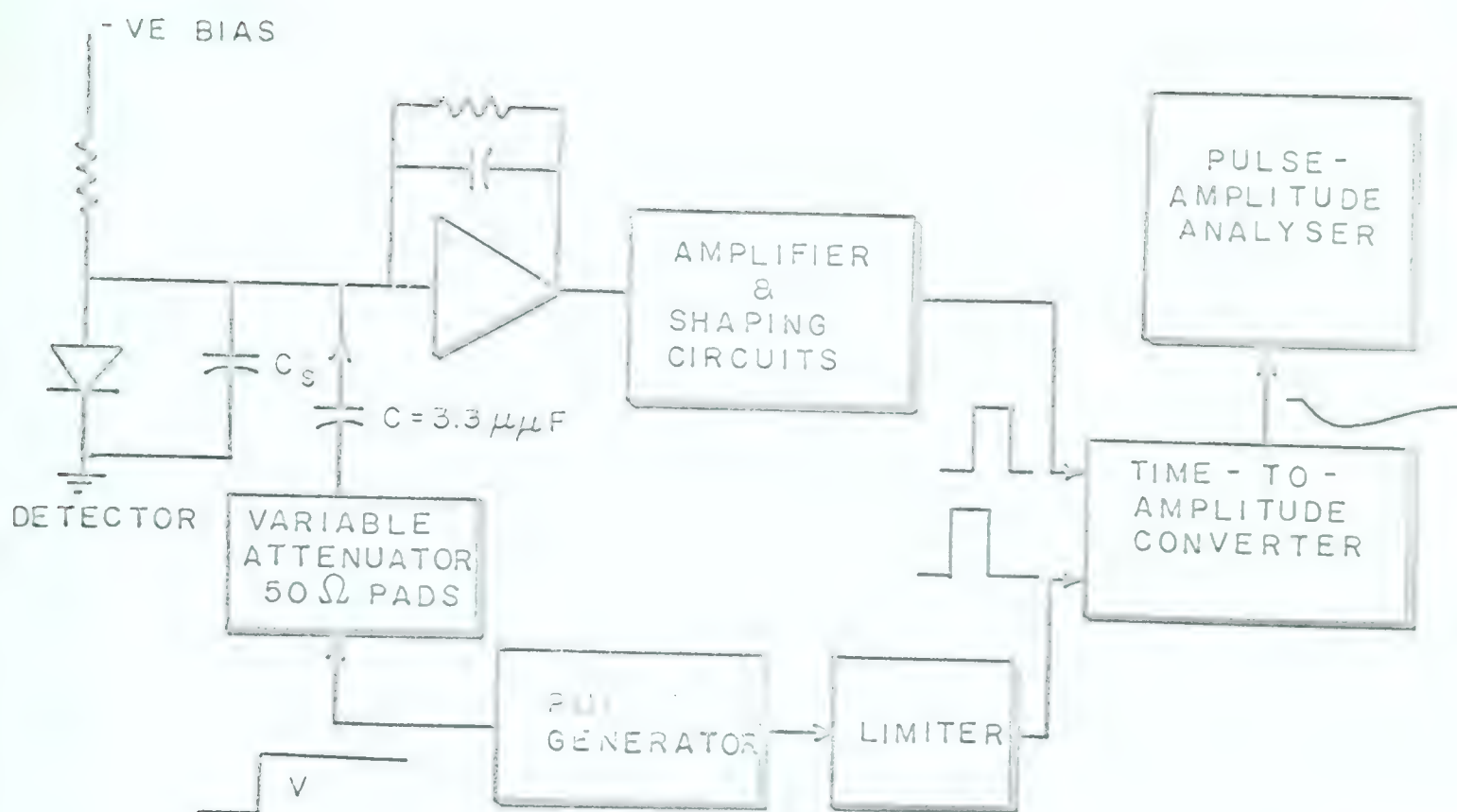
FIGURE 4.9

The Equipment used for the Time-Resolution Test

The pulse generator injects a narrow current pulse
into the input of the solid-state detector timing
system. The time relation between the direct pulse
from the generator and the pulse processed by the
system is measured by the time-to-amplitude converter
and recorded in a 256-channel pulse-amplitude analyser.

detector and the amplifier, and the frequency response of the amplifier will tend to destroy the good definition of the pulse released from the detector.

If the noise in the system is the major cause of the timing jitter, then the resolution will be proportional to E^{-1} through the relation (Co63)

$$\sigma^2(t) = \left(\frac{dV}{dt}\right)^{-2} \sigma^2(V) \tag{4.17}$$

where

$\sigma^2(t)$ = variance of time

$\sigma^2(V)$ = variance of V, i.e. the noise

$\frac{dV}{dt}$ = the slope of the voltage pulse at the threshold of the time detector; V is proportional to E

As described in Section 3, the current pulse at the input is integrated in a charge-sensitive preamplifier. The output of the preamplifier is then differentiated twice to produce a balanced waveform. Since the threshold of the zero cross-over pick-off circuit is approximately that point on the waveform when it passes through zero, dV/dt is easily expressed in terms of the rise time of the pulse and the energy of the particle.

The amplifier was described for the case in which two delay lines are used to produce proper shaping of the pulse. One resistor-capacitor differentiating network followed by shaping with one delay line has also been used, and both cases are considered below.

Double-delay-line Differentiated Pulse

The falling edge of a double-delay-line-shaped pulse can be represented by

$$V(t) = V_o \left(2 e^{-t/\tau} - 1 \right) \qquad (4.18)$$

where: V_o = the peak amplitude of the pulse; $V_o \propto E$.

τ = the rising time-constant of the pulse.

The time at which the waveform begins to fall due to the differentiating action of the delay lines is taken as zero time. This waveform crosses zero volts when $2\exp(-t_1/\tau) = 1$, and has a slope

$$\left. \frac{dV}{dt} \right)_{t_1} = - \frac{V_o}{\tau} \qquad (4.19)$$

One Delay-line Differentiation, T_w, followed by RC - Differentiation with RC = T_w.

For this type of filter the shape of the output pulse is

$$V(t) = \frac{V_o T_w}{T_w - \tau} \left\{ e^{-t/\tau} \left(e^{-T_w/\tau} - 1 \right) - e^{-t/T_w} \left(e^{-1} - 1 \right) \right\} \qquad (4.20)$$

where: T_w = the width of the pulse shaped by the delay line;

also RC = T_w.

The pulse crosses zero at time

$$t_1 = \frac{\tau T_w}{T_w - \tau} \ln \left(\frac{1 - e^{-T_w/\tau}}{1 - e^{-1}} \right) \qquad , \quad T_w > \tau$$

and has the slope

$$\frac{dV}{dt}\Big)_{t_1} = \frac{V_0}{\tau} \frac{\left(1 - e^{-1}\right)^{\frac{\tau}{T_w - \tau}}}{\left(1 - e^{-T_w/\tau}\right)^{\frac{\tau}{T_w - \tau}}}$$

For $T_w \gg \tau$

$$\frac{dV}{dt}\Big)_{t_1} = 0.63 \frac{V_0}{\tau}$$

The factor 0.63 results since RC was chosen to be equal to T_w. The slope can be made to approach V_0/τ by making RC smaller, but then the slope is more dependent on τ.

The type of shaping also affects $\sigma^2(V)$, as is seen from the following simplified argument. The operation of delay line clipping increases the noise by a factor of $\sqrt{2}$ since the high-frequency components in one interval of time are added to the noise in an adjacent interval. In the RC-differentiation case, this does not occur even though the bandwidth is reduced. Thus a factor of approximately $\sqrt{2}$ improvement in the noise is expected in the RC case.

In any type of shaping that involves two differentiations, the time at which the waveform passes through zero is independent of the amplitude of the pulse as illustrated by the expressions for t_1 above. As expressed previously, the jitter in the time is caused by the noise in the system. A component of the time resolution independent of E is also present due to the fluctuations in the electronic time detecting circuit.

To separate the two effects the measured values of $R(t)$ have been squared and plotted against E^{-2} as shown in Fig. 4.10. If the measurement is performed with the solid-state detector removed from the circuit, curve B is obtained. With the detector in place and biased to -150 V, curve A results. Both curves can be represented by

$$R^2(t) = k_1{}^2 + k_2{}^2/Q^2$$

: curve A, $k_1{}^2 = 5$ and $k_2{}^2 = 76$; for curve B, $k_1{}^2 = 4$ and $k_2{}^2 = 31$ in units of (channels)^2/(equivalent MeV)^2. The calibration is 1 ns = 12 channels, so that the resolution can be broken into the following parts

    (1) $R(t)$jitter   = 0.18 ns

    (2) $R(t)$input circuit = $0.46\ E^{-1}$ ns

    (3) $R(t)$detector   = $0.56\ E^{-1}$ ns

The detector tested in this measurement was a Nuclear Diodes 300 ohm-cm surface-barrier detector with a junction area of approximately 0.33 cm^2. The entire arrangement was identical to that used for the $O^{16}(d,p)O^{17}$ and $B^{11}(d,p)B^{12}$ coincidence studies.

The contribution to the resolution caused by the input circuit is probably due to the stray capacity of the detector's socket and the input leads to the pre-amplifier. The detector's contribution includes its total effect, e.g. the junction capacity and the noise generated by the leakage current of the reverse-biased diode.

To estimate the effect of the input capacity on the resolution, the detector was removed from the circuit and replaced by
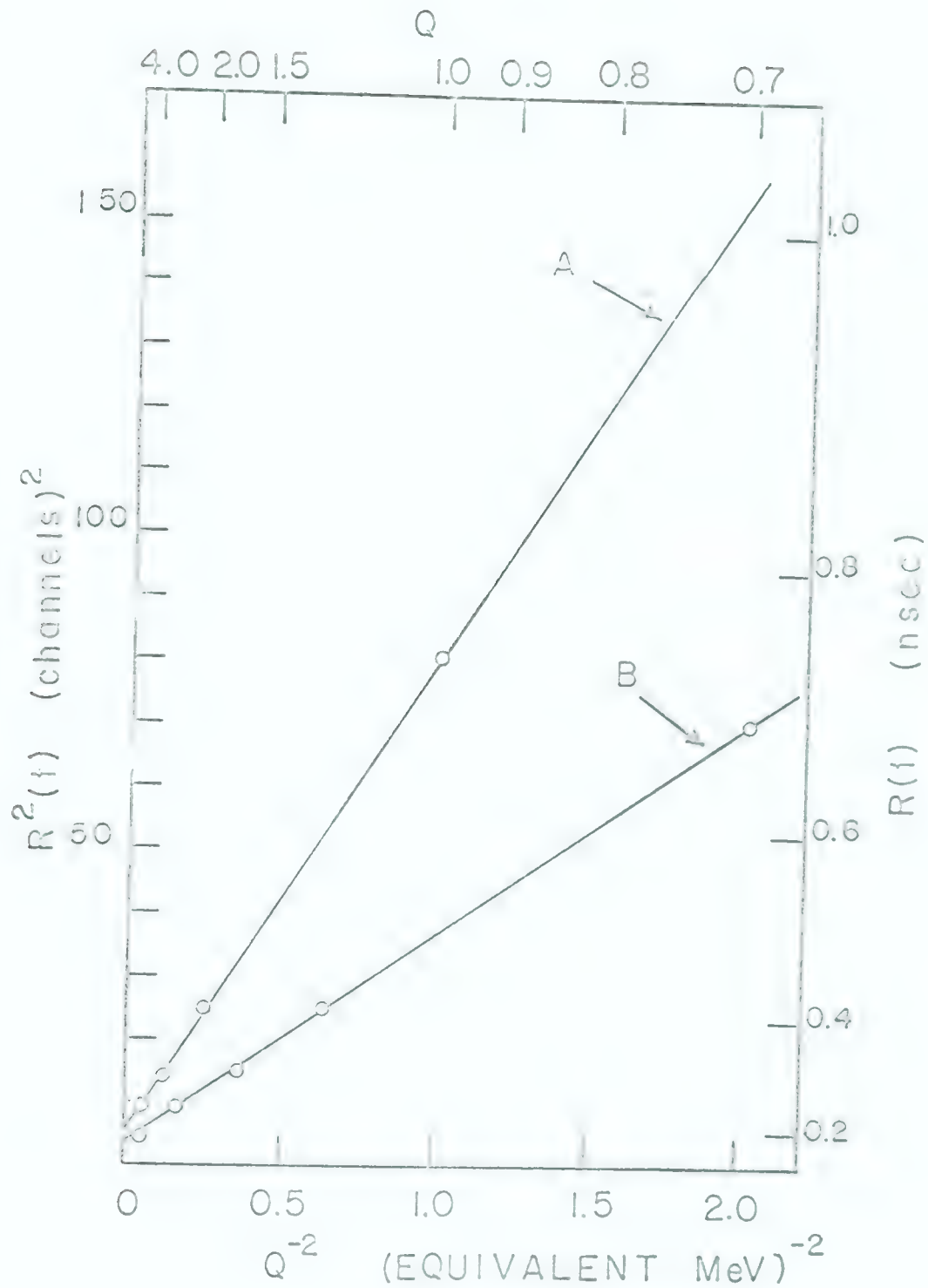
FIGURE 4.10

The Time Resolution as a Function of Input Charge

Curve A was obtained by injecting a narrow pulse of current into the particle detector. Q is the input charge expressed in equivalent MeV. Curve B shows the effect of removing the detector and repeating the test.

capacitors of known value.

The results of this measurement are shown in Table 4.3, where the resolution is listed as a function of the input capacity. The value of the capacity includes the capacity of the holder for the test capacitors; each test capacitor value was measured on a bridge operating at a frequency of 1 kc/s. The input charge simulated E = 2 MeV and was kept constant throughout the test.

The effect of the input capacity on the resolution is quite pronounced and arises from two effects

(1) Since the input impedance of the preamplifier is not negligible at high frequencies, the total input capacity, C, introduces a time constant equal to $Z_{in}.C$, which slows the rise time of the preamplifier output waveform.

(2) The signal-to-noise ratio will decrease with increasing C.

Thus the form of $R(t,C)$ is not a simple function of C, but at least it should show behaviour with terms proportional to C and to C^2. The object of this type of test is to bring into realization the approximate behaviour, and is not intended to be a detailed study of the transfer properties of the electronic circuit. For example, it is easily seen that the slope of the shaped pulse will change in a complicated manner as indicated by the expression previously given, through the dependence on the rising time-constant, τ, which in turn depends on the input capacity.

A good fit to the data results if a term independent of C is included, i.e.

$$R^2 = K_1^{\ 2} + K_2^{\ 2} + K_3^{\ 2} C^2$$

where: $K_1^{\ 2} = 5$, the jitter from the measurement of R vs E.

$K_2^{\ 2} = 10$

$K_3 = 0.15$ channels/

However, there may be terms proportional to $(C \div C_o)$ and $(C \div C_o)^2$ since a fit can be obtained by using C_o as a parameter. An unreasonably large value of C_o gives the best fit (approx. 60 pF). It is difficult to account for such a large value.

INPUT CAP. ($\mu\mu$F)	RESOLUTION (CH.)
4	4
15	4.7
27	6
48	9.5
60	10.5
69	14.2
107	17.5

TABLE 4.3

Conttini, Gatti and Svelto (Co63) have given an analysis of a solid-state detector timing circuit in which $\sigma^2(t)$ is expressed in terms of the input capacity, noise components and time constants of the amplifier. Their system does not use a charge sensitive preamplifier and is not exactly equivalent to the system described here.

Nevertheless, their analysis does show the strong dependence on input capacity.

The timing performance of their circuits is about the same as our system. As shown previously, the resolution is very dependent on the conditions of measurement, so that a direct comparison is difficult. The following table lists a comparison with the conditions of measurement.

$\sigma(t)$ (ns)	Detector Area (mm²)	ρ (Ω-cm)	Test	Input Energy	
0.1	12	110	Light pulser & α-particles	5 MeV	Conttini et al
0.2* ~.3	33	300-1000**	Charge injection	5 MeV	Present Work

* Curve A of Fig. 4.10
** Manufacturer's specification

TABLE 4.4

The charge injection test used to estimate the resolution, does not take into account the presence of series resistance in the detector. Thus the comparison assumes that in our detector this effect is negligible.

CHAPTER 5

EXPERIMENTAL TECHNIQUES

The experimental methods and the analysis of data were dealt with briefly in Chapters 2 and 3 to stress the results and not the details of the experiments. In this chapter, the description of the methods used in the measurements is expanded.

The method used to determine the branching ratio of the 1.67-MeV state of B^{12} is an attempt to do multiparameter analysis. This mode of data accumulation has become a powerful tool of nuclear physics in recent years and has led to the concept of "on line" computers for data storage and reduction. It will become apparent that the accuracy of the branching-ratio data would have been better if a full two-parameter analyser had been available for sorting of the pulses from the solid-state detector and the gamma-ray detector. It might be added that the Nuclear Research Centre will have such a machine in the near future.

The Doppler shift attenuation method of measuring nuclear lifetimes is described in this chapter with reference to the work done on the 3.06- and 3.85-MeV states of O^{17}. No original methods of taking or analysing data have been devised by the author; the method has merely been studied and used. However, the solid-state detector system developed may have some significance in the future, with respect to recent developments in solid-state gamma-ray detectors (Li63b).

The last section of this chapter is a demonstration of the technique of lifetime measurement by direct timing using proton-gamma-ray coincidences. The solid-state detector system and a fast scintillator were used for the measurements. As far as it was developed, this technique is not as good as existing systems that use pulsed-beams and fast scintillators. If the experimental conditions were the same as in the reactions studied (i.e. about 2 MeV protons and 0.95 MeV gamma rays), the technique could be used to study lifetimes ≥ 0.5 nanoseconds and yield data suitable for analysis of the slope of the delayed resolution curve. The lower limit for analysis by the evaluation of the moments of the resolution curve is difficult to estimate, since the experimental conditions are very important when the data are analyzed by this method. In this respect, the technique used for the timing of the solid-state detector pulses is not ideal as a result of the dependence of the shape of the detector's current pulse on the range of the particle entering it. Thus, care would have to be taken in comparing the first moments of two p-γ time distributions if the particles had different energies.

5.1 The Measurement and Analysis of the B^{12} Branching Ratio

The determination of the branching ratio of two competing gamma-ray transitions requires a knowledge of the response of the scintillation counter as a function of gamma-ray energy. Since each detector responds in its own particular fashion in a given situation (e.g. differences in resolution and the presence of scattering materials), it is necessary to determine the response experimentally.

Once the detector's behaviour is known, the branching ratio can be calculated from the measured pulse-amplitude distributions obtained from the reaction in question.

In the particular case here, i.e. the measurement of the branching ratio of the gamma-ray decay of the 1.67-MeV state to the 0.95-MeV state, data were obtained in two ways. One measurement consisted of observing gamma-ray pulse-amplitude distributions, while the second method required the observation of particle spectra. In principle, the two modes of observation give the same result, except for the possible errors due to background. For each measurement the background estimation is entirely different, so that if the two branching-ratio determinations are the same, one has confidence that the corrections for the background were performed properly.

The response of the scintillation counter to gamma rays of different energy in the region of interest is shown in Fig. 5.1. The response to a pure 1.63-MeV gamma ray was determined experimentally by observing the 1.63-MeV radiation from the $F^{20} \rightarrow Ne^{20}$ $+\beta + \gamma$ transmutation. The short-lived F^{20} was produced by the $F^{19}(d,p)F^{20}$ reaction. The gamma-ray spectrum was accumulated by counting for short periods with the beam off the target after a short period of bombardment of a CaF_2 target. The half-life of F^{20} is about 12 minutes (Aj59) so this procedure is easily done without automatic interruption of the beam or programmed recording equipment. The 1.28- and 0.662-MeV shapes were obtained from Na^{22} and Cs^{137} sources respectively. Each spectrum was obtained
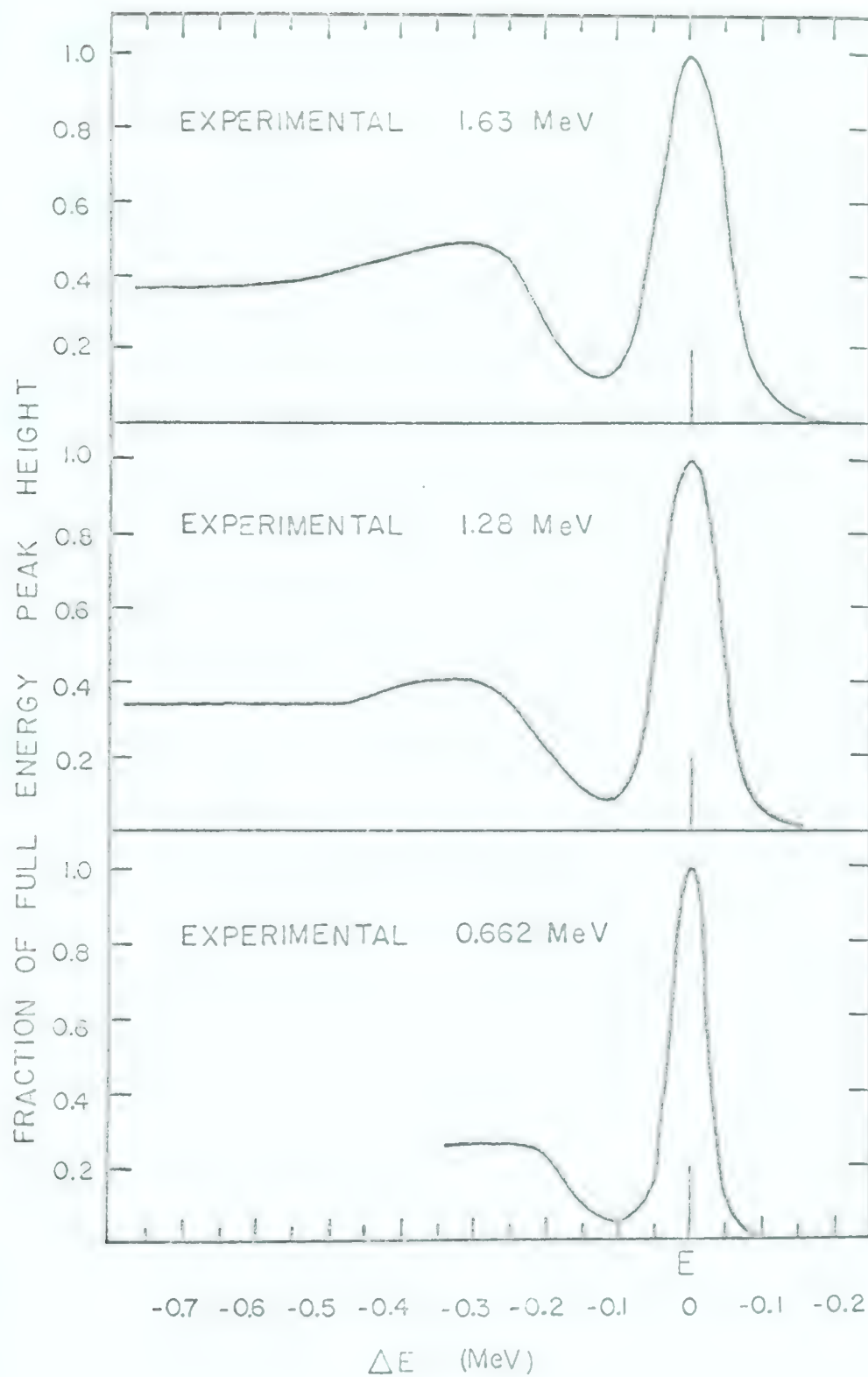
FIGURE 5.1

Experimental Shapes of 1.63-1.28-and
0.662-MeV Gamma-Rays

These spectra were obtained with a 2 in. by 2 in.
NaI(Tl) scintillation detector shielded with 1/4 in.
of lead.

under the conditions in which the B⁺⁺ measurements were made, i.e.
a 1/4-in. lead beta-ray absorber was placed between the source and
the NaI(Tl) crystal.

Figure 5.2 shows the shapes of the 0.95- and 0.72-MeV
gamma rays derived from the data of Fig. 5.1. The 1.67-MeV shape
was taken to be identical to the 1.63-MeV spectrum with the appropri-
ate energy calibration change. All of the curves are plotted with
the full-energy peak normalized to unit peak height. The horizontal
axis of the graphs is $(E-E_\gamma)$.

The spectrum in Fig. 5.3 shows the expected gamma-ray
pulse-amplitude distribution corresponding to a 6% branching to
the 0.95-MeV state from the 1.67-MeV state. This derived spectrum
should be compared with the actual coincidence spectrum obtained
from the $B^{11}(d,p\gamma)B^{12}$ reaction shown in Fig. 2.5. In the actual
spectrum, the intensity in the 1.25 MeV region is slightly higher
than the intensity in the derived spectrum. However, the relative
peak heights for the gamma rays are in fair agreement.

As described in Chapter 2, the other measurement of the
branching ratio was obtained by gating the particle spectrum with
two single-channel analysers selecting two adjacent regions of the
gamma-ray spectrum. The "upper" gate (see Fig. 5.3) selected only
those pulses due to 1.67-MeV gamma rays in the region of 1.25 MeV,
where an excess of counts was observed in the actual coincidence
spectrum of the gamma rays. This would tend to underestimate the
branching ratio if the radiation in the region of 1.25 MeV is in
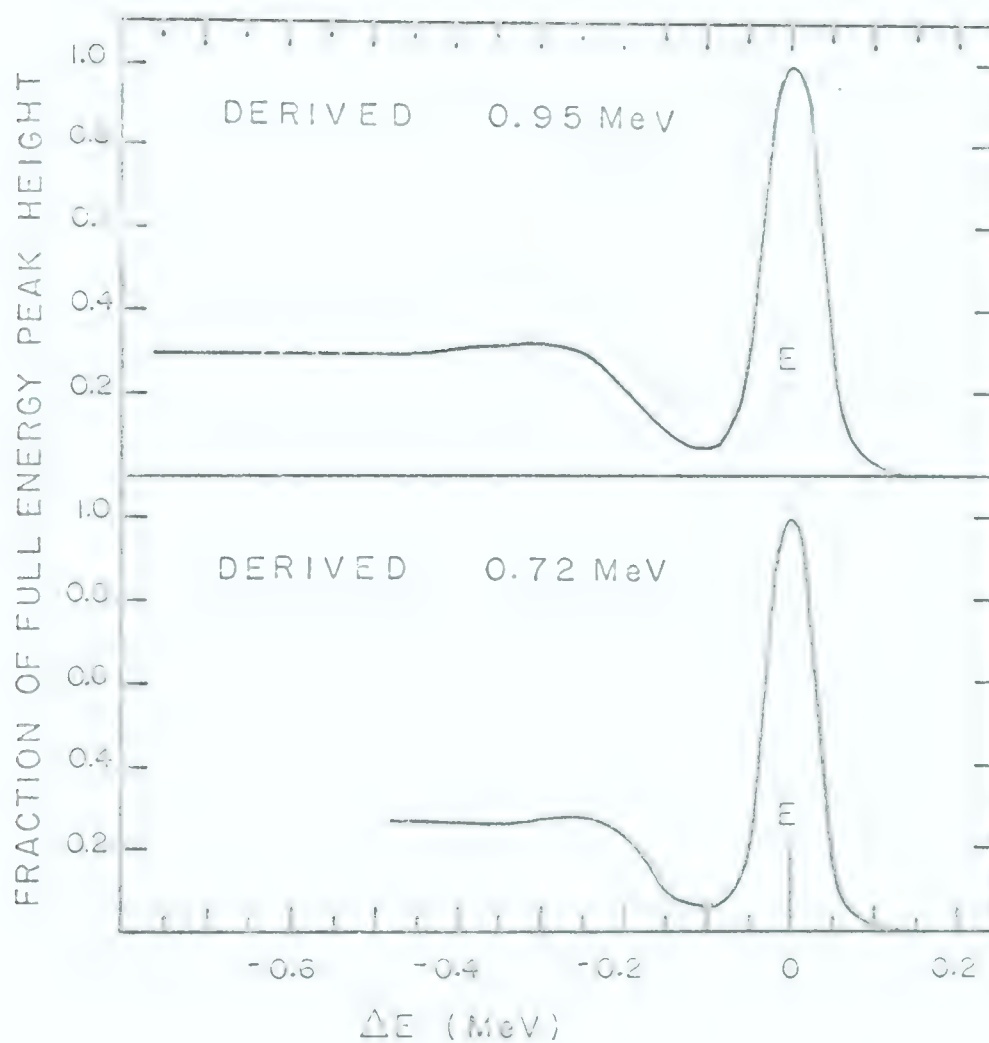coincidence with particles whose energy is the same as the B⁺⁺(1.67)

FIGURE 5.2

The Response for 0.95- and 0.72-MeV
Gamma-Radiation

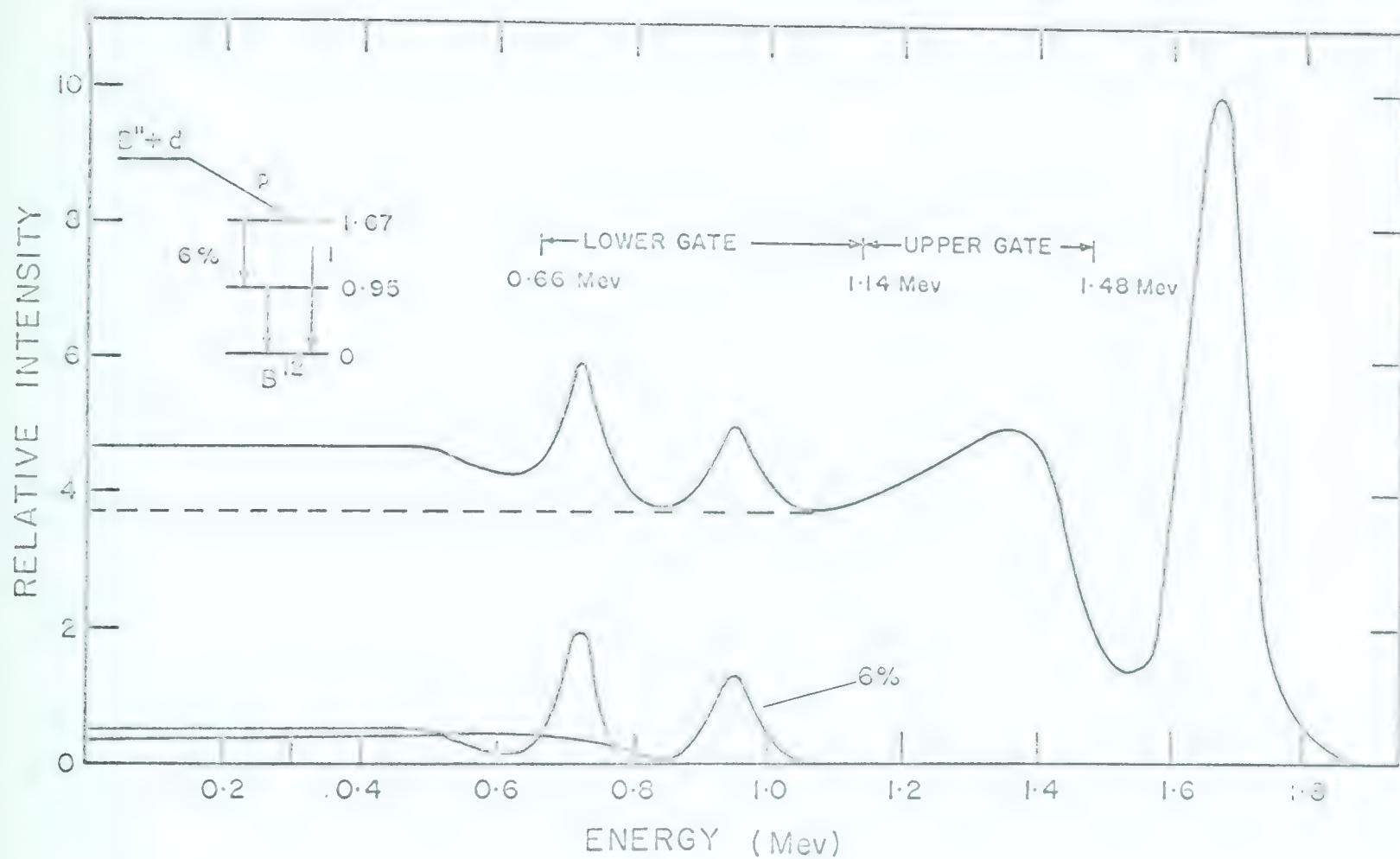These spectra are derived from the shapes given in
Fig. 5.1.

FIGURE 5.3

The Spectrum Shape Derived from Measured
Branching Ratio and Pure Line Shapes

proton group. The "lower" gate included the region of the spectrum containing both the 0.72- and 0.95-MeV full-energy peaks.

The measurement consisted of counting the number of coincident protons leading to the 1.67-MeV state for both the "upper" and "lower" gates.

The branching ratio, X, is calculated from the expression

$$X = \frac{Rf_4(1.67) - f_3(1.67)}{\dfrac{a_1 e_1}{a_3 e_3} f_1(0.72) + \dfrac{a_2 e_2}{a_3 e_3} f_2(0.95)} \tag{5.1}$$

where:

  X = the fraction of the transitions stopping over at the 0.95-MeV state relative to the ground state transition.

  R = the number of counts in the $B^{--}(1.67)$ proton peak gated by the lower gate, divided by the number resulting from the upper gate selection.

  $f_i(E)$ = the fraction of the total counts in the lower gamma-ray gate due to 0.72-, 0.95- and 1.67-MeV gamma rays respectively for i = 1, 2 and 3.

  $f_4(E)$ = the fraction of the total counts in the upper gate due to 1.67-MeV gamma rays.

  a_i = the attenuation factors for the respective gamma rays in the beta-ray absorber.

  e_i = the efficiencies of the NaI(Tl) detector for the gamma rays.

The measured value of R is 1.46 ± 0.06, corresponding to an average over five angles from 15° to 90° of the gamma-ray counter. The f_i values were obtained from the derived response curves of Fig. 5.2 and the 1.63-MeV experimental spectrum. The efficiencies

and absorption coefficients were obtained from published data (Ma60a);
from the above equation, it is noted that only relative values are
required.

Using the values $e_1/e_3 = 1.35$, $e_2/e_3 = 1.21$, $a_1/a_3 = 0.72$
and $a_2/a_3 = 0.84$ together with the experimental values $f_1(0.72) =$
$0.313^{+0.011}_{-0.051}$, $f_2(0.95) = 0.32^{+0.03}_{-0.04}$, $f_3(1.67) = 0.259 \pm 6\%$ and $f_4(1.67) =$
$0.203 \pm 4\%$;

$$x = (0 \pm 1).$$

The shape of the 1.67-MeV gamma ray is most important in
this experiment. The experimental value of the ratio of the full-
energy peak area to the total area is 0.17 and is lower than the
published ratio, 0.21, for a crystal of the same size (Ma60a). This
reflects the presence of the lead absorber for our measurements.
Similar comparisons for the derived 0.95- and 0.72-MeV shapes are
0.27 versus 0.31 and 0.32 versus 0.37 for the derived shapes and
published data respectively.

The following calculation shows that any correction to the
branching ratio due to summing of the 0.72- and 0.95- MeV gamma rays
in the gamma-ray detector is negligible. The addition of the scintil-
lation pulses in time coincidence tends to reduce the measured branch-
ing ratio, and the magnitude of the effect is estimated by

$$F \simeq \frac{2\omega \bar{e}}{4\pi} \left(1 - \frac{\omega \bar{a}}{4\pi} \right)^{-1} \tag{5.2}$$

where:

$F =$ the number of sum events divided by the
number of true 0.95- or 0.72-MeV events.

$$\bar{e} = \ldots$$

ω = the solid angle subtended by the gamma-ray
detector (= 0.15 for L = 10 cm)

For our detector and geometry, $\dfrac{\omega \bar{e}}{4\pi} \simeq 6 \times 10^{-3}$ so that $F \sim 1\%$. This is much less than the experimental errors on the branching ratio and has been neglected.

5.2 The Measurement of the Boron Target Thickness

The thickness of the self-supporting boron target used in the study of the $B^{11}(d,p)B^{12}$ reaction was determined by measuring the apparent shift in the resonance energy of the $F^{19}(p,\alpha'\gamma)O^{16}$ reaction. The measurement was done by observing the relative yield of the 6.13-MeV gamma radiation from a thin target of CaF_2 at the 873-keV resonance.

The curve labelled "A" in Fig. 5.4 shows the yield observed with CaF_2 alone, while the one labelled "B" shows the yield when the thin boron target was placed in front of the CaF_2 target. Both targets were oriented at 45° with respect to the beam direction. Therefore, the observed shift in the resonance represents the actual thickness of the boron as used in the B^{12} studies. The shift in the low-energy edge of the yield curve gives the boron target thickness, while the shift in the high-energy edge gives the combined effect of the thickness of the boron and straggle in the energy of the beam. The straggling caused by the thickness of the target is an important consideration in the fast coincidence work since it introduces an uncertainty in the time of arrival of the particles at the solid-state
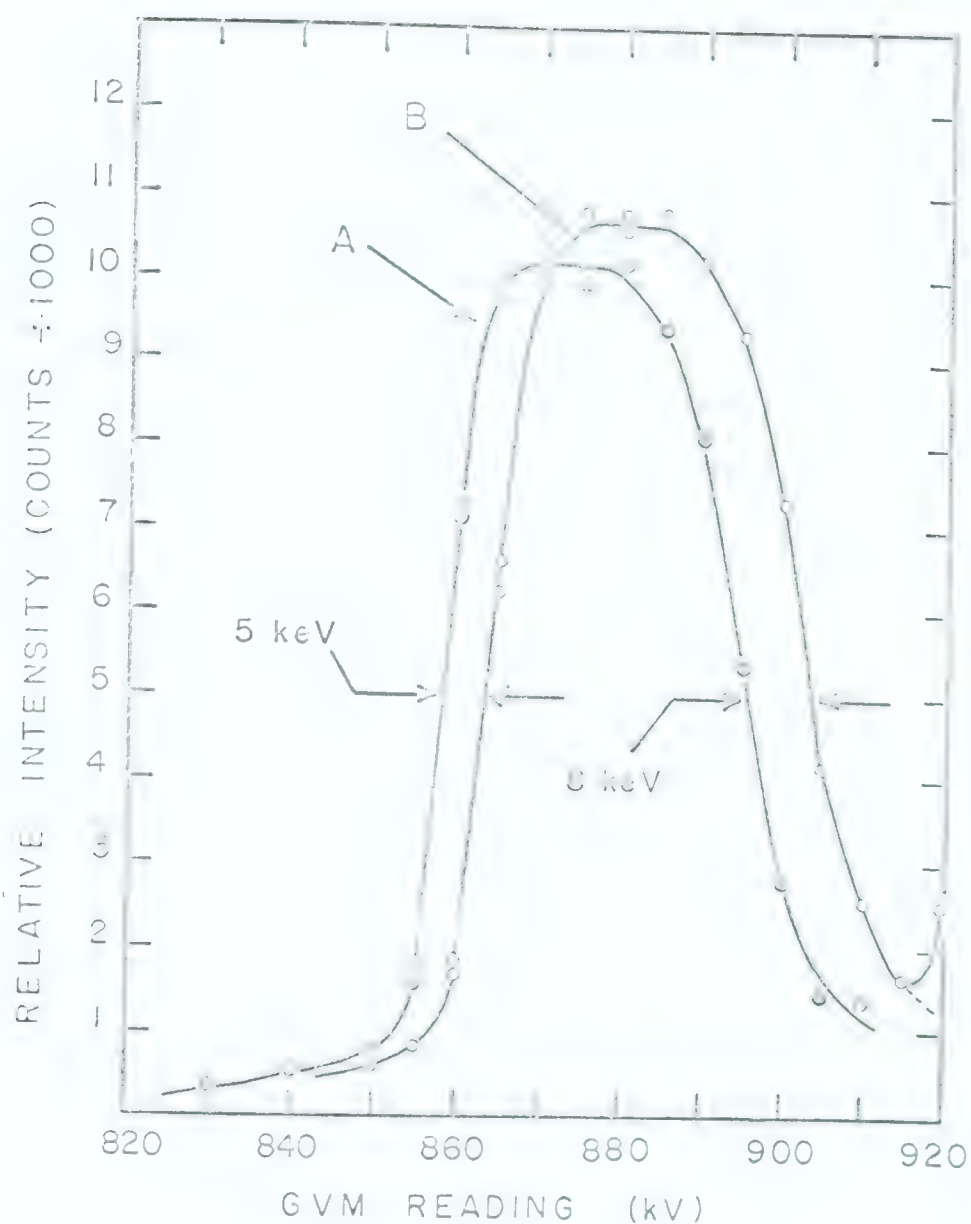
FIGURE 5.4

Measurement of the Thickness of the Boron
Target

The curve A shows the measured yield curve for
the reaction $F^{19}(p, \alpha \gamma)O^{16}$ near the 873 keV resonance.
Curve B shows the apparent shift in the energy of the
resonance when the beam passes through the boron target
before striking the CaF_2 target.

detector. However, for this large the uncertainty is negligible.

The data from this measurement can be summed up by the following values:

(1) The thickness is 5-keV for 873-keV protons, or using the stopping-power data of Whaling (Wh58), $t \approx 10 \ \mu g/cm^2$.

(2) The uncertainty in the energy of the particles leaving the target is 3-keV for 873-keV protons observed in a detector subtending a very small solid angle.

5.3 The Doppler Shift Attenuation Method of Measuring Nuclear Lifetimes

The Doppler shift attenuation method was used to determine the mean lifetimes of the 3.85- and 3.06- MeV levels in O^{17} as described in Chapter 3. This section is intended to present more details of the measurements and to illustrate the technique from the point of view of a tool used in nuclear physics. The method has become increasingly important in recent years because of the increased experimental knowledge accumulated on the stopping power of heavy ions in solids, and because of recent advances in methods of electronic stabilization of the gain of a gamma-ray detector. It has proved to be a powerful method of investigation since nuclear lifetimes are a sensitive test of the theories of nuclear structure. An excellent description of the method can be found in reference (Li63a) on which this description is based.

The technique is founded on the fact that the stopping time of energetic heavy ions in solids is of the same order of

magnitude as the lifetimes of many bound nuclear states. Although

the slowing down mechanism of heavy ions is a difficult process to

describe theoretically, it is fortunate that a "characteristic

stopping time" for a given ion in a given material can be defined.

One can certainly say there is a force acting on the ions

as they pass through a solid,

$$- F = ma \tag{5.3}$$

This force causes them to lose energy as they slow down.

$$\Delta E = \Delta xF \tag{5.4}$$

Thus, $\frac{dv}{dt}$ can be calculated from experimental stopping-power data for
each value of E,

$$-\left(\frac{dE}{dx}\right)_E = m \left(\frac{dv}{dt}\right)_E \tag{5.5}$$

If $\frac{dv}{dt}$ is plotted as a function of the velocity, v, a nearly

linear relation is found as shown in Fig. 5.5. The usual velocity

dependence of $\frac{dE}{dx}$ does not hold for low-energy heavy ions because

of the importance of charge changes. Since $\frac{dv}{dt}$ is a linear function

of v, a characteristic stopping time, α, can be defined through the

statistical statement

$$- m \frac{dv}{dt} = m \frac{v}{\alpha} \tag{5.6}$$

Thus
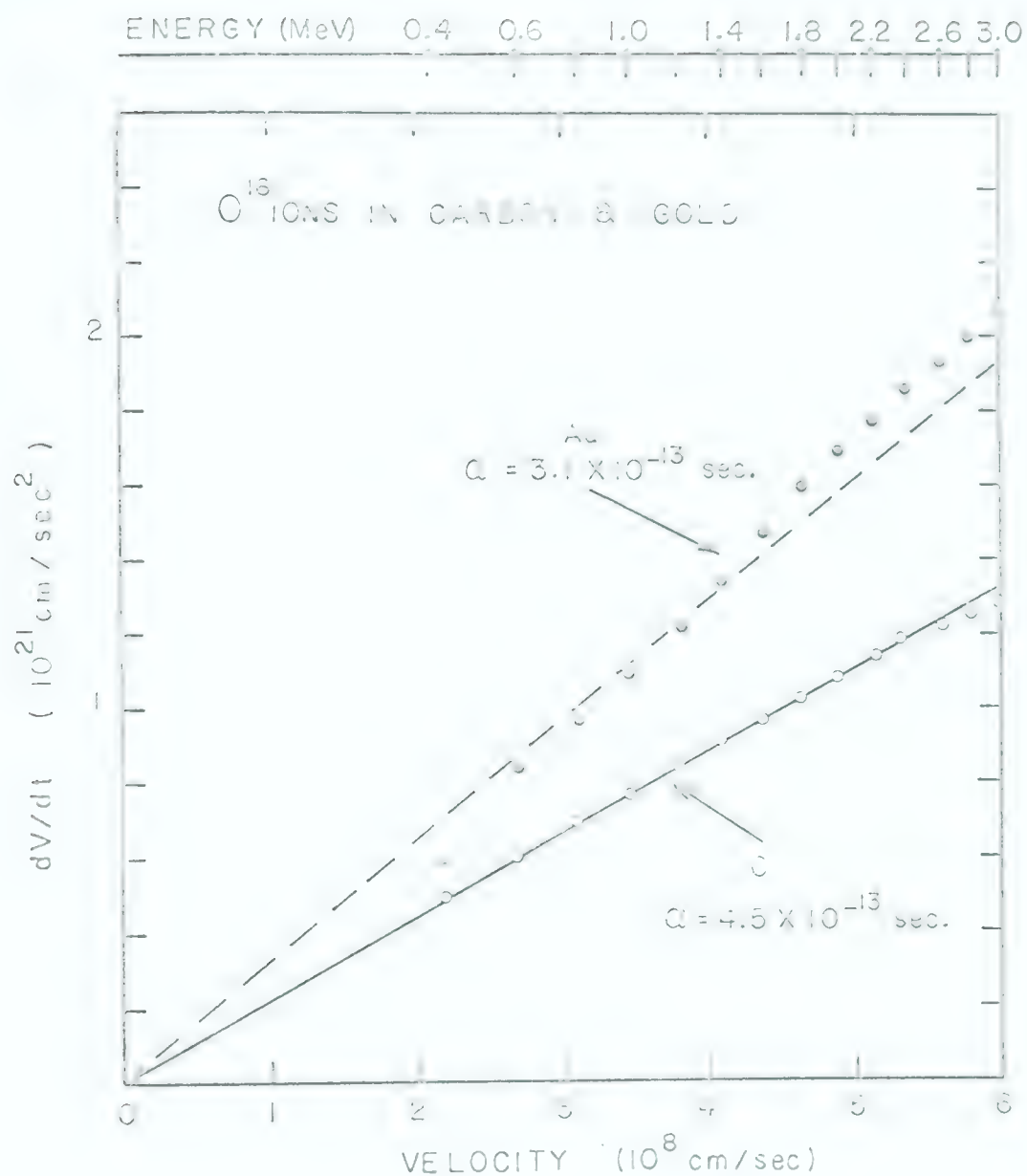
$$v = v_o e^{-t/\alpha} \tag{5.7}$$

FIGURE 5.5

The Deceleration of O^{16} ions in Carbon and
Gold as a Function of Velocity

The curves are calculated from the stopping-
power data of Porat and Ramavataram (Po61).

where v_o = the ion's initial velocity. From Fig. 5.5 the Q's for 0^{16} ions slowing down in gold and carbon are 3.1×10^{-13} and 4.5×10^{-13} respectively. These values of Q are used to give the values for 0^{17} ions in carbon and tantalum.

In general, Q is different for different stopping materials so that the experimenter has a limited control over how quickly the ions come to rest. He also has a limited control over v_o through choice of the nuclear reaction he uses and the bombarding energy at which he excites the nuclear state.

The Doppler shift formula for the energy of a gamma ray observed at an angle θ with respect to a moving nucleus is

$$h \nu = h \frac{\nu_o \sqrt{1 - \left(\frac{v}{c}\right)^2}}{(1 + \frac{v}{c} \cos \theta)} \qquad (5.8)$$

and for non-relativistic ion velocities

$$\frac{h \nu}{h \nu_o} \cong 1 - \frac{v}{c} \cos \theta \qquad (5.9)$$

If the energy of the gamma ray is measured at two angles with respect to the recoil axis of the excited nucleus, the observed fractional shift in energy is

$$\frac{\Delta E}{E} = \frac{v}{c} (\cos \theta_1 - \cos \theta_2) \qquad (5.10)$$

For $\theta_1 = 45°$ and $\theta_2 = 135°$, the optimum angles in many cases (Li63a),

$$\frac{\Delta E}{E} = \sqrt{2}\, v/c \tag{5.11}$$

In the ideal measurement, the Doppler shift is observed for the nuclei recoiling into vacuum giving rise to a maximum possible shift.

$$\left(\frac{\Delta E}{E}\right)_{max} = \frac{v_o \sqrt{2}}{c} \tag{5.12}$$

Then the nuclei are deliberately stopped in a solid and the shift measured.

$$\left(\frac{\Delta E}{E}\right)_{obs} = \frac{\bar{v} \sqrt{2}}{c} \tag{5.13}$$

where $\bar{v}$ = the average velocity of the ions.

Now, if the Doppler shift is attenuated it is apparent that some nuclei emitted gamma radiation at a velocity less than v_o, indicating that the nuclear state has a lifetime comparable to the stopping time. With the knowledge of $v(t)$, this lifetime can be calculated from the observed, attenuated shift. In the 0^{17} experiment, the initial velocity, v_o, was calculated from the kinematics of the reaction.

The experimental measurements are presented in the form

$$F = \frac{\bar{v}}{v_o} = \frac{\left(\frac{\Delta E}{E}\right)_{obs}}{\left(\frac{\Delta E}{E}\right)_{max}} = \frac{\left(\frac{\Delta E}{E}\right)_{obs}}{\frac{v_o \sqrt{2}}{c}} \tag{5.14}$$

F, the Doppler shift attenuation factor, can be calculated if the velocity of the recoiling ions is known as a function of time.

$$F(\tau, \alpha) = \frac{\bar{v}}{v_o} = \frac{1}{v_o \tau} \int_0^\infty v(t, \alpha) \, e^{-t/\tau} \, dt \qquad (5.15)$$

where τ = lifetime of the state.

So that with the assumption that $v(t) = v_o \exp(-t/\alpha)$, $F(\tau, \alpha)$ can be plotted as a function of τ.

$$F(\tau, \alpha) = \frac{\alpha}{\tau + \alpha} \qquad (5.16)$$

Calculation of the Characteristic Stopping Time

The calculation of the value of α for 0^{17} ions from that for 0^{16} ions is straight forward. If we assume the same retarding force is acting and let $v(A)$ and $m(A)$ be the velocity and mass of the ion with mass number A,

$$\frac{dv(16)}{dt} = \frac{m(17)}{m(16)} \frac{dv(17)}{dt}$$

For the same energy, the velocities are related by

$$v(16) = \sqrt{\frac{m(17)}{m(16)}} \, v(17)$$

Substituting these relations into (5.6) gives

$$\alpha(17) = \sqrt{\frac{m(17)}{m(16)}} \, \alpha(16) \qquad (5.17)$$

The calculation of q for the stopping material tantalum from the gold data is not so clear, but since the materials are similar, i.e. Z(Au) = 78 and Z(Ta) = 73, q^{-1} is assumed to vary directly as the density, ρ.

$$q(Ta) = \frac{\rho(Au)}{\rho(Ta)} q(Au) \qquad\qquad (5.18)$$

where ρ(Au) = 19.3 and ρ(Ta) = 16.6 gm/cm^3. Using (5.17) and (5.18) the characteristic stopping times for O^{17} slowing down in carbon and tantalum are 4.64×10^{-13} and 3.75×10^{-13} sec. respectively.

These values have been used to calculate $F(q, \tau)$ as shown in Fig. 5.6 for comparison with the experimental value of F, determined from the Doppler shift of the energy of the gamma rays.

No attempt has been made to allow for the events in which the O^{17} ions slow down partially in the carbon target and partially in the tantalum backing. The target thickness was not known accurately, so the errors on τ include the possibility that the total environment was either carbon or tantalum .

An upper limit on the carbon target thickness was obtained from a yield curve obtained during a survey to decide the best energy to measure the n-γ coincidences. None of the small resonances were wider than 200 keV for alpha particles of about 10 MeV. Thus, any uncertainty in v_o from target thickness considerations is less than 2% of v_o.
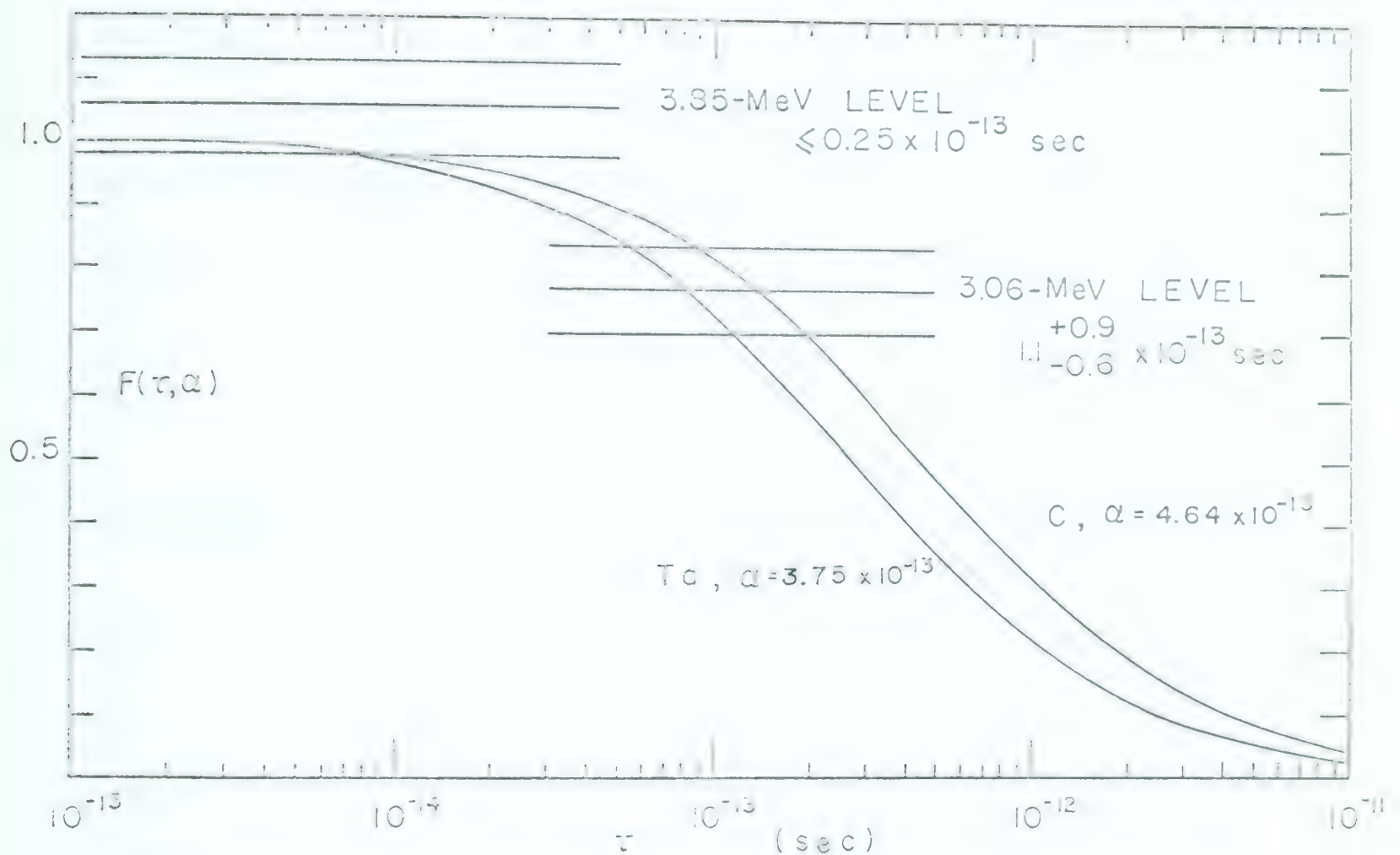
FIGURE 5.6

Doppler Shift Attenuation Analysis

F(τ, α) is the ratio of the mean velocity to the initial velocity of O^{17} ions slowing down in carbon or tantalum. The value of F from Doppler shift measurements is

$$F = \left(\frac{\Delta E}{E}\right)_{obs} \div \left(\frac{v_o \sqrt{2}}{C}\right)$$

Values for the 3.85- and 3.06-MeV state of O^{17} are shown.

Another uncertainty, which is negligible compared to the errors already mentioned, arises because of the finite solid angles subtended by the neutron and gamma ray detectors.

Incidentally, Fig. 5.6 shows the range of τ that can be measured by the Doppler attenuation method. In the next section, a description of the direct timing method of measuring longer nuclear lifetimes is given with reference to the work done on the 0.95-MeV state of B^{12} and the 0.871-MeV state of O^{17}.

5.4 Lifetime Measurements by Direct Timing, Using p-γ Coincidences

The measurement of nuclear radiative lifetimes by direct timing can be done in a variety of ways. The observation of the time relation between two gamma rays emitted in cascade, or the time relation between the arrival of a pulse of bombarding particles and a gamma ray produced by a reaction, is capable. in special circumstances, of yielding measurements of lifetimes as short as $\sim 10^{-11}$ sec. (Sc63).

In this section, some work done using particle-gamma-ray coincidence measurements is described in connection with the nuclear reactions $B^{11}(d,p\gamma)B^{12}$ and $O^{16}(d,p\gamma)O^{17}$. The equipment used for the measurements has been described in Chapters 2 and 4. The main incentives to attempt the measurements were an estimate of the mean life of the 0.95-MeV state of B^{12} and the resolution of the discrepancy in previous measurements of the 0.871-MeV state of O^{17}.

In searching for a reaction involving p-γ coincidences to compare with the $B^{11}(d,p\gamma)B^{12}$ reaction, $O^{16}(d,p\gamma)O^{17}$ was found to be the most suitable. However, a discrepancy existed between two

precision measurements of the lifetime for the 0.871-MeV state in O^{17}.
Kane et al (Ka60) had measured τ_m = 0.255±0.013x10^{-9} sec. by gamma-
gamma coincidences, whereas Gale et al (Ga62) had obtained τ_m =
0.43±0.02x10^{-9} sec. by pulsed-beam methods. Although a measurement
by p-γ coincidences was not expected to give a precision measure-
ment, it was felt that the greater selectivity for the desired
reaction made it a worthwhile measurement. In any case, this investi-
gation would provide a basis for comparison with the B^{12} transition
since the gamma-ray energies are approximately equal, i.e. 0.87
versus 0.95 MeV.

During the course of the measurement, the incentive in the
case of O^{17} was removed when Lowe and McClelland (Lo63) obtained
τ_m = 0.266±0.008 x 10^{-9} sec by pulsed-beam techniques. Our results
are consistent with the lower value and may throw some light on the
reason Gale et al measured an apparent long lifetime.

The pulse-amplitude distribution of Fig. 5.7, obtained by
observing the gamma rays from the deuteron bombardment of a thin
quartz target with a NaI scintillation detector, shows that the
0.87-MeV gamma ray from $O^{16}(d,p)O^{17}$ is the only one with appreciable
intensity. A "Naton" 2 in. by 2 in. plastic scintillator was used
for the final timing measurements and yielded a spectrum with the
Compton edge of the 0.87-MeV gamma ray as the only prominent feature
above 0.5 MeV.

The spectrum of charged particles is equally as "clean"
as the gamma-ray spectrum. The spectrum of Fig. 5.8 was also taken
at a bombarding energy of 1.5 MeV with the particle detector at

FIGURE 5.7
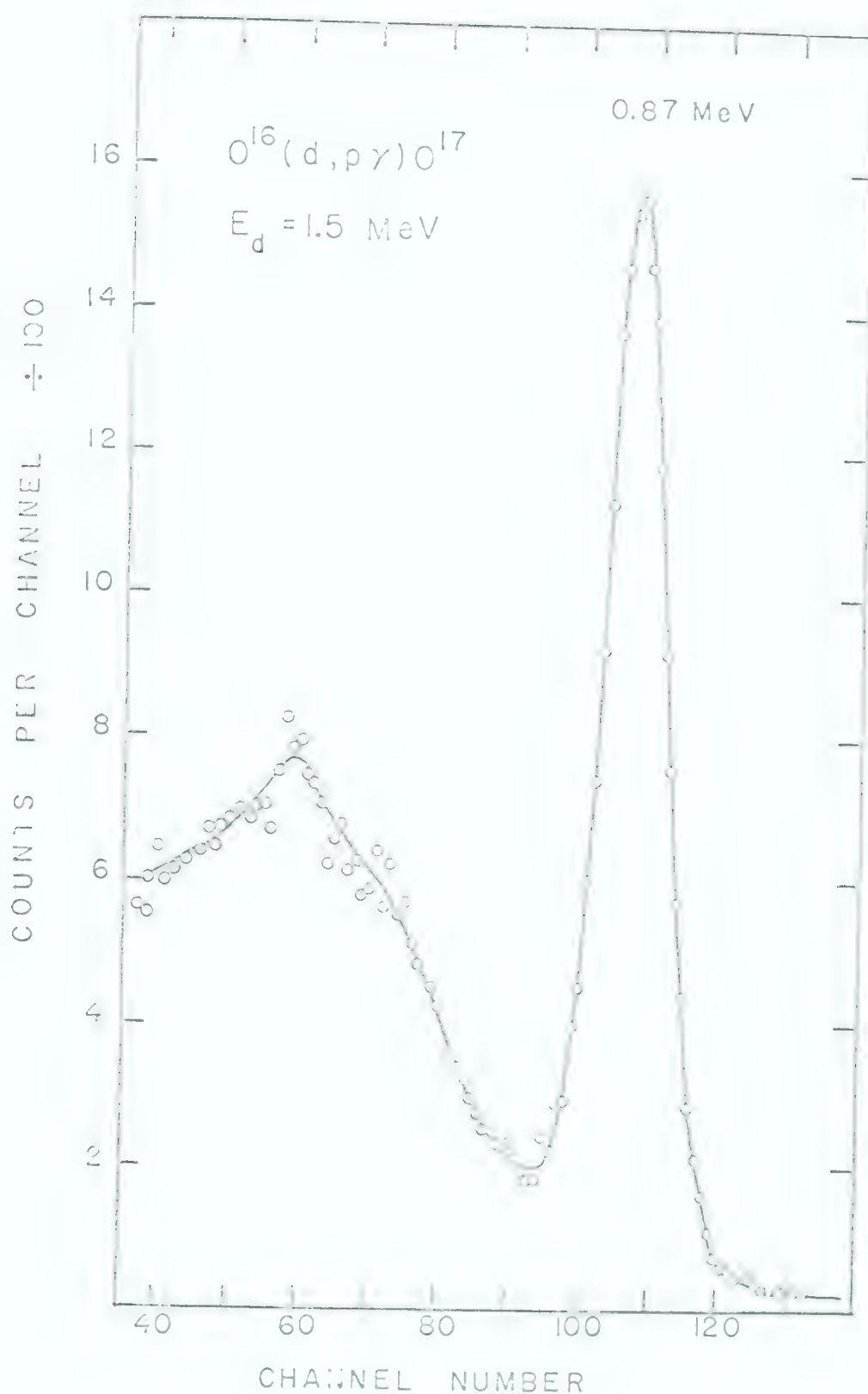
The Gamma-Ray Spectrum from the $O^{16}(d,p)O^{17}$
reaction at E_d = 1.5 MeV

This spectrum from a NaI(Tl) detector was obtained
by bombarding a thin SiO_2 target with deuterons. The
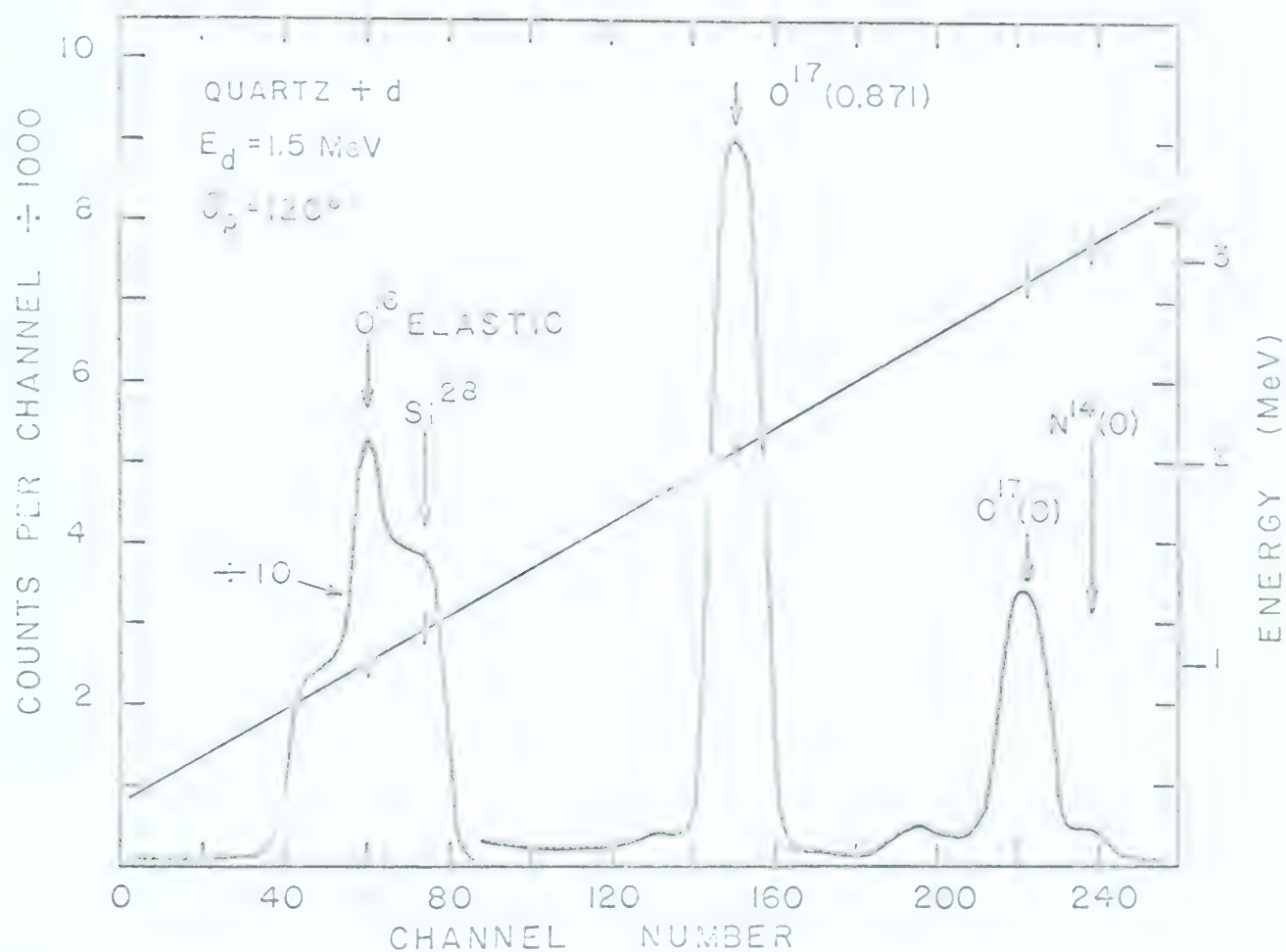only intense peak is the 0.87-MeV gamma ray from O^{17}.

FIGURE 5.8

The Charged-Particle Spectrum from 1.5-MeV
Deuterons Incident on a Thin SiO_2 Target

The proton groups from the $O^{16}(d,p)O^{17}$ reaction to
the ground and the first excited states are the prominent
features above 1.5 MeV. The width of the peaks is
mainly due to target thickness.

120° to the beam direction. The proton groups to the ground (2.9 MeV) and the 0.871-MeV state (2.09 MeV) of O^{17} are the prominent features above the scattered deuterons from O^{16} and Si^{28}. The weak group at 3.1 MeV can be assigned to the $O^{16}(d, \alpha)N^{14}$ reaction to the ground state. The other weak groups are unidentified, but probably arise from reactions with Si. The width of the peaks (150 keV) is due to the thickness of the target, but is not serious here since the proton group of interest is well separated. An estimate of the target thickness from the width of the peaks gives about 400 $\mu gm/cm^2$. The value does not agree with the thickness determined by weighing so that the targets were probably non-uniform.

Figure 5.9 shows the time spectrum for the 0.87-MeV gamma ray. The kicksorter used to record the spectrum was gated on only when the pulses from both detectors satisfied the necessary energy conditions selected by single-channel analysers. The curve shown is the sum of eight consecutive runs. Each run was separately analysed "on line" to give the normalized moments of the distributions which are listed in Table 5.1.
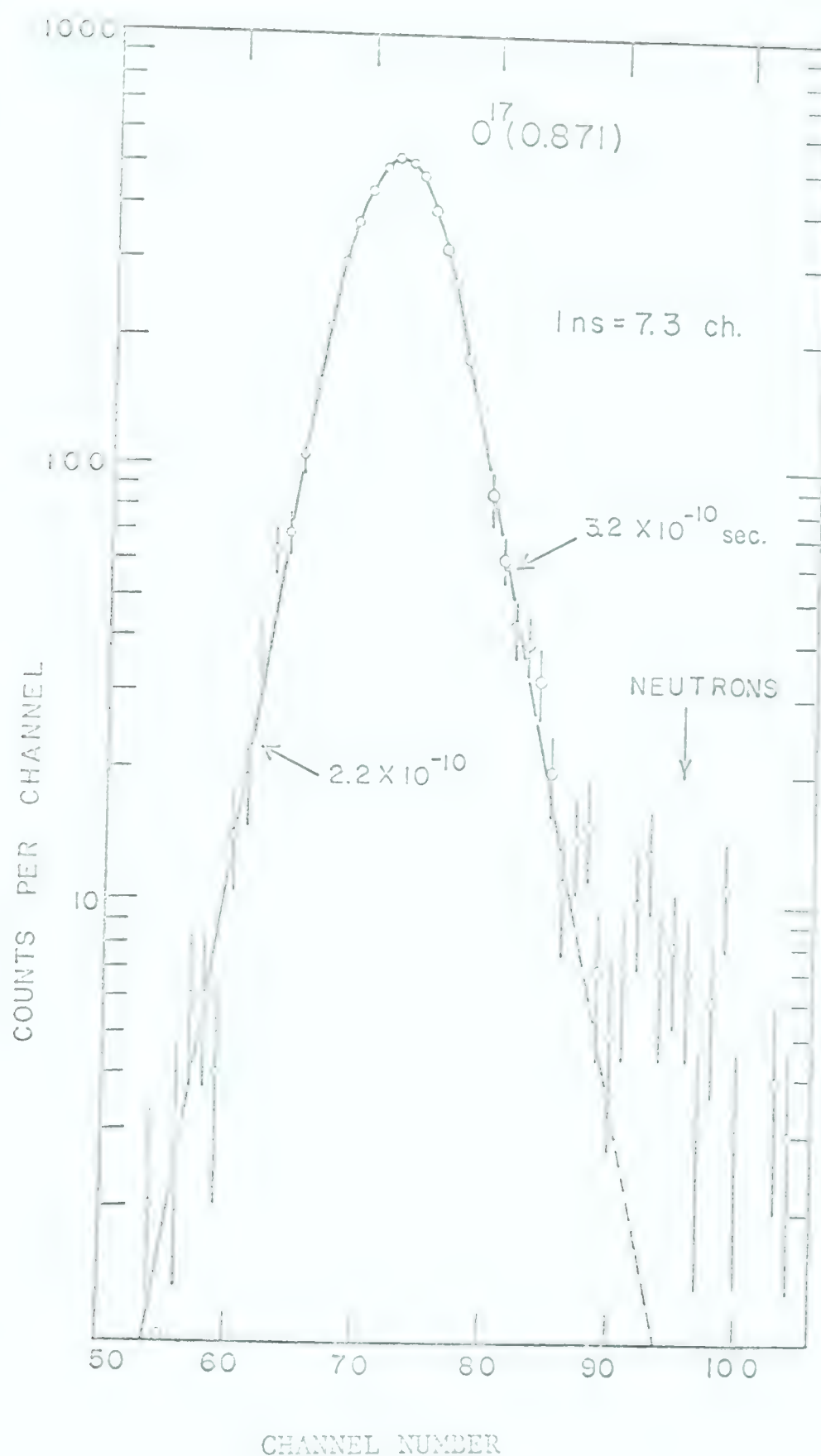
CHANNEL NUMBER

FIGURE 5.9

The Time Spectrum of p-γ Coincidences for the
0.871-MeV State of O¹⁷

A plastic scintillator at -90° detected the gamma
rays in coincidence with protons detected at 110°.
The time shown is the time taken for the intensity to
decrease by a factor of 2.

RUN No.	M1	M2	AREA
1	72.34±0.18	23.6±1.6	699
2	72.56 0.19	24.7 1.8	669
3	72.16 0.17	22.1 1.7	752
4	72.79 0.18	23.2 1.5	685
5	72.37 0.19	23.9 1.7	682
6	71.99 0.19	24.5 1.7	672
7	72.44 0.19	26.3 1.8	693
8	72.26 0.19	27.1 1.7	726
9	72.20 0.18	23.3 1.5	755
10	71.15 0.18	25.0 1.6	744
11	71.34 0.19	25.8 1.8	735

The Normalized Moments of Consecutive Runs on the Delayed
Coincidence Spectrum of O^{17}

TABLE 5.1

From this we could determine that no drifts had occurred, and there-
fore tried a third-moment analysis of the data to obtain a lifetime
estimate of the 0.87-MeV state of O^{17}. Before discussing the
analysis, a few comments regarding Fig. 5.9 are necessary.

As indicated in Fig. 5.9, it was found necessary to put a
10 μin. Ni foil in front of the solid-state detector to prevent the
observation of neutron-coincidences. Presumably the neutrons
arise from high Q-value (d,n) reactions; the heavy-ion recoils

entering the solid-state detector. The effect was pronounced when the gamma-ray detector was at forward angles and may explain the long apparent lifetime measured by Gale et al. The dotted curve shows the tail of the distribution after elimination of neutron-ion coincidences by protecting the detector with the 10 μin. Ni foil.

A third moment analysis of the distribution was carried out after the background had been subtracted (background= 3 counts/ch). The moments were calculated for two limits of integration; the first analysis being calculated from channel 50 to channel 90, and the second over a narrower, more symmetric, range from channel 60 to 85. The first three moments of the sum distribution are shown in Table 5.2.

RANGE (CHANNELS)	M1	M2	M3	AREA
50 to 90	72.4±0.06	21.8±0.5	24.7	5475
60 to 85	72.32±0.06	19.0±0.4	7.3	5404

The First Three Moments of the Delayed Coincidence Curve for $0^{16}(d,p\gamma)0^{17}$ for Runs 1 to 8 in Table 5.1

TABLE 5.2

The third moments are seen to be considerably different for the two analyses since M3 is strongly influenced by the "tails" of

the distribution. Correction factors can be calculated to extra-
polate the computed values of M3 to correspond to the entire range
of the distribution, but this is considered unreliable.

For a "prompt" distribution M3 is zero, i.e. it is
symmetrical. In cases where a prompt curve is not available, the
evaluation of the M3 from the delayed curve has been used to obtain
the mean lifetime (We60). The lifetime can then be calculated from

$$\tau = \left[1/2 \ M3 \right]^{1/3}$$

The values from Table 5.2 give τ equal to 2.3 and 1.5 channels,
which correspond to 0.31 and 0.20 x 10^{-9} sec. respectively. The
value 0.31 x 10^{-9} sec. certainly represents an upper limit on the
lifetime, and therefore decides which of the precision measurements
mentioned earlier is correct.

The data shown in Fig. 5.9 could be used to give a more
precise statement about the lifetime, but published data from
experiments using pulsed-beam techniques are much more accurate.

The experimental problem of measuring the time relation of
the 0.95-MeV gamma ray with respect to the protons from the
$B^{11}(d,p\gamma)B^{12}$ reaction is similar to the O^{17} case. However, the back-
ground is much more serious in the direct spectrum of the charged-
particle detector and the gamma-ray detector. The background under
the proton group of interest (see Fig. 5.10) can give rise to true
coincidences since the continuum under the peak is partially from
the $B^{11}(d,n)C^{12}$ reaction, the C^{12} immediately breaking up by alpha-
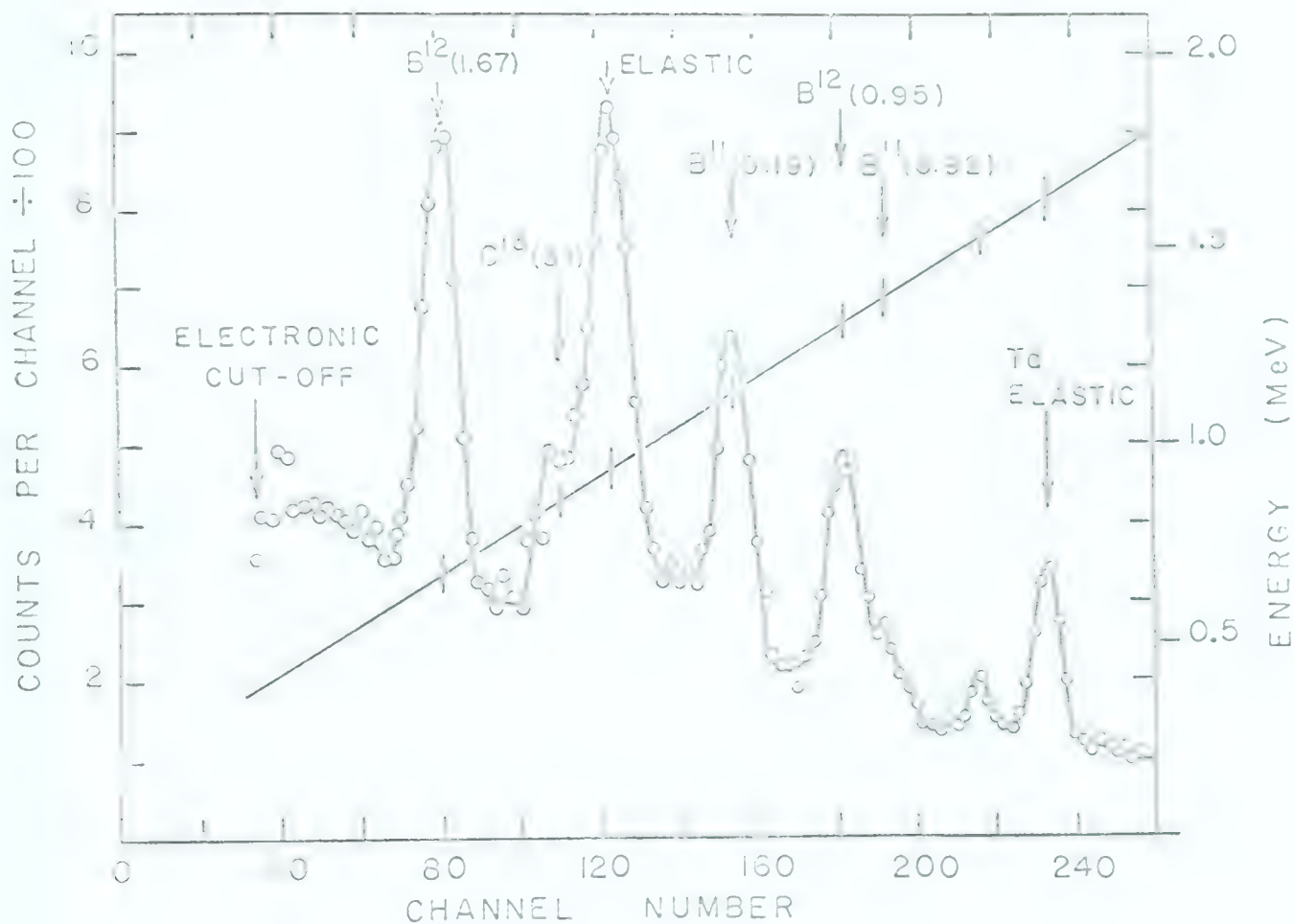particle emission. Shielding the solid-state detector with a foil

FIGURE 5.10

The Charged-Particle Spectrum from a Natural Boron
Target Bombarded with 1.7-MeV Deuterons

The particles were observed at $\theta_p = 110^o$. A single-
channel analyser selected the proton group to the 0.95-MeV
state of B^{12} for fast coincidence measurement. The peaks
are identified by the residual nuclei and the energy level.

to reduce the n-α coincidences is impractical, since the energy resolution would be degraded. To separate the α-n coincidences from the desired p-γ coincidences, the scintillator was placed at a distance sufficiently far from the target (12 cm) so that the neutron peaks would be shifted from the gamma-ray peak in the time spectrum.

To maintain reasonable conditions for comparison of the O^{17} and B^{12} measurements, the side channel selecting the energy of the pulses in the gamma-ray detector was first set on the 0.871-MeV gamma ray for measurement of the $O^{16}(d,p\,\gamma)O^{17}$ reaction, and held at the same settings of bias and channel width for measurements of the $B^{11}(d,p\,\gamma)B^{12}$ reaction. In this way, no extrapolations of the time resolution curve are required for the contribution to $\sigma^2(t)$ by the gamma-ray detector, $\sigma^2(t)$ being the variance of the resolution curve.

The variance had to be extrapolated because of the different energies of the protons. This was done using the relations for the resolution described in Chapter 4.

Since the second moment of the resolution curve for the $O^{16}(d,p\,\gamma)O^{17}$ reaction is known accurately and the mean life of the 0.871-MeV state is known, the resolution curve for a hypothetical "prompt" curve can be derived. The second moment is related to the mean lifetime, τ, by the relation

$$\tau = \left[M_2(F) - M_2(P) \right]^{1/2}$$

where

$M_2(F)$ = the second moment of the delayed resolution curve.

$M_2(P)$ = the second moment of the "prompt" curve.

Using the first value of $M_2(F)$ from Table 5.2, $M_2(P)$ was calculated. A Gaussian curve with $M_2(P) = \sigma^2(t)$ was then calculated and the peak located on the peak of the experimental time spectrum obtained from the $B^{11}(d,p\,\gamma)B^{12}$ reaction. The solid curve drawn in Fig. 2.7B (Chapter 2) was fitted in this manner. From an inspection of the fit, it was concluded that the curve is a "prompt" curve.

W. G. Davies of this laboratory programmed the LGP 30 computer available in the Nuclear Research Center to calculate the moments for the $0^{16}(d,p\,\gamma)0^{17}$ measurements. A 60 digit per second paper-tape punch read out the memory of the pulse-amplitude analyser after each run. The tapes were then fed into the computer for immediate analysis.

The moments listed in Table 5.1 were calculated from the well-known expressions for moments.

$$M_1 = \frac{\sum_k t_k\, n_k}{N}$$

$$M_n = \frac{\sum_k \left(t_k - M_1\right)^n n_k}{N} \qquad , n > 1$$

where:

M_1 = the first moment

M_n = the nth moment

t_k = the channel number

n_k = the number of counts in t_k after background subtraction

N = the total number of counts in the distribution

The statistical errors on M_1 and M_2 were taken to be (Ke51):

$$\Delta M_1 = \sqrt{\frac{M_2}{N}}$$

$$\Delta M_2 = \sqrt{\frac{M_4 - M_2^2}{N}}$$

These expressions are quite adequate since the background under the peak was very small. Also, the background was well determined since a large number of channels was devoted to background on both sides of the resolution curve.

Before concluding this section, some references dealing with the moment analysis of resolution curves to extract lifetimes should be given, since this topic has been covered thoroughly in the literature.

Newton (Ne50) has given a method of analysis related to the moment method, but designed to take advantage of the most statistically significant parts of the prompt and delayed curves. This method is similar to the "subtraction of spectra" method used in Chapter 3 to calculate the small energy change due to the Doppler

shift in the energy of a gamma ray.

The problem of analysis of resolution curves has been treated generally in papers by Bay (Ba50, Ba55) and Birk et al (Bi59). More recent articles dealing with this topic have been published by Jones (Jo59), Gale (Ga62) and Sundström (Su62).

It was mentioned earlier that it is possible to extrapolate the lifetime from moments calculated over a partial range of integration. The method of analysis used by Newton shows how this may be done. Equation (3) of Newton's paper is

$$\frac{dF(x)}{dx} = \lambda \left[P(x) - F(x) \right]$$

where:

$$\lambda = \tau^{-1}$$

$P(x)$ = the "prompt" curve

$F(x)$ = the "delayed" curve

The equation is multiplied by x and integrated over a finite range

$$\int_A^B x \frac{dF}{dx} \, dx = \lambda \int_A^B \left[xP(x) - xF(x) \right] \, dx$$

Integrating the left-hand side by parts and rearranging gives

$$\tau = \frac{\int_A^B \left[xF(x) - xP(x) \right] \, dx}{\int_A^B F(x) \, dx + AF(A) - BF(B)}$$

The numerator is the difference in the "moments" of F and P calculated over a finite range. Since F varies like e^{-x^2}, the usual expression for τ is obtained as the range of integration is made larger, i.e.

$$\tau = M_1(F) - M_1(P)$$

Similar expressions can be obtained for relations involving higher moments, but they become too cumbersome.

REFERENCES

A161   T. K. Alexander and F. S. Goulding, Nucl. Instr. and Methods
13 (1961) 244.

A162   T. K. Alexander and L. B. Robinson, Nucleonics 20 (1962) 70.

A162a   T. K. Alexander, L. B. Robinson and R. A. McNaught, Proc. of
the Harwell Symposium on Nuclear Instruments (1962) 189.

Aj59   F. Ajzenberg-Selove and T. Lauritsen, Nuclear Phys. 11 (1959) 1.

Ar61   J. C. Armstrong and K. S. Quisenberry, Phys. Rev. 122 (1961)
150.

Ba50   Z. Bay, Phys. Rev. 77 (1950) 419.

Ba55   Z. Bay, Phys. Rev. 100 (1955) 1197.

Bi59   Birk, Goldring and Wolfson, Phys. Rev. 116 (1959) 730.

Bu57   W. E. Burcham, Handbuch der Physik XL (1957) 1.

Br63   C. Broude, private communication

Ca63   R. R. Carlson and E. Norbeck, Phys. Rev. 131 (1963) 1204.

Ca63   C. Cavalleri, G. Fabri, E. Gatti and V. Svelto, Nucl. Instr.
and Methods 21 (1963) 177.

Ch54   Christy and Fowler, Phys. Rev. 96 (1954) 3, 851.

Ga62   N. H. Gale, J. B. Garg and J. M. Calvert, Nuclear Phys. 38
(1962) 222.

        N. H. Gale, Nucl. Phys. 38 (1962) 252.

Gi61   W. R. Gibbs and W. Tobocman, Phys. Rev. 124 (1961) 1496.

Go61   S. Gorodetzky et al, Journ. Phys. et la Radium 22 (1961)
573.

Go62   S. Gorodetzky, P. Fintz and A. Gallman, Compts-Rend. 255
(1962) 1505.

Go60   F. S. Goulding and R. A. McNaught, Nucl. Instr. and
Methods 9 (1960) 282.

Ha62   R. W. Harris, G. C. Phillips and C. M. Jones, Nucl. Phys.
38 (1962) 259.

Ha63 M. Harvey, Phys. Letters $\underline{3}$ (1963) 209.

Ho63 H. D. Holmgren, L. M. Cameron and R. L. Johnston, Nucl.
        Phys. $\underline{48}$ (1963) 1.

Ho53 J. R. Holt and T. N. Marsham, Proc. Phys. Soc. $\underline{A66}$ (1953)
        1032.

Hu58 R. Huby, M. Y. Refai and G. R. Satchler, Nucl. Phys. $\underline{9}$
        (1958) 94.

Ja60 A. Jaffe et al, Proc. Phys. Soc. $\underline{76}$ (1960) 914.

Jo59 G. Jones, BAPS $\underline{4}$ (1959) 367.

Ka60 J. V. Kane, R. E. Pixley, R. B. Schwartz and A. Schwartzchild,
        Phys. Rev. $\underline{120}$ (1960) 162.

Ka58 R. W. Kavanagh and C. A. Barnes, Phys. Rev. $\underline{112}$ (1958) 503.

Ke60 E. L. Keller, Phys. Rev. $\underline{121}$ (1960) 820.

Ke51 J. F. Kenney and E. S. Keeping, Mathematics of Statistics,
        Part Two (1951), D. Van Nostrand Co. Inc., New York.

Ko60 E. Kondaiah et al, Nucl. Phys. $\underline{15}$ (1960) 254.

Ku56 D. Kurath, Phys. Rev. $\underline{101}$ (1956) 216.

Ku59 D. Kurath and L. Pičman, Nucl. Phys. $\underline{10}$ (1956) 313.

La61 J. A. Ladd and J. M. Kennedy, Chalk River Report, AECL 1417
        (1961).

La60 A. M. Lane, Rev. Mod. Phys. $\underline{32}$ (1960) 519.

La51 R. A. Laubenstein and M. J. W. Laubenstein, Phys. Rev.
        $\underline{84}$ (1951) 18.

Li60 A. E. Litherland and G. J. McCallum, Can. J. Phys. $\underline{38}$
        (1960) 927.

Li61 A. E. Litherland and A. J. Ferguson, Can. J. Phys. $\underline{39}$
        (1961) 788.

Li63 A. E. Litherland, Bull. Am. Phys. Soc. $\underline{8}$ (1963) 463.

Li63a A. E. Litherland, M. J. L. Yates, B. M. Hinds, and
        D. Eccleshall, Nucl. Phys. $\underline{44}$ (1963) 220.

Li63b A. E. Litherland, Report to the Third Int. Accelerator
        Conf., Boston (1963).

Lo63   J. Lowe and C. L. McClelland, Phys. Rev. 132 (1963) 367.

Ma60   M. H. Macfarlane and J. B. French, Revs. Mod. Phys. 32 (1960) 567.

Ma60a   J. B. Marion, 1960 Nuclear Data Tables, Part 3, U.S. Govt. Printing Office, Washington 25, D.C.

Ma62   S. Matthies, U. G. Neudachin and Yu F. Smirnov, Nucl. Phys. 38 (1962), 63.

Ne50   T. D. Newton, Phys. Rev. 78 (1950) 490.

Ol64   W. C. Olsen, Ph.D. Thesis, University of Alberta (1964).

Po61   D. I. Porat and K. Ramavataram, Proc. Phys. Soc. 77 (1961) 97.

Ra60   B. J. Raz, Phys. Rev. 120 (1960) 169.

Ro63   B. A. Robson and E. Weigold, Nucl. Phys. 46 (1963) 321.

Sc63   A. Schwartzchild, Nucl. Instr. and Methods 21 (1963) 1.

Se63   R. E. Segel, P. P. Singh, R. G. Allas and S. S. Hanna, Phys. Rev. Letters 10 (1963) 345.

Sh54   W. T. Sharp, J. M. Kennedy, B. J. Sears, and M. G. Hoyle, Chalk River Report CRT 556, August, 1954.

Su62   T. Sundström, Nucl. Instr. and Methods 16 (1962) 153.

Ta60   I. Talmi and I. Unna, An. Rev. of Nuclear Science 10 (1960) 353.

Tw62   P. J. Twin and J. C. Wilmott, Finite Solid Angle Correction for NaI(T) Crystals. University of Liverpool (1962).

Va57   Van der Ziel, Solid-State Physical Electronics (1957) Prentice-Hall, New York.

Wa63   E. K. Warburton and L. F. Chase, Phys. Rev. 132 (1963) 2273.

We60   R. Weaver and R.Bell, Nucl. Instr. and Methods 9 (1960) 149.

Wh58   W. Whaling, Handbuch der Physik, E. Flügge, ed., 34 (1958) 193.

Wi56   D. H. Wilkinson, Phil. Mag. $\underline{1}$ (1956) 1031.

Wi57   D. H. Wilkinson, Proc. Rehovoth Conf. on Nuclear Structure
        (1957) 175.

Wi60   D. H. Wilkinson, Nuclear Spectroscopy B, F. Ajzenberg-Selove,
        ed. (1960) Academic Press, N.Y.

Wi61   D. H. Wilkinson, D. J. Pullen and A. B. Whitehead, Proc.
        Rutherford Jub. Int. Conf., Manchester (1961) 565.

Ya63   K. Yagi, Y. Nakajima, K. Katori, Y. Awaya and M. Fujioka,
        Nuclear Phys. $\underline{41}$ (1963) 584.

        These references from Section 4.3 are relisted here for
        the sake of convenience:

To61   P. A. Tove and K. Falk, N.I. & M. $\underline{12}$ (1961) 278.

Fr63   G. Frabri, E. Gatti, and V. Svelto, Proc. of the Conf.
        on Instrument Techniques in Nuclear Pulse Analysis,
        Monterey, Calif. April, 1963. In press.

Ne60   G. C. Neilson, W. K. Dawson, F. A. Johnson, and J. T.
        Sample, Suffield Tech. Report $\underline{176}$ (1960) D.R.B.

Go60   F. S. Goulding, R. W. Nicholson, and J. B. Waugh,
        N.I. & M. $\underline{8}$ (1960) 272.

Ch62   R. L. Chase and V. Svelto, BNL 5350 (1962).

Go63   F. S. Goulding and D. A. Landis, Proc. of the Conf. on
        Instrument Techniques in Nuclear Pulse Analysis,
        Monterey, Calif. April, 1963. In press.

Go60   F. S. Goulding and R. A. McNaught, N.I. & M. $\underline{9}$ (1960) 282.

Ne59   G. C. Neilson, W. K. Dawson and F. A. Johnson, R.S.I. $\underline{30}$
        (1959) 963.

Co63   C. Cottini, E. Gatti, and V. Svelto, Proc. of the Conf.
        on Instrument Techniques in Nuclear Pulse Analysis,
        Monterey, Calif. April, 1963. In press.